Water vapour transport to the high latitudes : mechanisms and variability from reanalyses and radiosoundings

Ambroise Dufour

To cite this version:

Ambroise Dufour. Water vapour transport to the high latitudes : mechanisms and variability from reanalyses and radiosoundings. Earth Sciences. Université Grenoble Alpes, 2016. English. NNT : 2016GREAU042 . tel-01562031

HAL Id: tel-01562031
https://theses.hal.science/tel-01562031
Submitted on 13 Jul 2017

UNIVERSITÉ DE GRENOBLE

THÈSE

Pour obtenir le grade de

DOCTEUR DE L'UNIVERSITÉ DE GRENOBLE

Spécialité : **Sciences de la Terre et de l'Environnement**

Arrêté ministériel : 7 août 2006

Présentée par

Ambroise DUFOUR

Thèse dirigée par **Olga ZOLINA**

préparée au sein du
Laboratoire de Glaciologie et Géophysique de l'Environnement
et de l'École Doctorale
Terre, Univers, Environnement

Transport de vapeur d'eau vers les hautes latitudes

Mécanismes et variabilité d'après réanalyses et radiosondages

Soutenue le **24 mars 2016**,
devant le jury composé de :

M. Christophe GENTHON
Directeur de recherche, LGGE, Président
M. Stefan BRÖNNIMANN
Professeur, Université de Berne, Rapporteur
M. Richard P. ALLAN
Professeur, Université de Reading, Rapporteur
Mme Valérie MASSON-DELMOTTE
Directrice de recherche, LSCE, Examinatrice
M. Peter KOLTERMANN
Professeur, Université de Moscou, Examinateur
Mme Olga ZOLINA
Maître de conférence - chaire CNRS, LGGE, Directrice de thèse
M. Sergey GULEV
Directeur de laboratoire, Institut P. P. Shirshov, Invité

Tous les fleuves se jettent dans la mer, et la mer ne regorge pas,
et les fleuves reviennent au lieu d'où ils coulent pour couler encore.
Ecclésiaste 1:7 *trad.* *Renan* (1881)

Remerciements

J'aimerais remercier ma directrice de thèse, Olga Zolina, de m'avoir guidé pendant ces quatre années. Tout en sachant encadrer avec gentillesse ma tendance naturelle à la dispersion, elle m'a laissé deux libertés, ô combien précieuses en sciences : d'allier théorie et pratique et de suivre des fausses pistes.

En arrivant tout timide en conférence, je guettais de loin Sergey Gulev. Sa présence chaleureuse me laissait réconforté et je repartais bouillonnant de nouvelles idées.

Je suis très reconnaissant envers les professeurs Brönnimann et Allan d'avoir accepté d'évaluer mon manuscrit, et ce dans des délais très brefs. De même, je suis honoré de compter dans mon jury Mme Masson-Delmotte et le professeur Koltermann.

Également membre du jury, je tiens à remercier particulièrement Christophe Genthon qui m'a envoyé à l'autre bout du monde il y a deux ans et m'a introduit au laboratoire de glaciologie il y a quatre ans. C'est un merveilleux écosystème où se côtoient glaciologues, nivologues, chimistes, télédétecteurs, modélisateurs... et même un biologiste, qui se reconnaitra.

Merci du fond du cœur à Ségolène, qui m'a soutenu, supporté et a iL.U.M.iné la fin de ma thèse.

Humblement, je rends hommage à Pikku et à ses disciples : Arsène, son oracle, Déborah, la grande prêtresse et tous les missionnaires de Pikku à travers le monde : Corée, Équateur, Chine, Québec... À bientôt j'espère.

Finalement, je remercie El Niño de m'avoir épargné la frustration de montagnes enneigées pendant la rédaction. Maintenant ça suffit : qu'il neige !

Transport de vapeur d'eau vers les hautes latitudes

Mécanismes et variabilité d'après réanalyses et radiosondages

Résumé : La vapeur d'eau convergeant vers les régions polaires se condense en nuages qui retiennent la chaleur terrestre. Ces nuages donnent lieu à des précipitations, qui adoucissent les océans polaires et épaississent les calottes de glace. Sans changement des vents, le transport de vapeur d'eau est appelé à augmenter dans un climat plus chaud et donc les chutes de neige sur les calottes également. Le surplus d'humidité risque cependant de rétroagir sur le réchauffement de surface.

Afin de contraindre les projections futures, cette thèse se propose d'évaluer la variabilité actuelle du cycle de l'eau dans les hautes latitudes. Elle s'appuie sur sept réanalyses globales et des observations par radiosondages allant de 1979 à 2013. Leurs biais intrinsèques et les approximations de calcul n'entament pas les conclusions principales de cette étude.

En Arctique, mise à part une légère surestimation, le transport d'humidité dans les réanalyses est remarquablement proche des observations, aussi bien dans le temps que dans l'espace. Dans toutes les réanalyses, les perturbations météorologiques advectent la majeure partie de la vapeur d'eau en provenance des moyennes latitudes, de 89 à 94% à 70°N. D'après la plupart des sources, évaporation, précipitation et humidité atmosphérique augmentent en accord avec l'élévation des températures. Toutefois, les flux de vapeur d'eau ne suivent pas la loi de Clausius-Clapeyron car humidité et vents sont moins corrélés, notamment près de la surface.

En Antarctique, le manque d'observations se fait sentir : la convergence de vapeur d'eau sur la calotte varie de 117 à 156 mm par an selon les réanalyses. Le transport côtier, très variable dans l'espace, résulte de l'alternance entre vents catabatiques et passages de perturbations. Sur la côte, les radiosondages signalent une augmentation significative des flux d'humidité vers le Sud. À l'échelle du continent en revanche, les réanalyses ne font état de quasiment aucune tendance.

Enfin, le rôle des phénomènes météorologiques d'échelle courte est évalué de nouveau, selon plusieurs méthodes. En particulier, les cyclones extratropicaux laissent dans les flux de vapeur d'eau une empreinte caractéristique qui peut être détectée et quantifiée.

Mots clés: transport de vapeur d'eau, Arctique, Antarctique, réanalyse, radiosondage, cyclone

Water vapour transport to the high latitudes

Mechanisms and variability from reanalyses and radiosoundings

Abstract : The water vapour converging to the polar regions condenses into heat-trapping clouds and eventually precipitates, freshening the polar oceans and thickening the ice sheets. Modulo circulation changes, the moisture transport is expected to increase in a warmer climate. While the extra precipitation could dampen the ice sheets' contribution to sea level rise, the surplus of moisture could also feed back on the surface warming. However, the present variability of the polar moisture budgets must be known precisely before they can be projected with confidence into the future.

This study examines the atmospheric water cycle of both the Arctic and the Antarctic in seven global reanalyses and in radiosonde observations covering the 1979-2013 period. The impacts of known model and assimilation flaws and of the various numerical approximations were evaluated and proven to be limited, at least for the moisture flux variable and the more recent reanalyses.

In the Arctic, aside from a slight overestimation, the northward fluxes in reanalyses exhibit a remarkable agreement with the radiosoundings in terms of spatial and temporal patterns. In all reanalyses, transient eddies provide the bulk of moisture imports from the mid-latitudes – 89-94% at 70°N. In most datasets, evaporation, precipitation and precipitable water increase in line with what is expected from a warming signal. However fluxes do not scale with the Clausius-Clapeyron relation because the increasing specific humidity is not correlated with the meridional wind, particularly near the surface.

The representations of the Antarctic atmospheric water cycle in reanalyses suffer from the scarcity of observations : the moisture convergence estimates vary from 117 to 156 mm per year. On the coast, the mean moisture flux results from the interplay between transient eddies and katabatic winds, which are particularly sensitive to the orography. The coastal radiosonde sites report significant increases of the southward moisture fluxes but otherwise there are practically no trends in reanalyses on a continental scale.

Finally, the share of transient eddies in moisture advection is qualified using alternate methods. In particular, extratropical cyclones leave a characteristic imprint on the transport field, which can be detected and quantified.

Keywords: moisture transport, Arctic, Antarctic, reanalysis, radiosounding, cyclone

Contents

Introduction

The Antarctic ice sheet north of 82°S receives 171 kg m^{-2} of snowfall per year according to the satellite estimates of *Palerme et al.* (2014) : this is equivalent to 6.4 mm of sea level. Precipitation is also critical in forming the Arctic Ocean freshwater budget (*Serreze et al.*, 2006) and the surface mass balance of the Greenland ice sheet (*Ettema et al.*, 2009; *Burgess et al.*, 2010). In the Arctic, the net upwelling longwave surface radiation oscillated between ~ 40 W m^{-2} under a clear sky and ~ 0 W m^{-2} under moist and cloudy conditions at Ice Station SHEBA[1] during the polar night (*Stramler et al.*, 2011). Indeed, the marginal greenhouse effect of water vapour is particularly strong in dry climates (*Curry et al.*, 1995). The polar heat budgets are also affected by the release of latent heat during condensation and the subsequent clouds (*Solomon*, 2006; *Curry et al.*, 1996). These different phenomena at either pole are all controlled by the transport of moisture from the mid to the high latitudes. They illustrate the need for a detailed description of the atmospheric water fluxes to the polar regions by cross-referencing several sources, both reanalyses and observations. Once the present variability is established, the knowledge of the mechanisms responsible for the advection will enable to interpret and constrain current and future trends. It is the purpose of this thesis.

The effects of climate change are manifest in the Arctic : the surface temperature trend is twice as large as the global trend during the last few decades (*Polyakov et al.*, 2002; *Serreze et al.*, 2009; *Screen and Simmonds*, 2010; *Hartmann et al.*, 2013). The sea-ice extent in September has declined at a rate of 12.4% per decade from 1979 to 2010 with an associated reduction in ice thickness (*Stroeve et al.*, 2012). In Antarctica, the temperature and sea ice trends are more nuanced. The total Antarctic sea ice extent has increased by 1% per decade from 1979 to 2008 (*Cavalieri and Parkinson*, 2008) but these changes are compatible with rising oceanic and atmospheric temperatures (*Zhang*, 2007). West Antarctica and the Peninsula are unmistakenly warming and the continent-wide near-surface temperature trend is positive (*Steig et al.*, 2009; *Bromwich et al.*, 2013). The results from the Coupled Model Intercomparison Project (CMIP5) indicate that the temperature tendencies at both poles will continue during the twenty-first century under different emission scenarios (*Collins et al.*, 2013).

---

[1] Surface Heat Budget of the Arctic Ocean, from 1997 to 1998, in the Beaufort and Chukchi Seas

Since relative humidity remains constant in climate model projections, specific humidity follows the Clausius-Clapeyron relation and should increase at a rate of 7% per degree Kelvin of warming (*Held and Soden*, 2006; *Allan et al.*, 2013). According to the authors, the moisture advection should increase in similar proportions, provided the winds do not change. This view is supported by model projections for the Arctic (*Bengtsson et al.*, 2011; *Hwang et al.*, 2011) and the Antarctic (*Gregory and Huybrechts*, 2006; *Krinner et al.*, 2007). In the Arctic, the retreat of the sea ice is a confounding factor : the intensification of the atmospheric water cycle may be driven by local evaporation over ice-free ocean rather than advection (*Bintanja and Selten*, 2014; *Kopec et al.*, 2016). Through the direct radiative impact and indirect effect on clouds, the increasing amounts of moisture could themselves be a cause of the accelerated surface warming.

In situ observations of the components of the hydrological cycle are rare in the polar regions, particularly over the oceans and ice sheets. The sparse terrestrial station network, buoys, drifting ice stations and occasional scientific cruises do not provide the adequate temporal and spatial coverage for an explicit description of the regional climate and its evolution. Satellite data are indirect and subject to large uncertainties in the Arctic and Antarctic and may be limited in time by several years for specific instruments onboard specific satellites (*Groves and Francis*, 2002; *Boisvert et al.*, 2013; *Palerme et al.*, 2014).

Atmospheric reanalyses benefit from both in situ and remote sensing observations and likely constitute the most comprehensive source of information on polar hydrological budgets at present. However, neither precipitation nor evaporation is assimilated in global reanalyses : instead, they are computed based on model physics during the generation of the first guess field. As a result, these variables vary considerably across the datasets : for instance the net precipitation (precipitation minus evaporation) over global land areas varies by a factor of two between NCEP NCAR R1 and NCEP CFSR (*Trenberth et al.*, 2011). Moisture transport, however, is computed from wind and humidity, both of which are analysed, hence the results are more consistent among datasets. *Trenberth et al.* (2011) reported only a 43% difference in moisture convergence over land between NCEP NCAR R1 and NCEP CFSR. For the Arctic, the difference between the moisture transport estimated by ERA 40 (*Jakobson and Vihma*, 2010) and MERRA (*Cullather and Bosilovich*, 2011) is below 10%. Transport-based estimates of convergences also tend to be less affected by changes in the observation system unlike precipitation and evaporation. In MERRA for example, the transition from TOVS to ATOVS between 1998 and 2001 introduced a positive trend in global precipitation that is absent from the observational records (*Trenberth et al.*, 2011).

Our work builds upon a number of previous studies evaluating moisture transport in reanalyses, starting with *Genthon and Krinner* (1998) for Antarctica with ERA 15 and *Cullather et al.* (2000) for the Arctic with NCEP NCAR R1 and ERA 15. *Groves and Francis* (2002) are noteworthy for having decomposed the moisture flux into the monthly mean flow and transient eddy contributions, demonstrating the predominance of the latter, confirming the results of *Peixóto and Oort* (1992). In addition to this decomposition, we use the storm trajectories described in *Gulev et al.* (2001); *Rudeva and Gulev* (2007) and *Tilinina et al.* (2013) to evaluate the specific role of extratropical cyclones. *Cullather and Bosilovich* (2011) analysed the moisture budget of both polar regions as depicted in MERRA and included comparisons of evaporation and precipitation fields from ERA Interim and CFSR. We extend the comparison to JRA 55 as well as the older reanalyses – NCEP NCAR R1, NCEP DOE R2 and JRA 25, all of which been continued up to 2013 (unlike ERA 40). Besides evaporation and precipitation, we specifically focus on water vapour advection, as it is more stable and better suited to establish model-independent features of the hydrological cycle variability. This variable can also be validated against observations, namely radiosonde data. We are extending the earlier observational studies of *Connolley and King* (1993) and *Serreze et al.* (1995) that predated the widespread use of reanalyses.

The thesis is organized as follows. Chapter 1 describes the data sources, including their limitations, as well as the methods used to compute the moisture transports. Chapter 2 is dedicated to the Arctic, Chapter 3 to the Antarctic. These sections are subdivided into the analysis of the climatological spatial structure, of long-term moisture budgets, of the transport components due to the mean flow and transient eddies and of the seasonal cycle and interannual variability of the source terms. Finally, Chapter 4 offers some perspective on the methods used to distinguish between mean flow and transient eddies and revises the role of extratropical cyclones.

Chapter 1

Data and methods

1.1 Reanalyses

Numerical weather prediction models need to be initialised before any forecast can be made. This initial state, or analysis, should draw upon as many observations of the atmosphere as possible. Unfortunately, the observation network – ground stations, satellite tracks, buoys, aeroplane routes, etc. – bears no relation with the model grid. On first sight, a simple interpolation of the observations to the model grid seems the obvious solution. However, at synoptic scales, the variables governing the atmosphere – winds, pressure, temperature, etc. – are tied, they rarely depart from quasi-equilibria, like those defined by the quasi-geostrophic equations. A careless interpolation will likely throw the modelled atmosphere off balance, leading to violent adjustments in the first hours of the forecast.

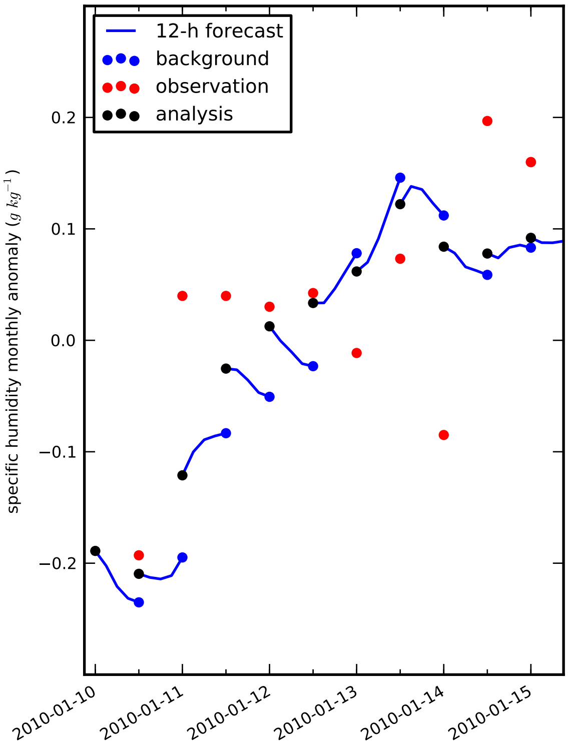

Figure 1.1: Assimilation of specific humidity at 600 hPa over the South Pole based on ERA Interim data and radiosoundings

Instead of producing an analysis from scratch, weather forecasters take advantage of the last prediction, called the “background,” which is already in equilibrium. It serves as a first-guess for the analysis. Figure 1.1 illustrates how the specific humidity at the South Pole was analysed on the 10^{th} of January, 2010, at 12 o’clock. A previous forecast, initialised twelve hours before, provides the background (blue dot). At noon, a weather balloon was launched from the South Pole station : its humidity measurements constitute the observations (red dot). The analysis (black dot) is a compromise between both sources of information.

Weather predictions centres frequently upgrade their models and data assimilation systems. Most conspicuously, when more powerful computers are acquired, the spatial resolution is increased. Such modifications prevent climatologists from using archived "operational" analyses to study global warming for instance : the abrupt or gradual improvements may lead to spurious shifts or trends in the temperature time series.

In "retrospective" analyses, or reanalyses, historical observations are processed with the same forecast model and data assimilation system. They provide a dynamically consistent view of the past state of the atmosphere that makes the best use of past observations. Nevertheless, the data input streams do change during the reanalysis period as new instruments are set up, drift or are replaced. Consequently, a trend or shift in the reanalysis data may reflect a modification in the observing system rather than a climatic phenomenon : trends derived from reanalysis data should therefore be treated with caution (*Bengtsson et al.*, 2004a). New satellites are notorious for disrupting the continuity of the time series. This is particularly important for the polar regions, where the assimilation relies predominantly on remote sensing due to the scarcity of conventional observations.

We used the output of seven global reanalyses (Table 1.1).

Reanalysis	reference	model vintage	model resolution	available resolution	data assimilation
NCEP NCAR R1	*Kalnay et al.* (1996)	1995	T62 L28	2.5° L8	3D-Var
NCEP DOE R2	*Kanamitsu et al.* (2002)	2001	T62 L28	2.5° L10	3D-Var
JRA 25	*Onogi et al.* (2007)	2004	T106 L40	1.25° L10	3D-Var
ERA Interim	*Dee et al.* (2011)	2006	T255 L60	0.75° L23	4D-Var
NCEP CSFR	*Saha et al.* (2010)	2009	T382 L64	0.5° L23	3D-Var + FOTO
MERRA	*Bosilovich et al.* (2006) *Rienecker et al.* (2011)	2009	1/2°*2/3° L72	1/2°*2/3° L23	3D-Var + IAU
JRA 55	*Ebita et al.* (2011) *Kobayashi et al.* (2015)	2009	T319 L60	0.5° L23	4D-Var

Table 1.1: Major characteristics of reanalyses compared during the study

Besides the increasing spatial resolution – from T62 in NCEP R1 to T382 in CFSR – the modern reanalyses distinguish themselves from the first generation by their improved model physics and data assimilation systems, especially regarding satellite observations. ERA Interim and JRA 55 both implement four-dimensional variational data assimilation (4D-Var) to account for the observations' temporal distribution within the assimilation window. CFSR still relies on 3D-Var but with a refinement : "First Order Time interpolation to the Observation" (FOTO, *Rancic et al.* (2008)). CFSR also couples atmosphere, simplified ocean and sea ice models to generate the 6-hourly guess field. Unlike the other datasets, MERRA is based on finite volume dynamics. Its "Incremental Analysis Update" (IAU) scheme improves on 3D-Var to dampen the analysis increment. In IAU, a correction is applied to the forecast model gradually, limiting precipitation spin-up in particular. To explain this important phenomenon, we must first introduce the basic equations of the atmospheric water cycle.

We consider a volum of air δV delimited by infinitesimal increments in the three directions, $\delta x, \delta y$ and δz. At synoptic scales, altitude and pressure are linked via the hydrostatic approximation : $\rho\,\mathrm{d}z = -\mathrm{d}p/g$ with ρ the density, g the standard gravity and p the pressure. The mass δm this volume contains can now be written $\delta x\,\delta y\,\delta p/g$ without the density term, ρ. Let ω be the vertical wind component in pressure coordinates and $\vec{u}$ the horizontal wind. In the absence of precipitation, the conservation of mass implies that the material derivative of δm be zero hence :

$$\frac{D\,\delta x\,\delta y}{Dt}\delta p + \delta x\,\delta y\frac{D\,\delta p}{Dt} = 0 \tag{1.1}$$

$$\operatorname{div}\vec{u} + \frac{\partial\,\omega}{\partial p} = 0 \tag{1.2}$$

In pressure coordinates, the equations of fluid mechanics simplify as if the fluid were incompressible.

The mass of water vapour the volum contains is : $q\,\delta m$ with q the specific humidity. The moisture content of this air parcel decreases when vapour precipitates and increases when condensed water evaporates. Such evaporation occurs either at the surface or in the atmosphere, as when a cloud dissipates. In other words :

$$\frac{D\,q\,\delta m}{Dt} = (e - c)\,\delta m \tag{1.3}$$

e and c are respectively the evaporation and condensation per unit mass. We use the conservation of mass equation in pressure coordinates to expand the material derivative :

$$\frac{\partial q}{\partial t} + \operatorname{div}(q\vec{u}) + \frac{\partial q\omega}{\partial p} = e - c \tag{1.4}$$

$\operatorname{div}(q\vec{u})$ is the divergence of the horizontal moisture flux. The term in ω vanishes if we integrate the local equation from the surface (pressure p_s) to the top of the atmosphere (pressure zero) :

$$\frac{\partial}{\partial t}\int_{0}^{p_s} q\frac{\mathrm{d}p}{g} \;+\; (P-E) \;=\; \text{- div}\int_{0}^{p_s} q\vec{u}\,\frac{\mathrm{d}p}{g} \tag{1.5}$$

where E is the evaporation and P the precipitation, both per unit surface area.

The moisture budget of an atmospheric column can be analysed by evaluating either side of the moisture balance equation (Eq. 1.5). The first term on the left hand side, the precipitable water tendency, is typically negligible compared to the other terms for yearly time scales. The second term, P-E, or net precipitation, is computed by accumulating precipitation and evaporation during the generation of the model first guess. This is the so-called “physics output” method. NCEP NCAR R1, NCEP DOE R2, JRA25 and NCEP CFSR do not provide a ready-made evaporation product ; thus, we computed it from the latent heat flux using the skin temperature and snow and ice cover to determine the phase change enthalpy. The second method, referred to as the “aerological” method, evaluates the right hand side of Equation 1.5, the moisture flux convergence, which is based on analysed humidity and winds. The two methods yield different results : the moisture budget of the reanalyses is typically not closed (e.g. *Trenberth et al.* (2011), *Cullather and Bosilovich* (2011)). The physics output method is more dependent on model physics and tends to be affected by changes in input data streams. The aerological method is more stable and its output in different reanalyses is more coherent (*Trenberth et al.*, 2011).

Weather forecasters did not produce reanalyses with climatology in mind, at least not originally. The reanalyses were used to initialise “reforecasts” that served as benchmarks to evaluate their model and data assimilation schemes, as well as to study the impact of changes in the observation system. Reforecasts with lead times up to ten days are available for ERA Interim. In Figure 1.2, we plot the trajectories of the forecasted specific humidity at 600 hPa over the South Pole for different starting dates with colours varying from blue to red depending on the lead time. In this anecdotal example, the humidity at 600 hPa does not present any obvious tendency in the first hours of the model run. Does this hold over larger areas and for the whole 1979-2013 period ? For this purpose, we build climatologies with constant lead times to study how the worldwide water cycle is set in motion in ERA Interim (Figure 1.3, a). As reported by *Kållberg* (2011), precipitation undergoes a minor spin up in the first six hours of the forecast : a 7.8% increase. The atmosphere also has a slight tendency to dry up, particularly at lead times of 12 and 24 hours. We cannot account for the mismatch between evaporation, precipitation and the integrated water tendency (red

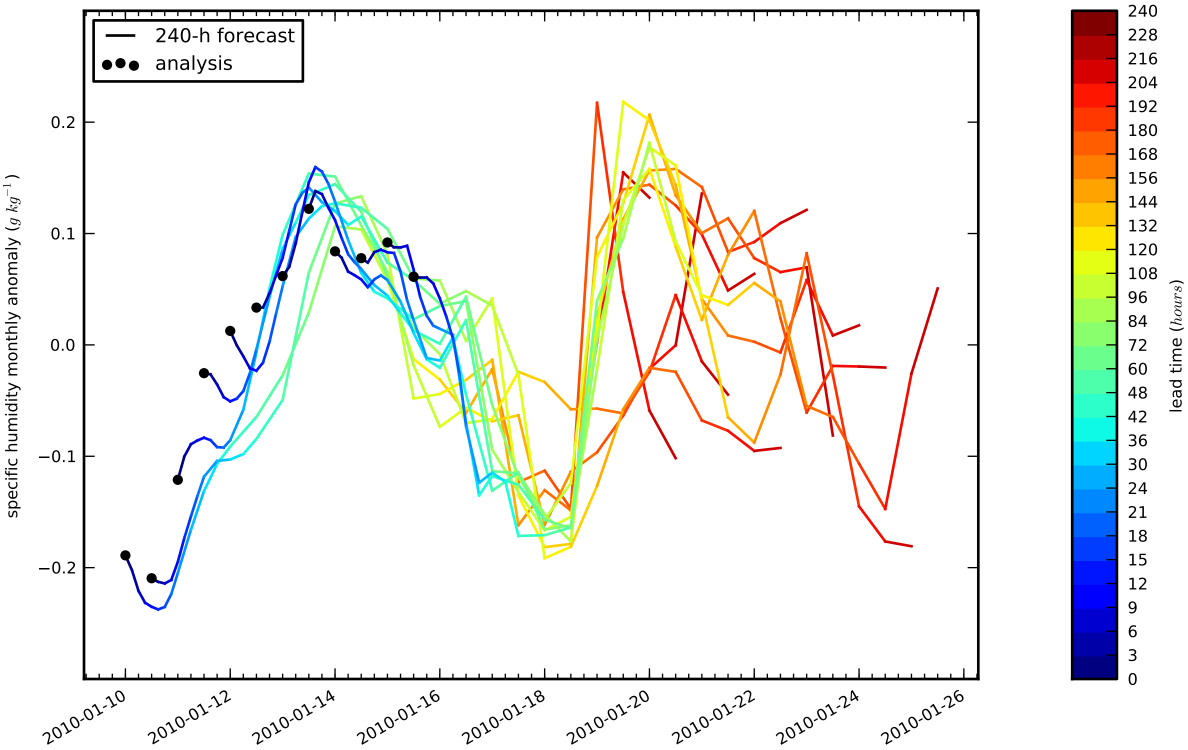

Figure 1.2: Ten day ERA Interim reforecasts for specific humidity at 600 hPa over the South Pole.

line). It is not mentionned in *Kållberg* (2011).

The water budget of the polar regions involves an extra term : the moisture advection from the mid-latitudes, which is unaffected by the spin-up of the model (magenta lines in Figure 1.3, b and c). The integrated water content shows slightly more pronounced oscillations than in the worldwide case. The model spin-up of precipitation is much more severe : +28.2% for the Arctic and +35.8% for Antarctica. At what lead times should we compute the precipitation : between 0 and 3 hours to be as close to the analysis as possible, or between 18 and 24 hours, when precipitation has stabilised ? There is no such ambiguity with moisture advection. The standard practice in other reanalyses is to archive the precipitation accumulated during the six first hours of the forecast : we followed this convention.

1.2 Radiosoundings

To validate the characteristics of moisture transport derived from reanalyses, we compared them to observations, namely radiosoundings from the Integrated Global Radiosonde Archive

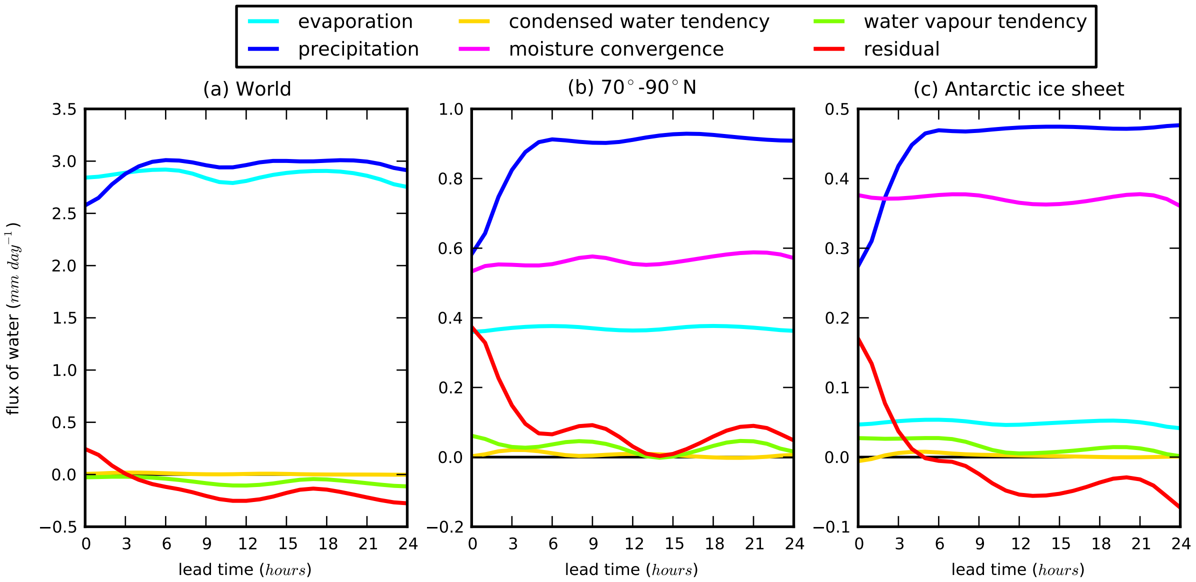

Figure 1.3: Spin-up of the ERA Interim water cycle for the entire atmosphere (a), the polar cap north of 70°N (b) and the Antarctic ice sheet (c).

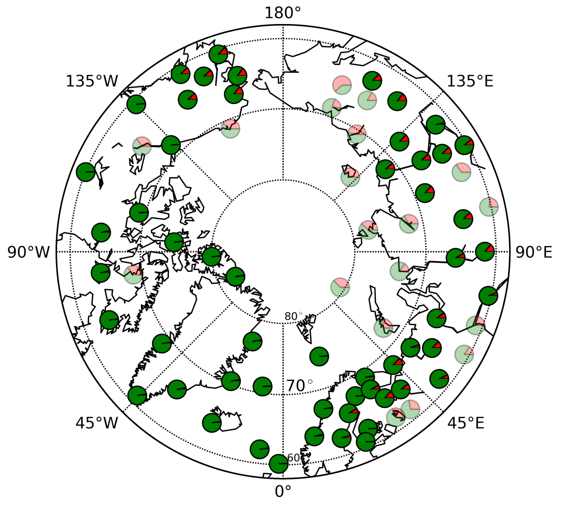

Figure 1.4: Arctic radiosonde launch sites active from 1979 to 2013 with the proportion of missing daily values (pie charts). Rejected sites are semi-transparent.

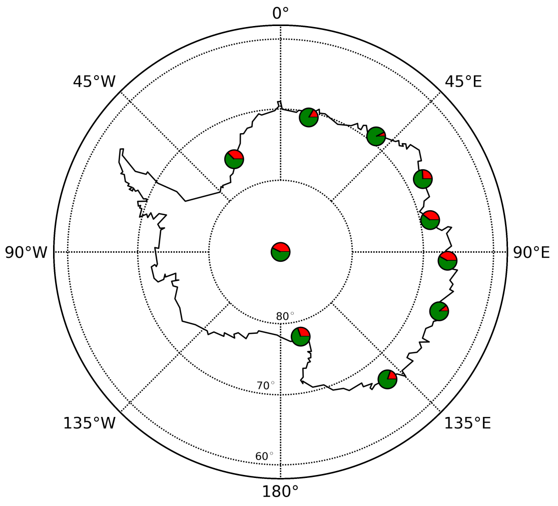

Figure 1.5: Same as Figure 1.4 but for the Antarctic. No rejection threshold was applied.

(IGRA, *Durre et al.* (2006)). For the region north of 60°N, seventy four sites were active throughout the satellite era from 1979 to 2013 (Figure 1.4). Thirty-nine sites are located on the coast including six on small islands. In Antarctica, there are only ten available sites, all but one on the coast of East Antarctica (Figure 1.5). The observation frequency ranges from once to twice daily, and corresponds to the synoptic times used in operational and retrospective analyses. Measurements are supposed to be available at least on certain standard levels, which are 1000, 850, 700, 500, 400, 300, 250 and 200 hPa in the troposphere.

IGRA does not constitute independent data : finding radiosoundings that are not assimilated in reanalyses is quite a challenge (*Francis*, 2002). Nevertheless, radiosoundings are important to check the internal consistency of the data assimilation schemes. There may be conflicts between in situ and remote sensing sources as in *Grant et al.* (2008) or the observations may be overridden by the model. Radiosoundings also have their limitations particularly in dry and supersaturated conditions (*Connolley and King*, 1993; *Miloshevich et al.*, 2006). In certain cases, the assimilation procedure may be justified in giving them little weight.

Before being archived in IGRA, soundings pass a number of quality control checks. The pressure, temperature and geopotential height variables receive a particular attention. However, the specific humidity and winds, which are of special interest to us, did not undergo climatological checks in IGRA ; thus, we performed additional quality screens on these variables to filter out extremely high values. For this purpose, we used the median as an indicator of central tendency and the interquartile range (IQR) as a measure of spread. Means and standard deviations are overly sensitive to outliers and yield artificially high thresholds. We computed the medians and IQRs for each calendar month to account for the variability due to the annual cycle. After subjective examinations of unnatural shifts and outliers in the time series and vertical profiles, we chose to remove values lying outside the range of ± 4 IQR from the median. Because the IQR of a Gaussian distribution is 1.35 times its standard deviation, our criterion corresponds to approximately $5.4\,\sigma$. Although this threshold seems permissive, in the Arctic, it excludes 4.8% of the wind data and 5.5% of the humidity data. Additionally, we required the existence of values on at least five pressure levels before performing linear interpolations of the vertical profiles. Finally, we only considered stations with at least 85% of days with valid soundings over the entire period, which led us to discard 11 sites in the Arctic. Such a threshold would leave us with no data in Antarctica : in Chapter 3, we detail an ad hoc procedure to deal with the gaps in the observation records.

Dataset	NCAR R1	DOE R2	JRA 25	ERA I	CFSR	MERRA	JRA 55	IGRA
subsampled	9.31	9.47	9.52	9.66	9.33	9.92	9.47	8.76
unsampled	10.04	10.11	9.68	9.67	9.48	10.26	9.71	

Table 1.2: Mean meridional moisture flux averaged over all radiosonde sites in reanalyses and IGRA (kg $m^{-1}s^{-1}$). The reanalyses were co-located in both time and space with the soundings in the second line but only in space in the third line.

To avoid a sampling bias, we only compared simultaneous observations and reanalysis values. The co-location of reanalysis data with radiosonde sites was performed via bilinear interpolation. In the Arctic, before we averaged a variable over the radiosonde sites, we first grouped the stations in eight 45° longitudinal sectors. We averaged the variable within these longitudinal bands after which the averaging was applied over the bands. In this manner, the data-rich regions (such as Europe) are not given an unfair emphasis. We were also concerned that our filters would be biased against intense moisture events because they exclude exceptionally high values of humidity and wind. However, in Table 1.2, the mean meridional moisture fluxes in reanalyses over the radiosonde sites are only slightly reduced by the subsampling.

1.3 Computation of the fluxes

To calculate the moisture budget of a given region we integrate the moisture balance equation (Eq. 1.5). We must resort to finite differences to compute the divergence and this introduces an error, pointed out by *Seager and Henderson* (2013). ERA Interim happens to provide a vertically integrated moisture convergence product calculated in spectral space on model levels. Over Greenland, it deviates by 0.3% from the finite differences result ; even less over the Arctic Ocean. When we compute the water budget over a polar cap, say the region north of 70°N, the divergence term simplifies to :

$$\iint\limits_{\phi>70^\circ} \int\limits_0^{p_s} \mathrm{div}(q\vec{u})\frac{\mathrm{d}p}{g}\mathrm{d}s = -\int\limits_{-\pi}^{\pi}\int\limits_0^{p_s} qv\frac{\mathrm{d}p}{g}\mathrm{d}\lambda \tag{1.6}$$

where ds is a surface element, ϕ latitude, λ longitude and v the meridional wind.

Up to now, we have assumed that the transport of water took place exclusively in the gas phase. In the transition from Equation 1.4 to Equation 1.5, we implicitely assumed that the vertical integral of the condensation per unit mass was precipitation. Indeed, the condensed phases, liquid and frozen, only make a fraction of the total column water : 0.9% north of

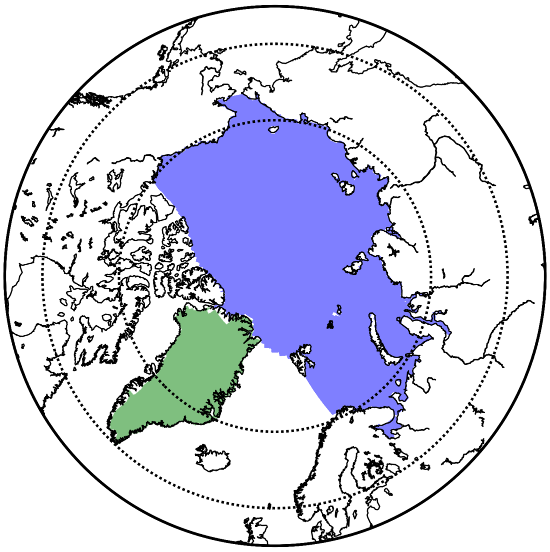

Figure 1.6: Arctic domains : the polar caps north of 60°N, 70°N, the Arctic Ocean defined in *Serreze et al.* (2006) and the Greenland ice sheet defined in *Cullather and Bosilovich* (2011).

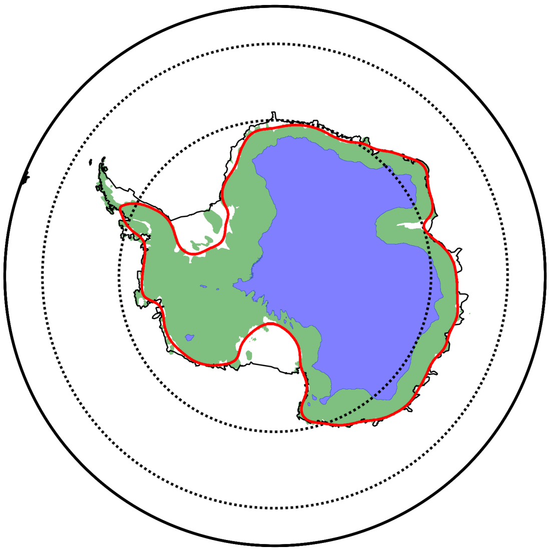

Figure 1.7: Antarctic domains : the polar caps south of 60°S, 70°S, the Antarctic ice sheet (smoothed boundary in red, excludes ice shelves) and plateau (elevation > 2250 m), as in *Palerme et al.* (2014).

60°N and 1.5% south of 60°S according to ERA-Interim. Few datasets provide the condensed water fraction on model levels and to our knowledge, no study has evaluated their impact on the water transport up to now (Table 1.3).

The condensed water fluxes are extremely variable from one dataset to the next. For the polar cap north of 70°N, the estimates from JRA 25 and NCEP CFSR vary by a factor of three, over Greenland by fifty. Unlike humidity, the liquid and frozen water fractions are not assimilated by the reanalyses (as far as we know). They are dependent on the forecast model's individual microphysics schemes. CFSR has the most intense condensed water fluxes : they make for 19.6% of the total water fluxes to Greenland. If moisture advection is used as a proxy for net precipitation on the ice sheet, it is critical to include fluxes of liquid and frozen water as well. The proportion of condensed water fluxes is higher for smaller domains like the Greenland ice sheet or the Antarctic plateau. In larger domains, most of the precipitated water was imported as vapour and condensed later, inside the domain boundaries. To keep the datasets comparable, we only consider water vapour fluxes in the remainder of the manuscript.

Under the hydrostatic approximation, the use of pressure as a vertical coordinate greatly simplifies the equations by removing the density term (e.g. Equation 1.2). However, the

Region	Reanalysis	water vapour flux	condensed water flux
70°-90°N	JRA 25	187.2	2.0
	ERA Interim	194.7	3.9
	NCEP CFSR	191.8	6.8
	MERRA	202.8	3.0
60°-90°N	JRA 25	259.3	5.6
	ERA Interim	257.3	7.9
	NCEP CFSR	260.3	12.5
	MERRA	265.7	5.0
Arctic Ocean	JRA 25	175.3	1.5
	ERA Interim	184.5	3.2
	NCEP CFSR	204.1	0.5
	MERRA	226.3	0.3
Greenland	JRA 25	163.0	1.3
	ERA Interim	177.7	2.0
	NCEP CFSR	289.2	**70.6**
	MERRA	395.3	**21.1**
70°-90°S	JRA 25	184.5	5.4
	ERA Interim	174.1	9.2
	NCEP CFSR	174.5	**13.8**
	MERRA	184.9	6.8
60°-90°S	JRA 25	309.5	6.9
	ERA Interim	335.9	11.2
	NCEP CFSR	353.6	15.0
	MERRA	345.9	6.7
Antarctic ice sheet	JRA 25	147.2	**9.6**
	ERA Interim	137.3	**16.5**
	NCEP CFSR	119.8	**26.4**
	MERRA	156.5	**11.0**
Antarctic plateau	JRA 25	59.6	**3.7**
	ERA Interim	47.2	**7.6**
	NCEP CFSR	52.5	**16.7**
	MERRA	48.4	**7.0**

Table 1.3: Atmospheric water convergence (in kg m^{-2} $year^{-1}$) to the various domains studied divided by phase : as vapour on the one hand and as a liquid or a solid on the other. The font colour is red when the condensed fluxes constitude more than 5% of the total water fluxes.

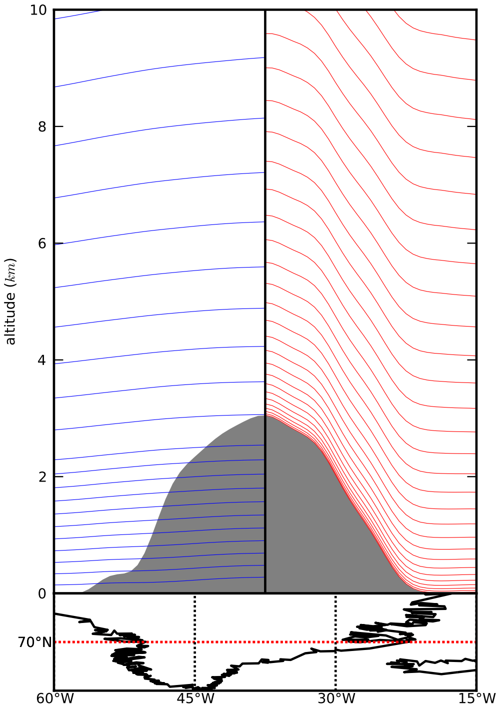

Figure 1.8: Longitudinal profile of the Greenland ice sheet on the 1^{st} of January, 2010. The blue lines locate the pressure levels of the ERA Interim archive ; the red lines locate the reanalysis' original model levels.

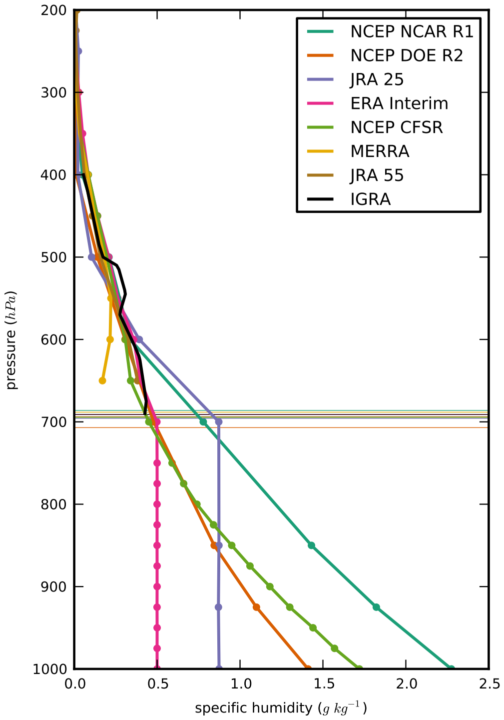

Figure 1.9: Vertical profile of specific humidity at the South Pole on the 1^{st} of January, 2010. The dots materialize pressure levels, the horizontal lines correspond to the surface pressure

numerical models use a different type of vertical coordinate. The conversion from "model levels" to "pressure levels" involves interpolation, a first source of error. What's more, the sea level pressure during an anticyclone may be higher than the first pressure level, 1000 hPa, hence the near surface information is lost. Conversely, the surface pressure over orography is bound to be lower than 1000 hPa : the pressure levels below the surface must be masked or filled with fictitious values. In Figure 1.8, the blue pressure levels intersect the grey profile of Greenland yet the lowest level does not make it to the sea. At the South Pole Station on the 1^{st} of January, 2010, the surface pressure was approximately 700 hPa : in some datasets, the specific humidity profile was extended to 1000 hPa using different conventions (Figure 1.9).

Whenever possible, it is preferable to make the numerical vertical integrations on model levels. In the forecast models of the first generation reanalyses, the vertical is divided in σ-coordinates. σ is simply the ratio of the pressure at a given level to the surface pressure. In NCEP NCAR R1 and NCEP DOE R2, σ ranges from 0.995 to 0.00273. If the surface pressure is 1000 hPa, this corresponds to 995 hPa for the first level and 2.73 hPa for the last. Whatever the surface elevation or the weather conditions, the σ-coordinates follow the terrain, just like the red curves in Figure 1.8. This ensures that the lowest layers of the atmosphere are properly represented in the model.

Unfortunately, σ-coordinates cannot do justice to the stratosphere - which is higly stratified as its name suggests - but pressure levels would be ideal. Starting with JRA 25, all the later reanalyses are produced on hybrid σ-pressure levels (so-called η levels), a compromise between the two systems. For any time t and location defined by latitude ϕ and longitude λ, the kth η level is defined as $p_k(\phi, \lambda, t) = A_k + B_k\, p_s(\phi, \lambda, t)$ (*Stepaniak*, 2008). All the A_k and B_k are constants. The B_k correspond to the σ variable, starting near 1 for the lowest levels and decreasing with altitude, eventually vanishing in the mid-stratosphere (pure pressure levels). The A_k correspond to the pressure increments which are zero near the surface (pure σ-levels) but gradually set the pace as the altitude increases. The JRA 55 archive provides three dimensional data on η levels only : we used the preceding relation to convert it to pressure levels via linear interpolation.

The thickness of an η level is obtained using half levels, designated by half-integer indices : $\Delta p_k = p_{k+.5} - p_{k-.5}$. k ranges from 1 (the highest level) to K (closest to the surface). The vertical integral of any variable $f(p)$ is then approximated by :

$$\int_0^{p_s} f(p)\mathrm{dp} \approx \sum_{n=1}^{N} f(p)(A_{k+.5} - A_{k-.5} + (B_{k+.5} - B_{k-.5}) \cdot p_s) \tag{1.7}$$

Ideally, the numerical vertical integrations should be made on model levels. For NCEP NCAR R1, NCEP DOE R2, NCEP CFSR and JRA 25, we only had specific humidities and winds on pressure levels, from $p_0 = 1000$ hPa to $p_N = 200$ hPa (300 hPa for NCEP NCAR R1) ; above these levels, moisture concentrations become negligible. The value of the variable on the lowest pressure level above the ground was taken to be the value of the variable at the surface. Let p_{n_0} be that level. The vertical integral of any variable $f(p)$ was approximated following the trapezoidal rule :

$$\int_0^{p_s} f(p)\mathrm{dp} \approx \sum_{n=n_0}^{N-1} \frac{1}{2}(f(p_{n+1}) + f(p_n))(p_n - p_{n+1}) + f(p_{n_0})(p_s - p_{n_0}) \tag{1.8}$$

Fluxes on model levels are available in ERA Interim, MERRA and JRA 55 and can be compared with the pressure level estimates. In all four regions considered, the relative differences in mean moisture convergence are below 4% and as low as 2% for the polar cap

Region	Reanalysis	model levels	pressure levels	convergence product
70°-90°N	ERA Interim	194.7	195.8	194.4
	MERRA	202.8	199.6	
	JRA 55	190.5	193.0	
60°-90°N	ERA Interim	257.3	258.3	256.6
	MERRA	265.7	257.7	
	JRA 55	260.5	261.6	
Arctic Ocean	ERA Interim	184.5	184.9	184.5
	MERRA	226.3	217.7	
	JRA 55	185.5	185.5	
Greenland	ERA Interim	177.7	177.6	177.1
	MERRA	395.3	389.9	
	JRA 55	155.2	157.7	
70°-90°S	ERA Interim	174.4	176.0	173.0
	MERRA	185.1	181.5	
	JRA 55	179.2	182.4	
60°-90°S	ERA Interim	335.5	336.4	334.2
	MERRA	345.5	335.3	
	JRA 55	355.8	354.9	
Antarctic ice sheet	ERA Interim	137.4	136.1	134.3
	MERRA	156.5	158.6	
	JRA 55	138.8	140.7	
Antarctic plateau	ERA Interim	47.3	**53.6**	46.4
	MERRA	48.5	**55.4**	
	JRA 55	47.0	**55.6**	

Table 1.4: Effect of the various numerical approximations on the time averaged (1979-2013) moisture convergence in the eight domains studied (kg m^{-2} $year^{-1}$). Red figures indicate relative errors exceeding 5%.

north of 70°N. The effects of the various numerical approximations are summarised in Table 1.4.

We reorganise Equation 1.8 to make the weight given to each level more apparent.

$$
\begin{aligned}
\int_0^{p_s} f(p)\mathrm{dp} \approx & f(p_N)\,\frac{p_{N-1}-p_N}{2} \\
& + \sum_{n=n_0+1}^{N-1} f(p_n)\,\frac{p_{n-1}-p_{n+1}}{2} \\
& + f(p_{n_0})\left(p_s - \frac{p_{n_0+1}+p_{n_0}}{2}\right) + \\
& + \sum_{n=0}^{n_0-1} f(p_n)\cdot 0
\end{aligned}
\tag{1.9}
$$

To avoid the influence of fictitious underground values, we use these weights in our temporal and spatial averages, as in :

$$\overline{q(p_n)} = \frac{1}{t_2-t_1}\,\frac{\int_{t_1}^{t_2} q(p_n,t)\,w_n(t)\,\mathrm{d}t}{\int_{t_1}^{t_2} w_n(t)\,\mathrm{d}t} \tag{1.10}$$

where p_n is a given pressure level and the overbar signals a temporal average between times t_1 and t_2.

To elucidate which time scales contribute most to the net moisture imports, we decompose the winds and humidity into mean and fluctuation (denoted by primes) using monthly averages to filter the synoptic transients as in *Peixóto and Oort* (1992). For a given location and altitude, the mean moisture flux breaks down into two terms, one due to transient eddies, the other to the mean flow :

$$\overline{q\mathbf{v}} = \overline{q{,}\mathbf{v}{,}} + \bar{q}\bar{\mathbf{v}} \tag{1.11}$$

Other applications of the Reynolds decomposition to the atmospheric moisture transport to the polar regions can be found in *Groves and Francis* (2002), *Oshima and Yamazaki* (2006), *Newman et al.* (2012), *Tsukernik and Lynch* (2013) and *Liu and Barnes* (2015a), on individual datasets.

Following *Peixóto and Oort* (1992), we introduce additional notations to refer to the zonal mean, $[q]$, and the vertical mean on pressure levels, $\{q\}$, and the deviations therefrom, q° and q^*. After vertical and zonal averaging of the meridional flux, we further decompose the mean flow term :

$$
\begin{aligned}
\{[\bar{q}\bar{v}]\} = & \{[\overline{q{,}v{,}}]\} + \{[\bar{q}^*\bar{v}^*]\} \\
& + \{[\bar{q}]^\circ[\bar{v}]^\circ\} + \{[\bar{q}]\}\{[\bar{v}]\}
\end{aligned}
\tag{1.12}
$$

The first term on the right hand side groups the contribution of small-scale, short-lived, “transient eddies,” including extratropical cyclones. The second term is the product of the zonal anomalies of the mean humidity and wind fields which are designated as “stationary eddies.” For instance, in the North Atlantic at 70°N, the air is particularly moist and the meridional wind is particularly strong compared to other longitudes. The third term on the right-hand side corresponds to the product of vertical anomalies in the zonally symmetric time mean humidity and wind fields, known as “vertical cells” by reference to the overturning circulations of the Hadley, Ferrel and polar cells. The fourth and last term should be zero because there is no net mass flux into a closed region on yearly time scales. We will test this assumption shortly.

Equation 1.12 involves the meridional wind averaged along time, longitude and over the full height of the atmosphere. For most reanalyses, our wind data is limited to an altitude of $p_N = 200$ hPa, i.e. four fifths of the mass of the atmosphere. To cover the last fifth, we would need three times the current amount of vertical levels. Indeed, as shown in Table 1.1, we only use one third of the available levels, at least for the modern reanalyses. We can circumvent this problem by invoking the conservation of mass. We integrate Equation 1.2 over the polar cap north of latitude ϕ_0 on the horizontal, and between the top of the atmosphere (0 hPa) and p_N on the vertical. Moist processes can be safely neglected at these altitudes.

$$\int_0^{p_N} \iint_{\phi>\phi_0} \mathrm{div}\vec{u}\ \mathrm{d}s\frac{\mathrm{d}p}{g} + \iint_{\phi>\phi_0} \int_0^{p_N} \frac{\partial\omega}{\partial p}\frac{\mathrm{d}p}{g}\mathrm{d}s = 0 \tag{1.13}$$

$$\int_0^{p_N}\int_0^{2\pi} v(\phi_0)\ \mathrm{d}\lambda\frac{\mathrm{d}p}{g} = \iint_{\phi>\phi_0}\omega(p_N)\ \mathrm{d}s \tag{1.14}$$

The mean mass flux into the polar cap is therefore :

$$\{[v]\}\cdot\int_{p_s}^{p_N}\int_0^{2\pi}\mathrm{d}\lambda\frac{\mathrm{d}p}{g} = \int_{p_s}^{p_N}\int_0^{2\pi} v(\phi_0)\,\mathrm{d}\lambda\frac{\mathrm{d}p}{g} + \iint_{\phi>\phi_0}\omega(p_N)\,\mathrm{d}s \tag{1.15}$$

We will often be implicitely multiplying the terms of Equation 1.12 by the mean column mass along the domain boundary, to express the fluxes in units of kg $\mathrm{m}^{-1}\mathrm{s}^{-1}$. A further division by the surface of the domain considered yields units of kg $\mathrm{m}^{-2}\mathrm{s}^{-1}$, or in the case of water fluxes : mm s^{-1}. For south polar caps, the northward wind is replaced with the southward wind. For more complex domains like the Antarctic ice sheet, [.] will refer to averages along the boundary of the domain. In these cases, it is more convenient to write the first term on the right-hand side as a divergence.

We integrate Equation 1.2 over the polar cap, this time from the top of the atmosphere to the surface. At more humid altitudes, atmospheric mass may be lost in the form of net precipitation (*Trenberth et al.*, 2011). To put it concisely,

$$\{[\bar{v}]\} - \{[\overline{qv}]\} = 0 \tag{1.16}$$

Let $\{[\overline{v_{nd}}]\}$ be the residual of this equation, "nd" standing for non-divergent. In practice, this residual term is not zero and it causes a non-physical advection of moisture (Table 1.5). For wide domains, such as polar caps, the impact on the moisture budget is limited. The problem is more serious over the Greenland and Antarctic ice sheets, particularly in the first generation reanalyses.

Throughout this study, we used each reanalysis' output grid to perform all computations : Reynolds decomposition, vertical integrations, spatial averages, etc. When necessary for the comparison and as a last stage, we bilinearly interpolated the derived products on a common grid (0.5° × 0.5° latitude-longitude).

Region	Reanalysis	mass convergence $\{[\bar{v}]\}$	moisture convergence $\{[\overline{qv}]\}$	moisture leak $\{[\bar{q}]\}\{[\overline{v_{nd}}]\}$
70°-90°N	NCEP NCAR R1	1.2e+03	191.7	0.8
	NCEP DOE R2	4.3e+02	199.5	0.2
	JRA 25	3.2e+03	187.2	2.1
	ERA Interim	-1.6e+03	194.7	-1.3
	NCEP CFSR	-3.0e+03	191.8	-2.4
	MERRA	6.8e+02	202.8	0.4
	JRA 55	4.4e+02	190.5	0.2
60°-90°N	NCEP NCAR R1	-8.2e+02	270.3	-1.2
	NCEP DOE R2	2.3e+02	270.9	-0.0
	JRA 25	2.6e+03	259.3	2.4
	ERA Interim	-4.7e+02	257.3	-0.8
	NCEP CFSR	-1.9e+03	260.3	-2.3
	MERRA	-9.8e+02	265.7	-1.3
	JRA 55	-5.5e+02	260.5	-0.8
Arctic Ocean	NCEP NCAR R1	9.6e+03	193.9	7.0
	NCEP DOE R2	9.6e+03	206.6	7.0
	JRA 25	1.9e+03	183.0	1.2
	ERA Interim	-1.6e+03	205.3	-1.3
	NCEP CFSR	-3.2e+03	204.1	-2.5
	MERRA	2.6e+03	226.3	1.7
	JRA 55	2.7e+03	188.3	1.7
Greenland	NCEP NCAR R1	-1.1e+05	364.4	**-69.7**
	NCEP DOE R2	-5.7e+04	336.6	**-35.2**
	JRA 25	1.4e+04	398.2	7.4
	ERA Interim	-8.9e+03	326.8	-5.4
	NCEP CFSR	-3.2e+03	289.2	-2.1
	MERRA	-5.9e+02	395.3	-0.6
	JRA 55	-2.5e+04	329.1	-14.2
70°-90°S	NCEP NCAR R1	-9.6e+03	176.6	-3.7
	NCEP DOE R2	-2.8e+03	175.7	-1.2
	JRA 25	4.5e+03	184.5	1.6
	ERA Interim	3.0e+03	174.4	1.1
	NCEP CFSR	9.9e+02	174.7	0.3
	MERRA	1.1e+03	185.1	0.3
	JRA 55	-1.2e+03	179.2	-0.5
60°-90°S	NCEP NCAR R1	-3.3e+03	334.0	-3.2
	NCEP DOE R2	3.7e+02	333.9	0.0
	JRA 25	-5.4e+02	308.6	-0.7
	ERA Interim	3.8e+02	335.5	0.0
	NCEP CFSR	-1.0e+03	353.3	-1.1
	MERRA	3.3e+03	345.5	2.2
	JRA 55	3.2e+03	355.8	2.2
Antarctic ice sheet	NCEP NCAR R1	-5.7e+04	116.5	**-20.5**
	NCEP DOE R2	-3.5e+04	113.9	**-12.8**
	JRA 25	-1.4e+04	147.1	-5.0
	ERA Interim	-9.7e+02	137.2	-0.4
	NCEP CFSR	-4.4e+03	119.9	-1.7
	MERRA	-1.2e+03	156.5	-0.5
	JRA 55	-1.8e+04	138.7	-6.2
Antarctic plateau	NCEP NCAR R1	-4.3e+03	54.5	-0.1
	NCEP DOE R2	-3.8e+03	54.2	-0.5
	JRA 25	1.1e+04	59.5	1.2
	ERA Interim	2.3e+04	47.3	**2.8**
	NCEP CFSR	3.1e+04	52.5	**3.6**
	MERRA	-2.0e+03	48.5	-0.2
	JRA 55	9.9e+02	47.0	0.1

Table 1.5: Total mass convergence, total moisture convergence and spurious moisture convergence averaged over the 1979-2013 period (in kg m^{-2} $year^{-1}$). The font is red when the spurious moisture convergence represents more than 5% of the total.

CHAPTER 2
Moisture advection to the Arctic

2.1 Spatial structure

We now examine the Arctic atmospheric hydrological cycle as represented by the seven reanalyses studied, with an emphasis on moisture transport. Whenever possible, we compare the reanalyses to the radiosonde observations.

To the first order, the mean vertically integrated moisture fluxes north of 60°N in ERA Interim follow an eastward zonally symmetric flow with magnitudes of approximately 25 kg $m^{-1}s^{-1}$ (Figure 2.1, a). The magnitudes decrease with latitude following the decreasing temperature and humidity, from 70 kg $m^{-1}s^{-1}$ over Northern Europe to zero over the central Arctic. Deviations occur from the zonal pattern, particularly in the northern North Atlantic as shown in Figure 2.1 (b). Transport over the Denmark Strait is clearly influenced by the cyclonic circulation associated with the Icelandic Low. Over the Norwegian Sea, the transport is the most intense (more than 80 kg $m^{-1}s^{-1}$) and exhibits a definite northward component. Over Alaska and the Bering Strait, the transport is weaker in magnitude (approximately 50 kg $m^{-1}s^{-1}$) but is directed straight towards the North Pole ; the same holds for the Labrador Sea and the Davis Strait.

The other datasets correspond well with the broad features of this climatology. As shown in Figure 2.1 (c), the differences between the mean moisture transport in ERA Interim and in the other reanalyses are on the order of 10 kg $m^{-1}s^{-1}$, constituting approximately one fifth to one fourth of the mean transport magnitude. The differences in model resolution are likely the reason for the larger spread over regions with complex orography such as Alaska, Scandinavia and Greenland. The first generation datasets, NCEP NCAR R1 and NCEP DOE R2 (turquoise and orange arrows in Figure 2.1, c and d), are often in disagreement with the other reanalyses in these areas. Their relatively coarse resolution (T62, 2.5°) does not allow fine-scale features to be adequately captured, such as off the southwestern shore of Greenland. In the higher resolution versions of Figure 2.1 (not shown here), the ensemble spread was not appreciably reduced in the vicinity of the radiosonde sites.

The longitude distribution of moisture transports at 70°N confirms the consensus among

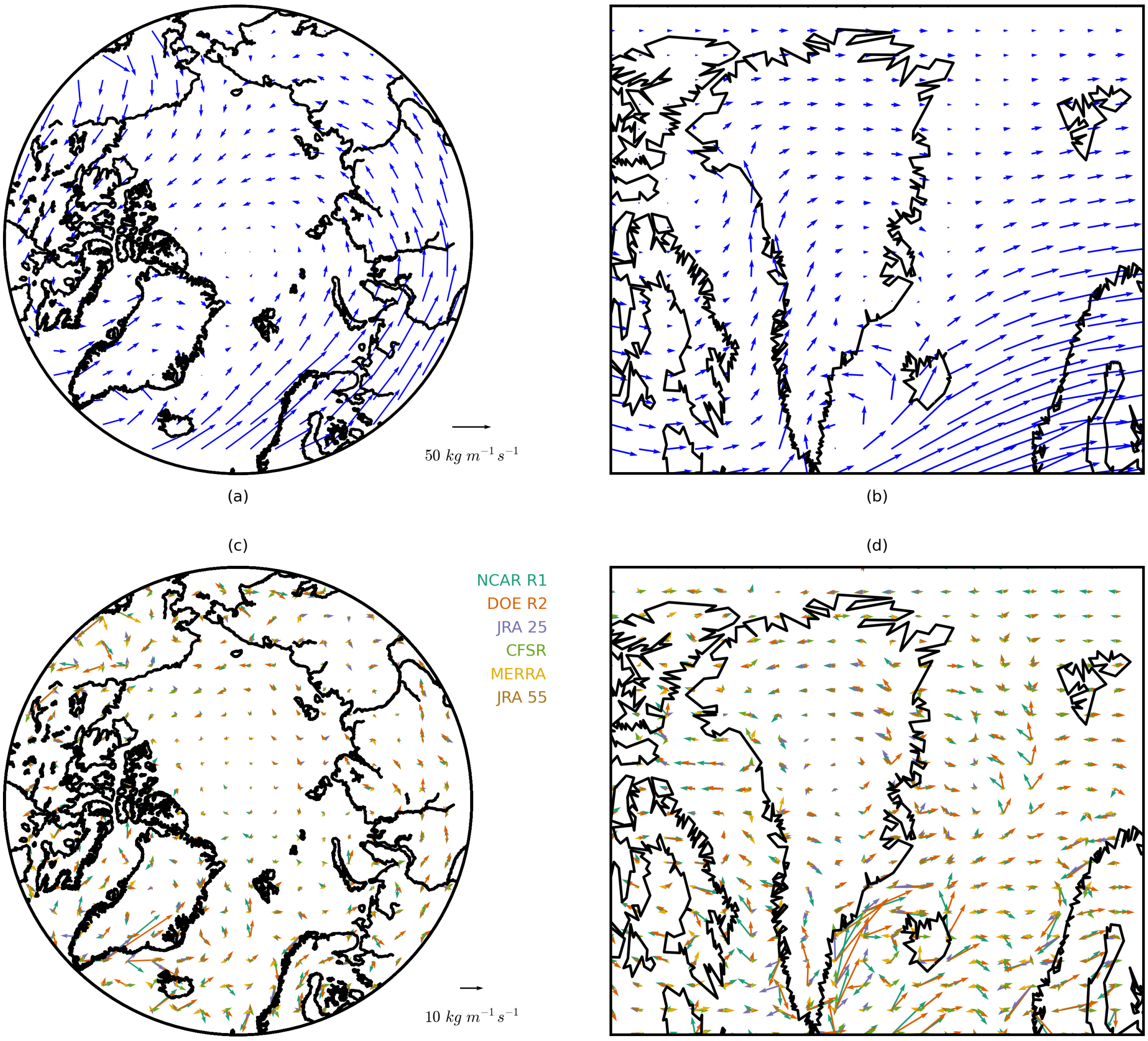

(a)

(b)

(c)

(d)

Figure 2.1: Time-averaged (1979-2013) vertically integrated moisture flux north of 60°N in ERA-Interim (a) and, with the same arrow scale, a zoom on the northern North Atlantic (b). Panels (c) and (d) show the differences in vertically integrated moisture flux between the other 6 reanalyses and ERA-Interim (same arrow scales).

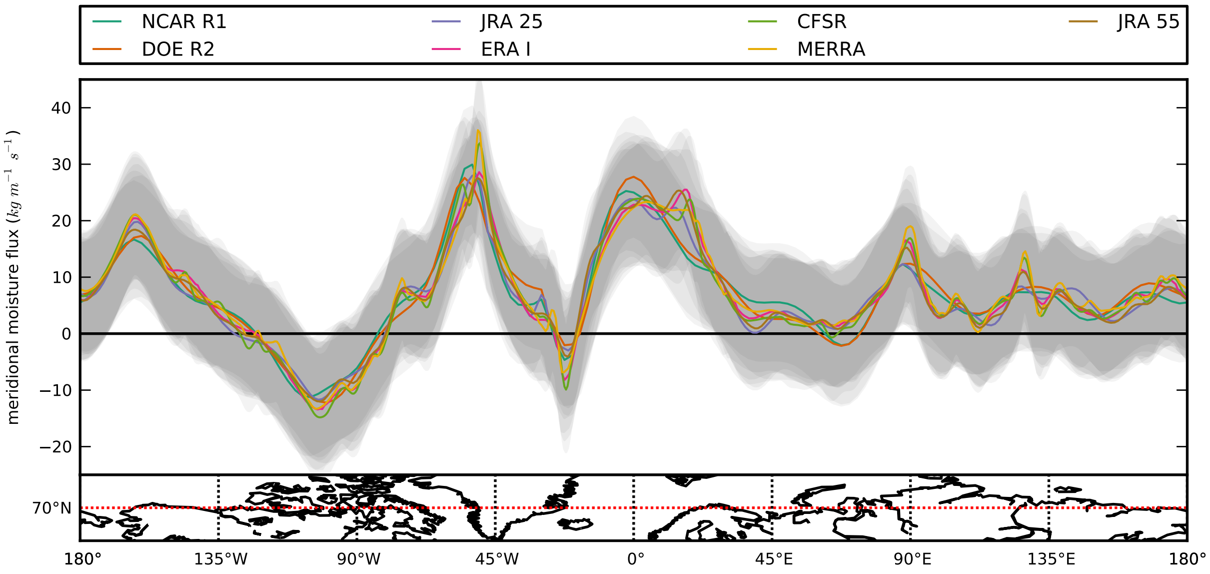

Figure 2.2: Longitudinal distribution of the climatological vertically integrated meridional moisture flux at 70°N in different reanalyses (1979-2013). The grey shaded bands indicate the ranges corresponding to plus or minus one interannual standard deviation from the mean.

different reanalyses (Figure 2.2). No dataset shows systematically lower or higher climatological moisture transport. The differences across products are within the range of interannual variability, except for the above mentioned regions of large disagreement. There, the longitude profiles of the modern reanalyses reflect the rugged relief beneath when the first-generation datasets smooth it out.

To evaluate the reliability of the moisture transport estimates in the reanalyses, we compared them to the IGRA radiosonde observations described in section 1. Considering climatological fluxes, the observed longitudinal pattern is broadly respected by the reanalyses (Figure 2.3, a). Aside from two outliers (Petchora station in the Northern Ural Mountains, and Narsarsuaq station in Greenland), correlations between moisture flux monthly anomalies in reanalyses and radiosoundings are higher than 0.85 (not shown). CFSR typically exhibits the best performance, followed by ERA Interim. JRA 25 often performs better than JRA 55 perhaps because the former relies more on satellite data.

Overall, the absolute moisture fluxes measured by radiosondes are lower than in the reanalyses regardless of whether the moisture is blowing north or south. The relative difference between the filtered observations and the subsampled ERA Interim is 10.2% when averaged over all radiosonde sites (Table 1.2). This difference is minimal in NCEP NCAR R1 (6.3%) and maximal in MERRA (13.2%). We sought an explanation in the representation of the

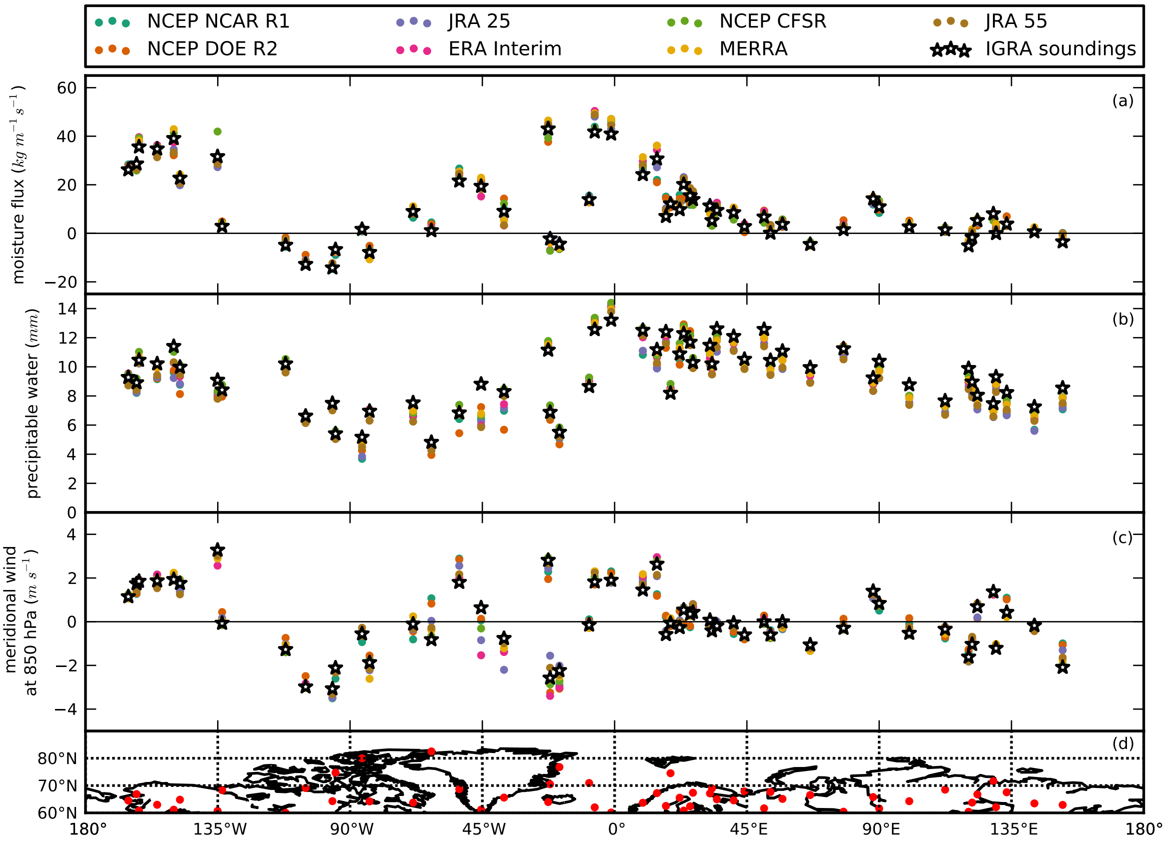

Figure 2.3: Climatological vertically integrated meridional moisture flux derived from reanalyses and radiosoundings (1979-2013) at the location of the radiosonde stations (a), idem for precipitable water (b) and for the meridional wind at 850 hPa (c). Panel (d) gives the location of the radiosonde stations.

humidity and wind in either dataset (Figure 2.3, b and c, respectively). Precipitable water is higher in the observations than in the reanalyses, but the meridional wind at 850 hPa (where moisture fluxes are strongest) is neither systematically higher nor lower. The mean precipitable water and wind at 850 hPa are not related to the mean vertically integrated moisture flux : this suggests that humidity and wind are correlated, both in time and along the vertical.

The vertical profiles confirm that fluxes are weaker when derived from radiosondes and that this difference is not a side effect of the vertical integrations (Figure 2.4, a). The reanalyses correspond well with the observations above 700 hPa, but overestimate the fluxes below that level. Only ERA Interim and JRA 25 capture the altitude of the maximum flux, at 850 hPa. The older NCEP reanalyses place it lower, below 900 hPa, whereas CFSR, JRA 55 and MERRA have local maxima at both heights. The specific humidity is well reproduced by the reanalyses, except in the boundary layer (Figure 2.4, b). Below 900 hPa, the radiosonde observations report two humidity inversions that are not captured by the reanalyses. MERRA and JRA 55 show a single humidity inversion but overestimate its strength. The spread between datasets is greater for the mean meridional wind variable (Figure 2.4, c). The observed winds are weaker in the upper troposphere but are within the reanalysis envelope below 600 hPa. Below this level, the winds shift from northward to southward. This change of sign in the wind direction is absent in the moisture flux profile indicating that the mean flow is not the main cause of moisture advection in the Arctic.

The vertical pattern of correlation of reanalyses' moisture transport with IGRA's is more disconcerting (Figure 2.4, d). ERA Interim and CFSR systematically outmatch the other with values of approximately 0.9 for the bulk of the free troposphere. These reanalyses do not perform as well near the surface or the tropopause, but this is insignificant compared with the other reanalyses, which achieve coefficients superior to 0.8 only in the layer between 700 and 500 hPa. This result is perplexing given the high correlation with the IGRA soundings of the vertically integrated quantities in all datasets. Some datasets probably reject the radiosonde observations in the upper and higher troposphere but the data from the middle troposphere is sufficient to reconstruct a plausible albeit inaccurate vertical profile.

The specific humidity and meridional wind variables exhibit the same vertical correlation patterns as the moisture flux except in the upper troposphere : the wind in ERA Interim and CFSR remains highly correlated with the soundings even higher than 500 hPa (Figure 2.4, e and f).

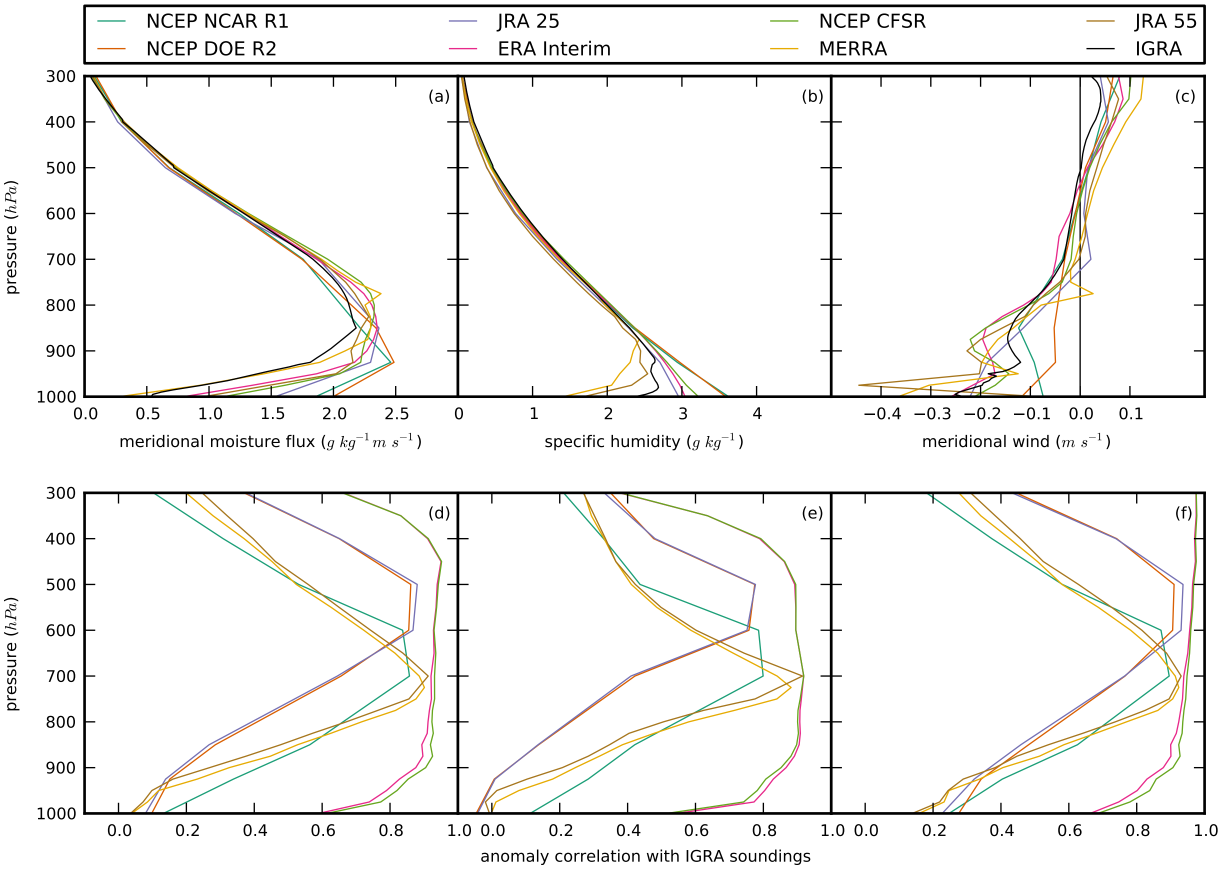

Figure 2.4: Mean vertical profiles of the seven reanalyses co-located with the selected radiosonde sites and averaged over all these sites for the meridional moisture flux (a), specific humidity (b) and meridional wind (c). The lower panels show the correlations between the said variables in reanalyses and in the radiosoundings.

2.2 Long-term moisture budgets

Table 2.1 and Figure 2.5 present the terms of the moisture budget in the different datasets for four regions : north of 70°N, north of 60°N, the Arctic Ocean and the Greenland ice sheet. The mean moisture convergence through 70°N is remarkably consistent between the seven reanalyses studied because they are constrained by common observations despite different model settings and resolutions. The minimum value (187 mm year^{-1}) is given by JRA 25 and the maximum (203 mm year^{-1}) by MERRA. In line with our findings in the previous section, the fluxes derived from radiosondes (*Serreze et al.*, 1995) or computed from satellite data (*Groves and Francis*, 2002) tend to be lower than the reanalysis values. Estimates of precipitation and evaporation are more scattered among datasets ; net precipitation computed from model physics ranges from 95 mm year^{-1} (NCEP DOE R2) to 244 mm year^{-1} (NCEP CFSR). The interdataset standard deviation for net precipitation is 45 mm year^{-1} compared to 5.1 mm year^{-1} for transport.

Predictably, no reanalysis succeeds in closing the moisture budget, with the largest mismatch found in NCEP DOE R2, where the moisture convergence exceeds net precipitation by 52%. This mismatch is smaller in the other datasets (although still 34% for MERRA). CFSR exhibits the most intense water cycle. Net precipitation is higher than the moisture convergence only in CFSR and JRA 55.

For the polar cap north of 60°N, the results of *Bengtsson et al.* (2004a) using ERA-Interim from 1989 to 2005 are congruent with our estimates from 1979 to 2013 for evaporation and transport but not precipitation (7% relative difference). Our precipitation estimates were computed as accumulated values by the numerical weather prediction model between the initialisation and the first twelve hours of forecast. *Bengtsson et al.* (2004a) preferred a time window shifted 18 hours from the analysis to avoid the model spin-up effects. At such lead times, net precipitation (physics output method) overshoots the transport estimates (aerological method).

We performed a similar budget analysis for the Arctic Ocean and the Greenland ice sheet. Atmospheric moisture convergence represents an important source term in the Arctic freshwater budget impacting ocean stratification, convection, the intensity of the thermohaline circulation and the formation of sea ice (*Serreze et al.*, 2006). For Greenland, net precipitation along with meltwater runnoff and blowing snow determine the surface mass balance of the ice sheet (*Ettema et al.*, 2009; *Burgess et al.*, 2010). Despite the warnings from *Bengtsson*

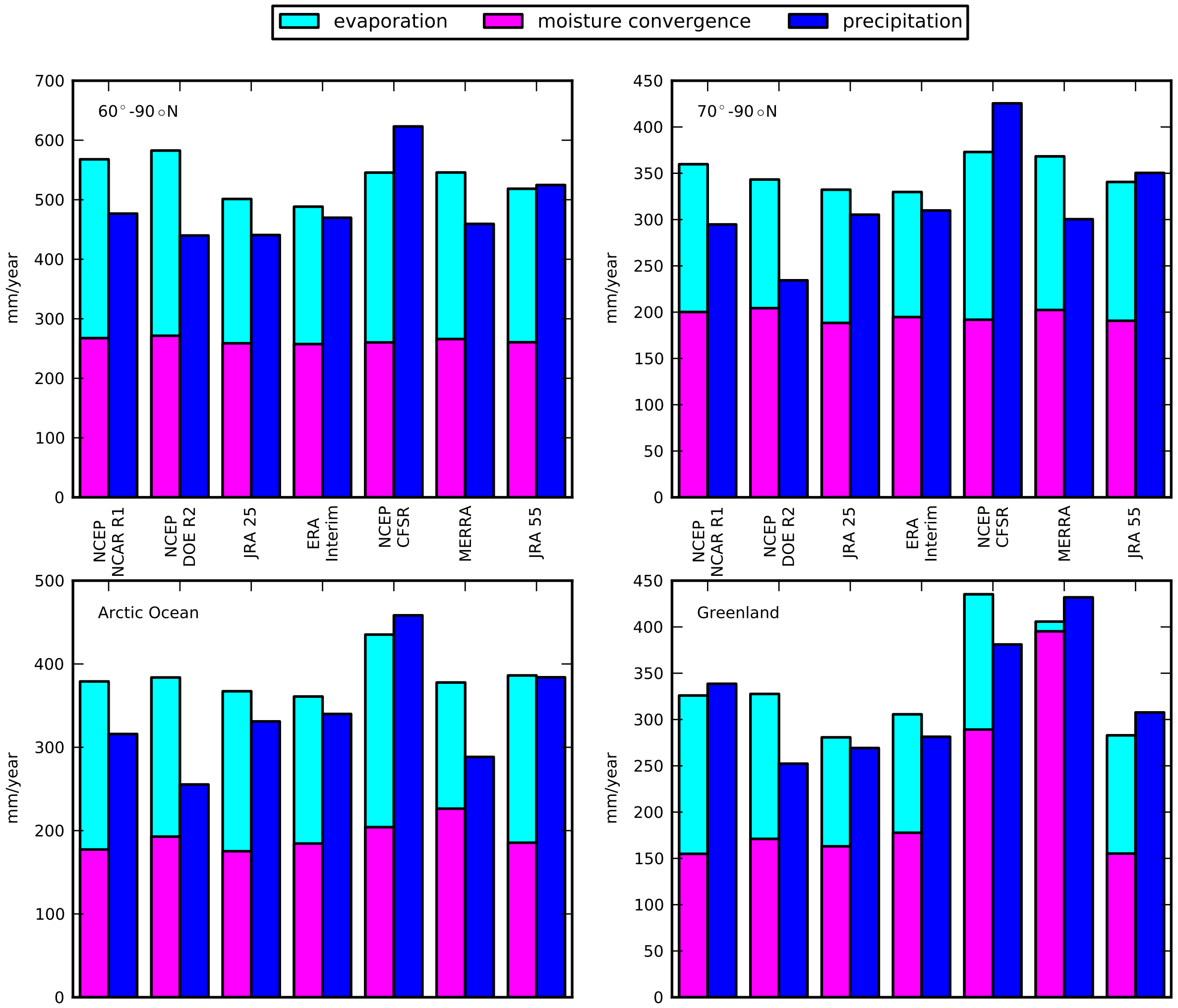

Figure 2.5: Histogram of the long-term averaged (1979-2013) moisture budget terms (mm year^{-1}) for the polar caps north of 70°N and north of 60°N, the Arctic Ocean and the Greenland ice sheet.

Region	Source	Period	P	E	P-E	T	P-E-T
70°-90°N	*Serreze et al.* (1995)	1974-1991				163	
	Bromwich et al. (2000)	1979-1993				189 (23)	
	Groves and Francis (2002)	1979-1998				151	
	Jakobson and Vihma (2010)	1979-2001	323 (23)	144 (9)	179 (20)	192 (16)	-13
	Cullather and Bosilovich (2011)	1979-2005	299 (16)	167 (7)	132 (16)	205 (15)	-73
	NCEP NCAR R1	1979-2013	295 (16)	160 (14)	135 (14)	192 (14)	-57 (12)
	NCEP DOE R2	1979-2013	234 (21)	139 (15)	95 (15)	199 (14)	-104 (12)
	JRA 25	1979-2013	305 (17)	144 (10)	161 (19)	187 (14)	-26 (16)
	ERA Interim	1979-2013	310 (14)	135 (9)	175 (14)	195 (13)	-20 (8)
	NCEP CFSR	1979-2013	426 (18)	181 (9)	244 (16)	192 (15)	53 (9)
	MERRA	1979-2013	300 (15)	166 (7)	134 (16)	203 (15)	-68 (16)
	JRA 55	1979-2013	350 (14)	150 (9)	200 (14)	190 (14)	10 (5)
60°-90°N	*Bengtsson et al.* (2011)	1989-2009	509	236	273	258	15
	NCEP NCAR R1	1979-2013	477 (18)	300 (11)	176 (17)	270 (10)	-94 (13)
	NCEP DOE R2	1979-2013	440 (29)	311 (18)	129 (16)	271 (11)	-142 (13)
	JRA 25	1979-2013	441 (19)	242 (7)	198 (20)	259 (9)	-61 (16)
	ERA Interim	1979-2013	470 (13)	231 (6)	239 (13)	257 (10)	-18 (7)
	NCEP CFSR	1979-2013	623 (20)	285 (8)	338 (16)	260 (12)	78 (8)
	MERRA	1979-2013	459 (20)	280 (5)	179 (18)	266 (12)	-86 (11)
	JRA 55	1979-2013	525 (14)	258 (7)	267 (12)	260 (11)	6 (7)
Arctic Ocean	*Serreze et al.* (2006)	1979-2001	310	130	190	210 (21)	
	Cullather and Bosilovich (2011)	1979-2005	285 (17)	150 (8)	135 (17)	213 (17)	-78
	NCEP NCAR R1	1979-2013	316 (16)	202 (15)	114 (16)	177 (17)	-63 (11)
	NCEP DOE R2	1979-2013	255 (19)	191 (18)	64 (16)	193 (18)	-128 (12)
	JRA 25	1979-2013	331 (20)	192 (11)	139 (23)	175 (18)	-36 (17)
	ERA Interim	1979-2013	340 (16)	176 (11)	164 (18)	184 (17)	-21 (9)
	NCEP CFSR	1979-2013	458 (20)	231 (12)	227 (19)	204 (18)	23 (18)
	MERRA	1979-2013	288 (16)	151 (8)	137 (17)	226 (17)	-89 (17)
	JRA 55	1979-2013	384 (16)	201 (11)	183 (18)	185 (18)	-2 (7)
Greenland	*Ettema et al.* (2009)	1958-2007	434 (23)	15	419		
	Burgess et al. (2010)	1979-2005			344 (23)		
	Cullather and Bosilovich (2011)	1979-2005	434 (46)	9 (2)	424 (47)	459 (44)	-35
	NCEP NCAR R1	1979-2013	339 (26)	171 (20)	168 (28)	155 (26)	13 (26)
	NCEP DOE R2	1979-2013	252 (29)	157 (14)	96 (28)	171 (28)	-75 (27)
	JRA 25	1979-2013	269 (24)	118 (10)	152 (25)	163 (22)	-12 (22)
	ERA Interim	1979-2013	281 (24)	128 (12)	153 (23)	178 (22)	-24 (9)
	NCEP CFSR	1979-2013	381 (39)	146 (11)	235 (31)	289 (38)	-54 (50)
	MERRA	1979-2013	432 (44)	11 (3)	421 (45)	395 (39)	26 (19)
	JRA 55	1979-2013	308 (25)	128 (10)	180 (21)	155 (20)	25 (11)

Table 2.1: Long-term averaged (1979-2013) moisture budget terms (mm year^{-1}) for the polar caps north of 70°N and north of 60°N, the Arctic Ocean and the Greenland ice sheet : T refers to the total poleward moisture transport, P to precipitation and E to evaporation. Values in brackets are the interannual standard deviations. This table is adapted from *Cullather and Bosilovich* (2011).

et al. (2011), integrating fluxes on pressure levels has only a moderate impact on the results even over these complex domains (Table 1.4). The maximum relative error (3.8%) is found in MERRA over the Arctic Ocean. Even when applying the same time window (1979-2005), we were unable to reconcile our estimate of the moisture convergence over the Greenland ice sheet using MERRA (393 mm year^{-1}) with that of *Cullather and Bosilovich* (2011) (459 mm year^{-1}). This mismatch does not apply to precipitation and evaporation.

2.3 Role of the mean flow and transient eddies

We now turn to the analysis of the moisture transport into the Arctic using the decomposition given by Equation 1.11. Figure 2.6 shows the climatological mean moisture transport due to the mean flow and transient eddies as represented in ERA Interim. Driven by the westerly winds, the mean flow is largely responsible for the zonal component of the total transport. The transient eddy flux is one order of magnitude weaker but is nearly exclusively meridional suggesting its dominant contribution to the poleward advection of moisture. However, the mean flow flux is not consistently zonal ; it has relatively small meridional components. Given the large magnitude of the mean flux, it also contributes to the moisture advection toward or away from the Arctic. For example, approximately half of the total northward flux over the storm tracks is due to the mean flow component.

Over the Canadian archipelago and Strait of Denmark, the mean flow transport imparts a southward direction to the total transport, offsetting the effect of the transients. The explanation is found in *Peixóto and Oort* (1992) and the standing wave pattern the authors identified in the mean tropopause winds. One of the two troughs is located East of the American continent implying southward winds over Canada and northward winds over the Baffin Bay and the Greenland Sea. Over Canada, these southward winds extend to the surface, so the mean flow flux in this region is also southward. Over the Strait of Denmark, the high northward winds advect a small amount of moisture compared to the southward surface winds associated with the Icelandic low, because the air is more humid near the surface. As a result, the vertically integrated mean flow flux is directed south between Greenland and Iceland.

To estimate the role of the transport components in different datasets, we apply the same decomposition (Equation 1.11) to all seven reanalyses for the meridional transport component at latitude 70°N. Figure 2.7 illustrates that the contribution of the transient

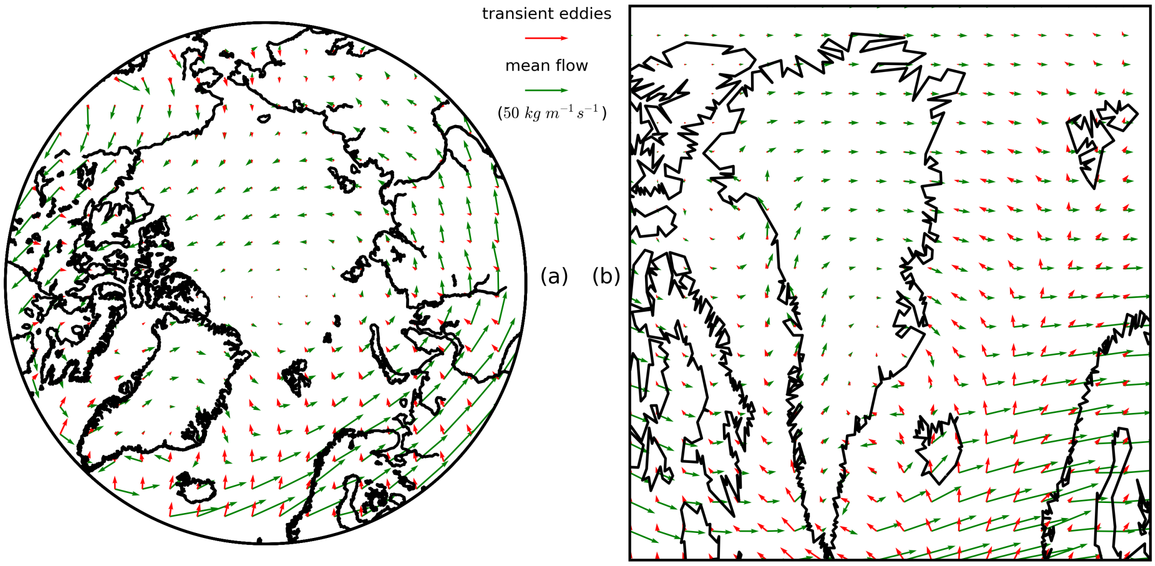

Figure 2.6: Reynolds decomposition (Equation 1.11) of the moisture fluxes in ERA-Interim : north of 60°N (a) and with the same arrow scale, a zoom on the northern North Atlantic (b).

eddy transport peaks at the end of the Atlantic and Pacific storm tracks, which are common features of all reanalyses (*Tilinina et al.*, 2013). The mean flow leads to both southward transport (e.g. at longitudes 135°W-90°W, 45°E-90°E) and northward transport (e.g. at 180°-135°W, 0°-45°E) that cancel each other in zonal mean. Consequently, poleward transient eddy fluxes are responsible for the bulk of the meridional moisture transport, reflecting the prominent role of cyclones in the moisture advection. The dominant role of transient eddies in the total northward moisture flux is particularly evident between 70°N and 75°N for all datasets (Figure 2.8, a and b).

All reanalyses reveal the signature of the polar cell in the form of a southward flux of water vapour between 60 and 75°N (Figure 2.8, a). The vertical profile of the transport confirms the presence of a vertical circulation cell whose lower branch (below 600 hPa) works to advect the moist surface air towards the South (Figure 2.8, c). While representing only a small fraction of the total flux, this component is likely to increase (in its absolute value) in a warmer and thus moister atmosphere.

Table 2.2 presents the mean and standard deviation of all components of the decomposition from Equation 1.12 for the moisture flux at 70°N.

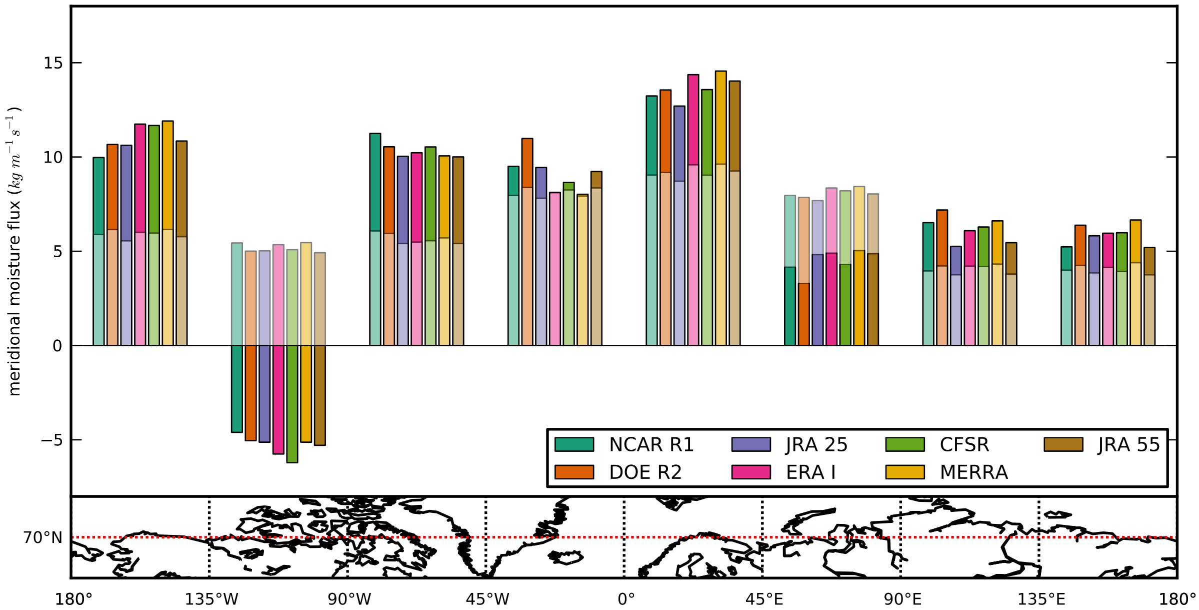

Figure 2.7: Longitudinal distribution of the vertically integrated total moisture transport at 70°N (solid bars) and its transient eddy component (from Equation 1.11, semi-transparent bars ; all bars start from zero) in the seven reanalyses. Each set of bars correspond to the average over 45-degree longitudinal bands, defined in the map in the lower panel.

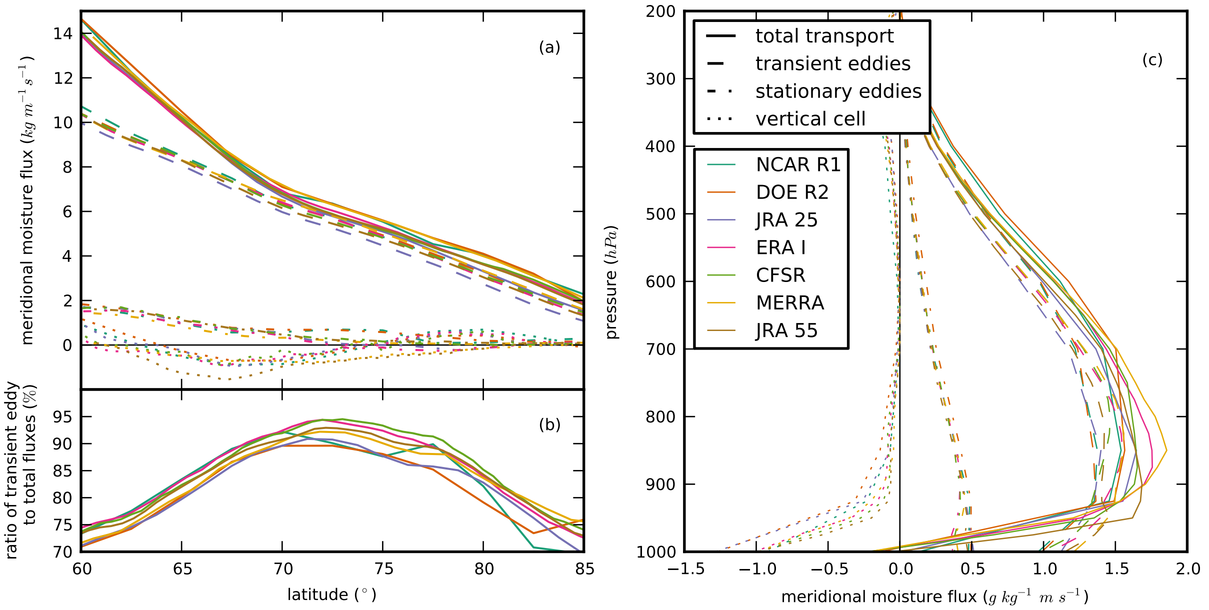

Figure 2.8: Meridional distribution in absolute (a) and relative values (b) of the different terms of the Reynolds decomposition (Equation 1.12) of the meridional moisture flux and their vertical profiles at 70°N (c).

Reanalysis	total $\{[\bar{q}\bar{v}]\}$	transient eddies $\{[\overline{q'v'}]\}$	stationary eddies $\{[\bar{q}^*\bar{v}^*]\}$	vertical cell $\{[\bar{q}]^\circ[\bar{v}]^\circ\}$	residual $\{[\bar{q}]\}\{[\overline{v_{nd}}]\}$
NCEP NCAR R1	192 (14)	176 (10)	40 (9)	-26 (7)	0.8 (0.0)
NCEP DOE R2	199 (14)	178 (10)	45 (10)	-24 (8)	0.2 (0.0)
JRA 25	187 (14)	167 (9)	40 (9)	-22 (7)	2.1 (0.0)
ERA Interim	196 (13)	180 (11)	40 (9)	-23 (6)	-1.3 (0.0)
NCEP CFSR	192 (15)	176 (11)	40 (10)	-22 (6)	-2.4 (0.0)
MERRA	200 (14)	183 (11)	42 (10)	-30 (7)	0.4 (0.0)
JRA 55	193 (14)	173 (10)	41 (10)	-25 (8)	0.2 (0.0)

Table 2.2: Long-term averaged (1979-2013) components of the moisture convergence north of 70°N (mm year^{-1}) according to Equation 1.12. $\{[\bar{v_{nd}}]\}$ is the residual of Equation 1.16. Values in brackets are the interannual standard deviations.

2.4 Seasonal variability

The seasonal variability of the moisture advection into the Arctic is important because mid-latitude and subpolar stormtracks and atmospheric humidity undergo significant changes throughout the year. The seasonal march of net precipitation over the Arctic is pronounced because precipitation and evaporation are strongly dependent on the seasonal variations in sea ice extent. All reanalyses show a similar seasonal behaviour of moisture convergence north of 70°N (Figure 2.9). The maximum of moisture convergence ($\sim$ 25 mm month^{-1}) is observed in July in all reanalyses except for NCEP NCAR R1 and NCEP DOE R2 which lag by one month compared to the other products. A winter minimum of about 12 mm month^{-1} is observed from December to March. The moisture transport component associated with transient eddies accounts for nearly the entire moisture convergence, providing up to 90% in winter and summer and up to 100% in the interseasons.

The annual peak of moisture transport is more acute over the radiosonde sites and occurs in September (Figure 2.10, a). As noted previously, the observed fluxes are weaker than in the reanalyses, particularly in spring, summer and early autumn.

The maximum net precipitation lags by approximately one month with respect to the moisture convergence and is observed in August in all products, except for JRA 25, for which the maximum is observed in September. The reason for this lag is in part physical : during the warm season, the water holding capacity of an atmospheric column increases (Figure 2.9, red curve), limiting the potential for the imported and evaporated moisture to precipitate.

Figure 2.10 (b) shows the annual cycle of precipitable water over the chosen radiosonde locations, which reaches a maximum in July, two months before the peak in moisture trans-

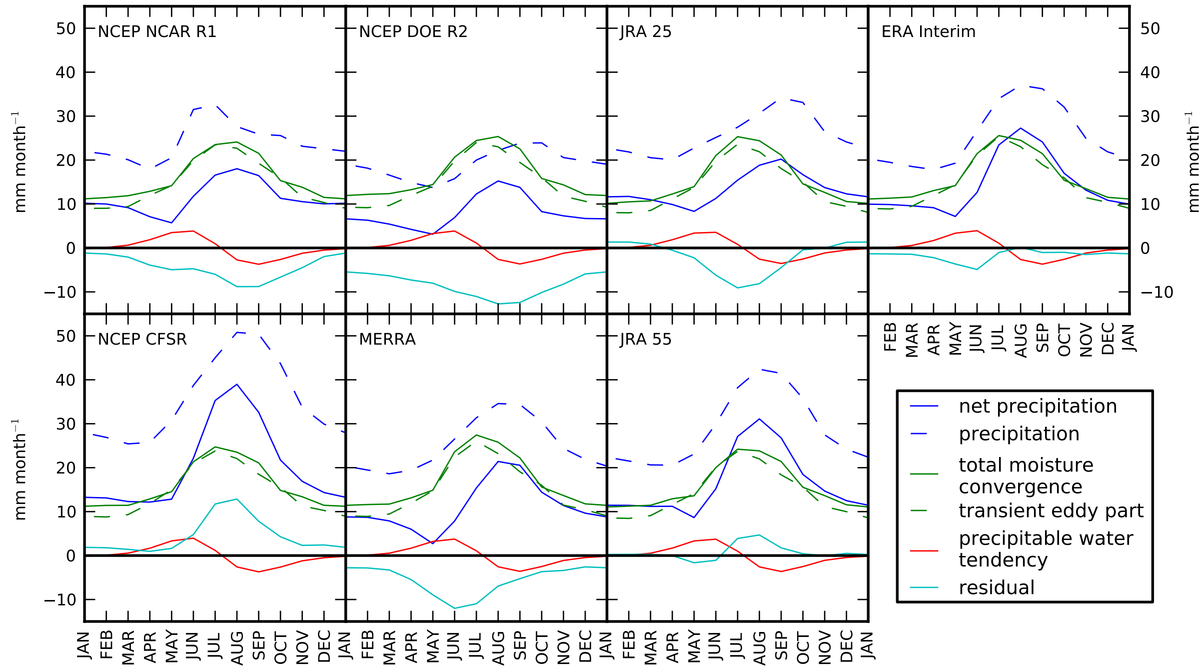

Figure 2.9: Seasonal cycle of the moisture budget for the polar cap north of 70°N. The residual term is equal to net precipitation minus convergence minus the rate of change of precipitable water.

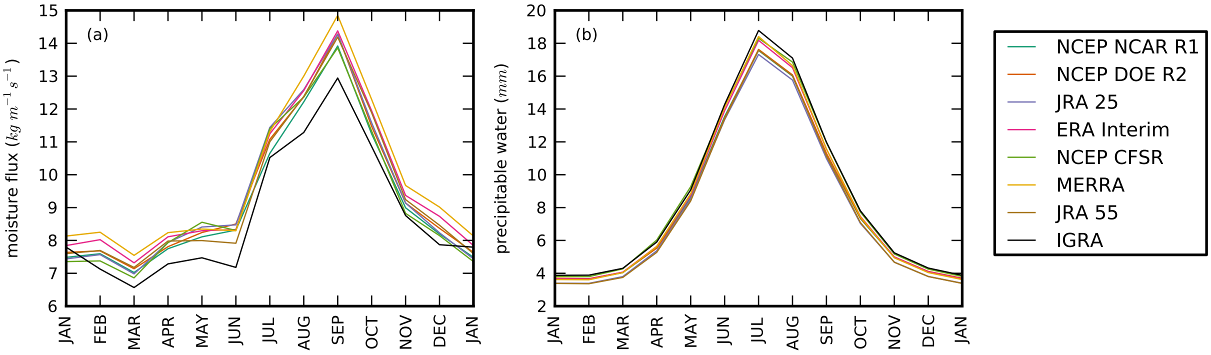

Figure 2.10: Annual cycle of the meridional moisture flux (a) and of precipitable water (b) in reanalyses and IGRA, averaged over all the radiosonde sites.

port.

However, a portion of the lag in Figure 2.9 can be interpreted as an artifact because the right and the left-hand sides of the moisture balance equation (Eq. 1.5) are computed independently. The water budget is thus unlikely to be closed, as indicated by the residual term in Figure 2.9 (light blue curve). The same applies to the energy budget ; for example, in MERRA the surface receives an excess of 11 W m^{-2}, which could lead to excessive latent heat fluxes (*Cullather and Bosilovich*, 2011). Indeed, in MERRA and most datasets, the closure problem is most acute in late spring, when evaporation is the highest. In contrast, the reanalyses diagnosing the most precipitation (NCEP CFSR and JRA 55) err in the opposite direction in the wet period of August and September.

We further divided the transports into the two so-called “Arctic seasons” : January-February-March-April (JFMA) and July-August-September-October (JASO) suggested by *Tilinina et al.* (2014) based on sea-ice concentrations. Figure 2.11 shows the longitudinal distribution of total moisture fluxes as well as the transient eddy part. The local maxima are well co-located in both seasons in the subpolar North Atlantic, the Labrador Sea and the Chukchi Sea. In these regions, the total summer fluxes are two to three times stronger compared to those in winter. This result also holds for the southward mean flow moisture flux over the Canadian Archipelago. The transient eddy fluxes in summer are also higher than in winter nearly everywhere, except for the Greenland Sea, where they are comparable. Likely, this results from the higher moisture in summer and the intensified storm activity over Northern Eurasia and the Eastern Arctic. *Serreze et al.* (2009) and *Tilinina et al.* (2013) demonstrated an intensification of cyclone activity over Northern Eurasia and Canada in summer that increases the advection of moistened air, leading to a doubling of the moisture transports over these regions.

2.5 Interannual variability

We also analysed how consistently the reanalyses reproduce the interannual variability of the Arctic moisture budget. The spread between reanalyses for the moisture transports is smaller than the interannual variability (Figure 2.12, a). As a result, the transport-based estimates of moisture convergence present common interannual variability patterns, such as a decade long decline starting in 1989. During this period, the total transports decreased statistically significantly by 12 (ERA Interim) to 15% (JRA 25). We computed linear trends

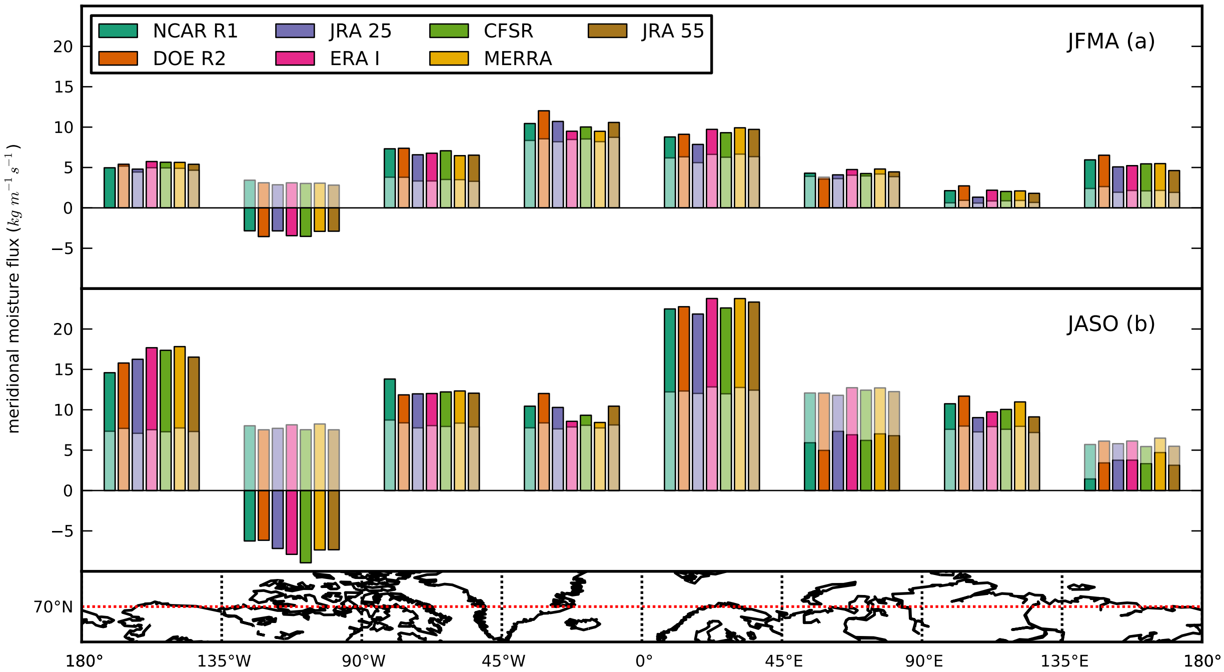

Figure 2.11: Same as Figure 2.7 but for the Arctic winter season (JFMA, panel a) and the Arctic summer season (JASO, panel b).

with different time windows to evaluate how robust these patterns were. Unlike MERRA (Figure 2.12, b), the significance of the trends in ERA Interim (panel c) is very sensitive to the starting year of the record : 1989 was a year of exceptionally strong fluxes. The impact of 1989 is evident in all reanalyses with the exception of MERRA. Over the 1979-2013 period, the trends in moisture transport are not statistically different from zero.

The Reynolds decomposition of the moisture flux gives some insight into the post-1989 decline. During this period, the transient eddy fluxes remained constant (Figure 2.13, a) but the contribution of stationary eddies and the polar cell dropped (panels b and c). The transport by the mean flow was responsible for the weakening of the meridional total moisture flux : by the turn of the millennium, transient eddies provided all of the moisture transport (panel d).

The time series of the moisture budget components confirm the disparity in evaporation and precipitation estimates as opposed to the transport products (Figure 2.13, e, f and g). Precipitation and evaporation are on the rise with the strongest signals identified in NCEP DOE R2 for evaporation (9.7% per decade) and in JRA55 for evaporation also (4.6% per decade). The reanalyses disagree as to the sign of the net precipitation change. Unlike the two JRA, most report an increase, with statistical significance in MERRA.

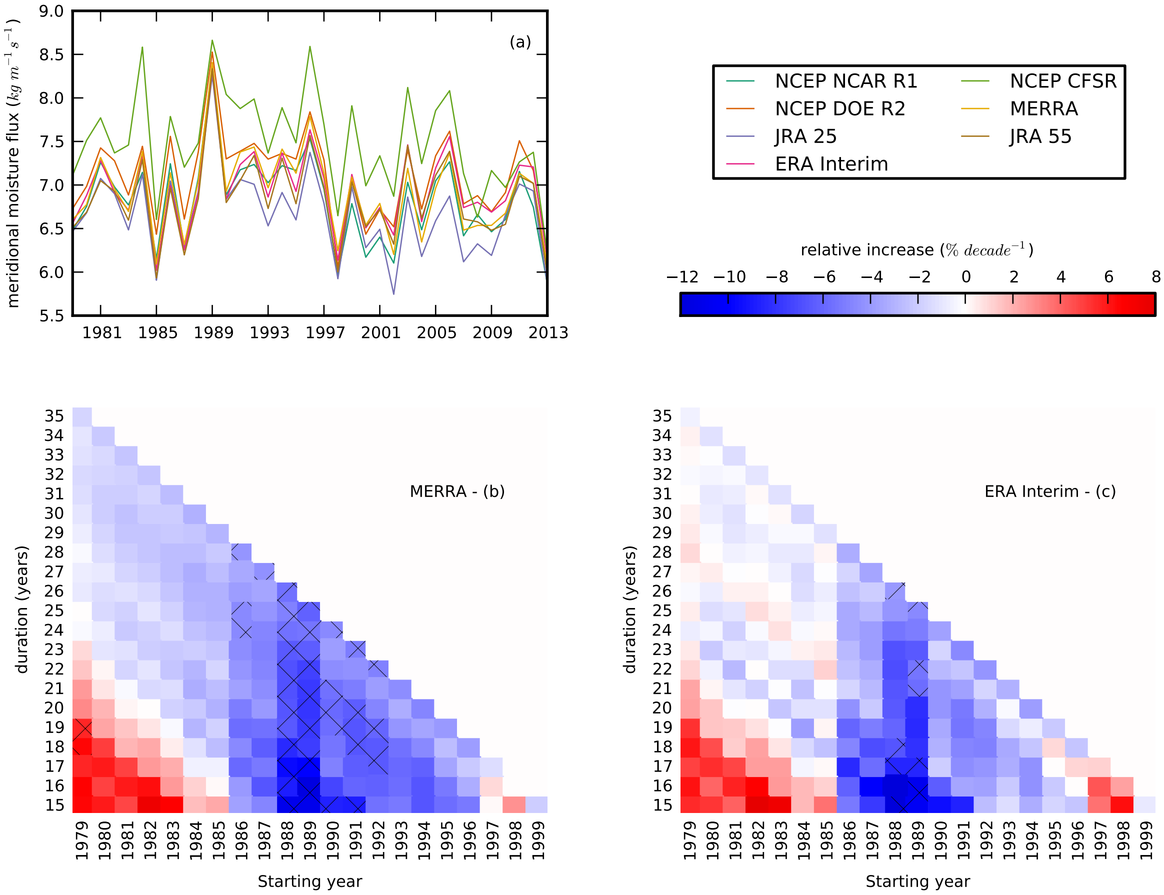

Figure 2.12: Time series of the mean meridional moisture flux through 70°N in all reanalyses (a). Slope of the linear trend for the said variable for MERRA (b) and ERA Interim (a) for different time windows. Statistical significance is denoted by hatches.

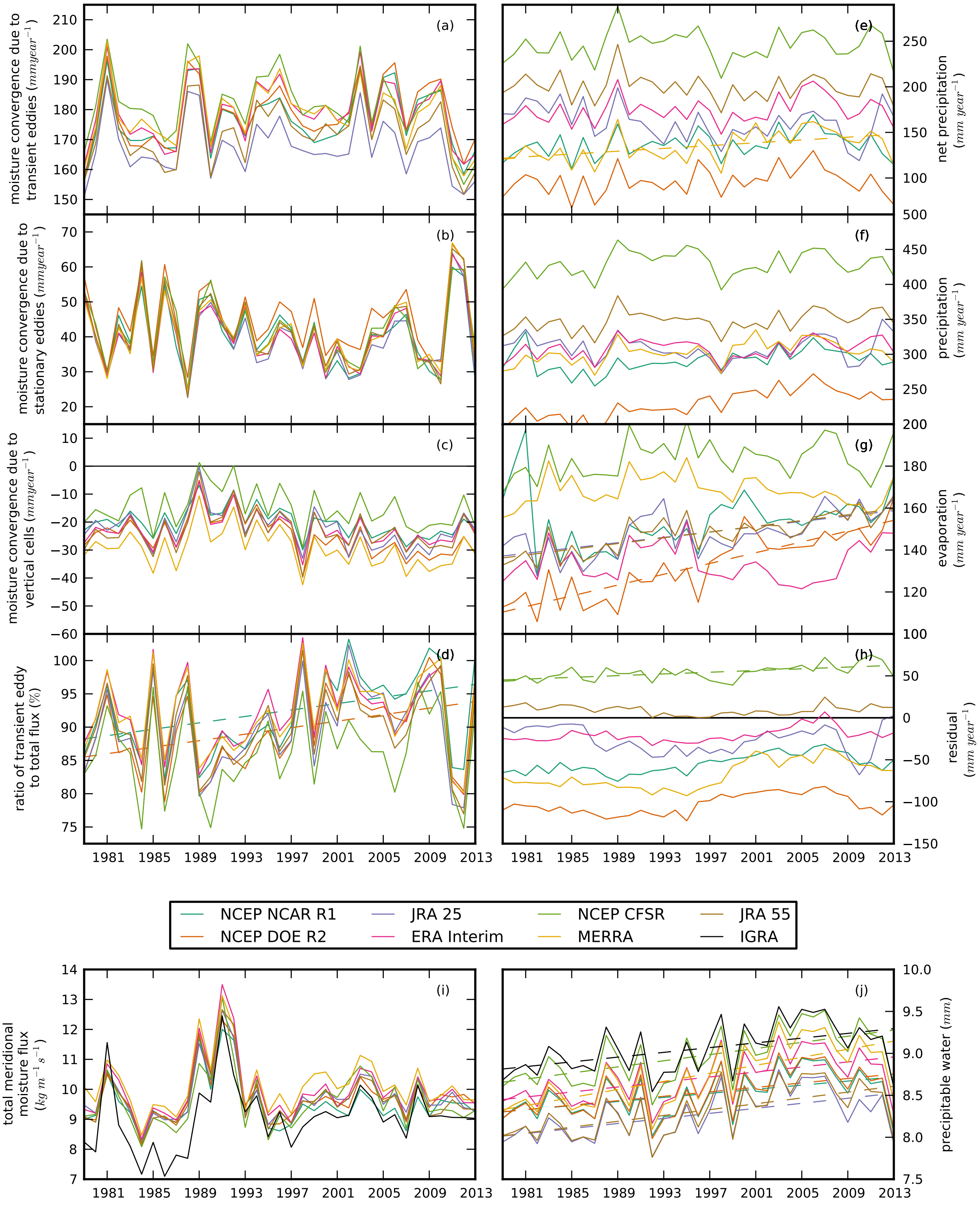

Figure 2.13: Time series of moisture convergence to the polar cap north of 70°N via the aerological method decomposed into the transient eddy part (a), the stationary eddy part (b) and the vertical cell (c) according to Equation 1.12. Panel (d) shows the transient eddy part divided by the total flux. Time series of the terms of the moisture budget for the said region : net precipitation or P-E via the physics output method (e), precipitation (f), evaporation (g) and the residual, i.e. the difference between the physics output and the aerological methods (h). Panel (i) on the lower left displays the meridional moisture flux in reanalyses and radiosondes averaged over all selected stations whereas panel (j) on the right does the same for the precipitable water variable. The regression line of the variable is drawn (in dashes) if its trend is statistically significant at the 95% level (Student t-test).

The non-closure of the moisture budget is accounted for in the residual term. The 1990s and early 2000 decade have seen a reduction in the absolute value of the residual in several datasets, most conspicuously in NCEP NCAR R1, JRA 25, ERA-Interim and MERRA. In the former, the sharp decrease (in absolute value) between 1998 and 1999 can be related to the introduction of the Advanced Microwave Sounding Unit (AMSU) in November 1998, as suggested by *Cullather and Bosilovich* (2011).

Figure 2.13 (i) and (j) show the comparison between reanalyses and IGRA data for meridional moisture fluxes and precipitable water, respectively. The radiosoundings indicate weaker moisture transport in the 1980s than the reanalyses but after 1989, the different transport estimates are highly consistent. Changes in precipitable water content are also very consistent across datasets, showing upward trends ranging from 5.0 to 9.8% over the 35-year period, with statistical significance at the 95% level.

A joint consideration of changes in the total meridional moisture transport and precipitable water reveals an apparent paradox. On the one hand, neither observations nor reanalyses report any significant change in northward moisture fluxes (Figure 2.13, i). On the other hand, precipitable water has increased unambiguously in all datasets (panel j). The increases in specific humidity have therefore not translated into corresponding increases in moisture fluxes. This goes against the widespread argument that the poleward moisture fluxes should strengthen in a warmer climate – it vindicates the opposing thesis, that the intensification of the hydrological cycle is driven locally by evaporation (*Bintanja and Selten*, 2014).

Given that moisture fluxes depend on both humidity and wind, a reasonable question comes : could changes in winds compensate the moistening ? To solve this conundrum, we introduce a more compact decomposition of the mean moisture fluxes through 70°N :

$$\{[\bar{qv}]\} = \{[\overline{q'^{*\circ} v'^{*\circ}}]\} + \{[\bar{q}]\}\{[\bar{v}]\} \tag{2.1}$$

where $q'^{*\circ} = q - \{[\bar{q}]\}$ and $v'^{*\circ} = v - \{[\bar{v}]\}$ i.e. anomalies relative to the vertical, zonal and monthly mean. The first term on the right-hand side is the covariance between the specific humidity and meridional wind. The second term is small as shown in Table 2.2 and we ignore it. We represent the covariance as the product of the standard deviation of the humidity and wind and their mutual correlation.

$$\{[\bar{qv}]\} = \sigma_{t,\lambda,p} q \ \sigma_{t,\lambda,p} v \ \mathrm{corr}_{t,\lambda,p}(q, v) \tag{2.2}$$

The evolution of the three factors over time is plotted in Figure 2.14.

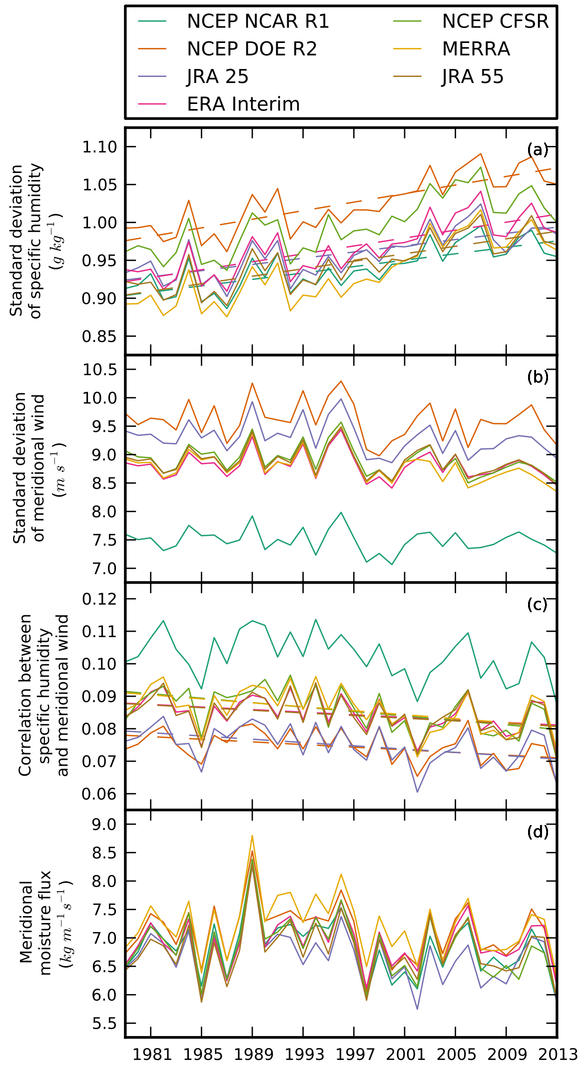

Figure 2.14: The covariance of meridional wind and specific humidity at 70°N decomposed into : the standard deviation of specific humidity (a), the standard deviation of meridional wind (b) and the correlation between both variables (c) according to Equation 2.2. Time series of the vertically integrated moisture flux through 70°N can be found in panel (d). Regression lines are drawn (in dashes) if the trends are statistically significant.

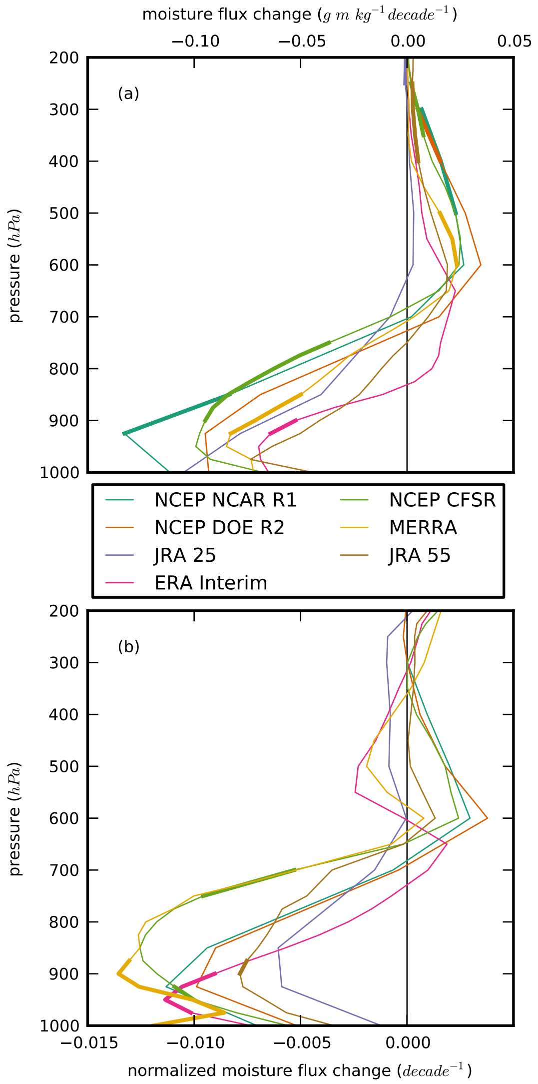

Figure 2.15: Vertical profile of the trend in meridional moisture flux at 70°N (a). Bold lines correspond to statistically significant trends. Vertical profile of the trend in normalized moisture flux (b). The normalized flux is defined as $[\bar{q}v]/(\sigma_{t,\lambda,p}q\ \sigma_{t,\lambda,p}v)$

The standard deviation of the humidity increased in all datasets from 7.5% (JRA 25) to 12.9% (MERRA), with statistical significance in NCEP NCAR R1, JRA 25, ERA Interim and JRA55 (Figure 2.14, a). The variance in humidity can be written as the sum of the temporal variance, the zonal variance and the vertical variance in much the same manner as the moisture flux in Equation 1.12.

$$\sigma^2_{t,\lambda,p} q = \{[\sigma^2_t q]\} + [\sigma^2_\lambda \bar{q}] + \sigma^2_p [\bar{q}] \tag{2.3}$$

The first term on the right-hand side, the temporal variability, only contributes slightly to the increase in the total variance (6-16%, depending on the reanalysis). The second and third terms represent the spatial variability, in both longitude and height. The saturation specific humidity depends exponentially on temperature through the Clausius-Clapeyron relation. If the atmosphere warms homogeneously and the relative humidity remains constant, the humid regions moisten faster than the dry regions. For example, the humidity contrast between the surface and the higher troposphere becomes sharper : $\sigma^2_p[\bar{q}]$ comprises 83–89% of the increase in the total variance. The contribution of the zonal variance is considerably smaller (-3–7%).

The standard deviation of the meridional wind stayed approximately stable, with a slight decrease in some reanalyses that was never statistically significant (Figure 2.14, b). The correlation between wind and humidity decreased significantly in all dataset but one (NCEP DOE R2) as shown in Figure 2.14 (c), which led to the slight decrease in the moisture flux (Figure 2.14, d) in spite of the moistening. The increasing humidity did not result in stronger moisture fluxes because the moisture and wind variations in space and time do not correspond as well as in previous periods.

Figure 2.15 (a) shows that the moisture flux has decreased below 700 hPa and increased moderately above. To explain this, we consider the correlation between meridional wind speed and humidity to determine which levels have contributed most to the $\mathrm{corr}_{t,\lambda,p}(q,v)$ statistic. We introduce a normalized flux : $[\overline{qv}]/(\sigma_{t,\lambda,p}q\ \sigma_{t,\lambda,p}v)$; its vertical integral is exactly $\mathrm{corr}_{t,\lambda,p}(q,v)$ according to Equation 2.3. The normalized flux has decreased particularly near the surface, between 950 and 850 hPa depending on the reanalysis (Figure 2.15, b). At these altitudes, the prevailing wind blows south, as part of the lower branch of the polar cell. However, this is only part of the explanation because the moisture transport due to the polar cell has not changed significantly (Figure 2.13, c).

The link between increases in moisture and transports is therefore not straightforward. The analysis of trends is impeded by strong interannual variability dominating the long-term tendencies. At the same time, climate models consistently project an increase in the moisture fluxes to the Arctic for the 21st century e.g. *Hwang et al.* (2011). The departure from the simple Clausius-Clapeyron scaling of the moisture fluxes could be a transitory phenomenon that would lapse when the global warming signal becomes stronger.

CHAPTER 3

Moisture advection to Antarctica

3.1 Spatial variability

In terms of observation density, a quick glance at Figures 1.4 and 1.5 shows that, of the two polar regions, the Antarctic is the poor relation. Ongoing long-term upper-air measurements are limited to the coast of East Antarctica and the South Pole station. Inland, the radiosonde program at Vostok Station stopped in 1992 ; at Dome C, winter-overs started in 2005 only. Polar orbiting satellites offer a good coverage of the continent but are handicapped by the resemblance between clouds and the frozen surface, the uncertainty in the snow emissivity estimates and the strong temperature inversions (*Bouchard et al.*, 2010). Consequently, we should expect a heavier reliance on the model first guess in the reanalyses and larger disagreements than in the Arctic even for analysed fields such as moisture and winds.

Over the Southern Ocean, the climatological moisture fluxes in ERA Interim (Figure 3.1, a) are dominated by the circumpolar westerlies with magnitudes in the order of 100 kg $m^{-1}s^{-1}$. The orographic precipitation over the Antarctic Peninsula leads to a depletion of moisture : the fluxes are halved on the leeward side. The polar vortex is centered on the Ross ice shelf (150°W-160°E) rather than on the South Pole, as explained in *King and Turner* (2007). The asymmetry in the prevailing winds causes significant advection to West Antarctica. Surprisingly, the fluxes do not immediately decrease as they move inland, despite the ice sheet's mean altitude of 850 m (Figure 3.1, b).

The moisture flux to East Antarctica is controlled by the circumpolar trough, a feature also described in *King and Turner* (2007). This belt of low pressure and high cyclone activity is located at an average latitude of 66°S with variations according to seasons. The mean winds inferred from Buys Ballot's law change from westerlies on the equatorward side of the trough, to easterlies on the poleward side. The change of direction causes some advection inland depending on the configuration of the coast. The trough off the coast of East Antarctica is actually subdivided into two low pressure regions, one at 20°E, the other at 90°E. Each is the center of a cyclonic circulation whose eastern branch works to advect moisture southward.

The reanalyses disagree on the magnitude of the fluxes due to the circumpolar westerlies

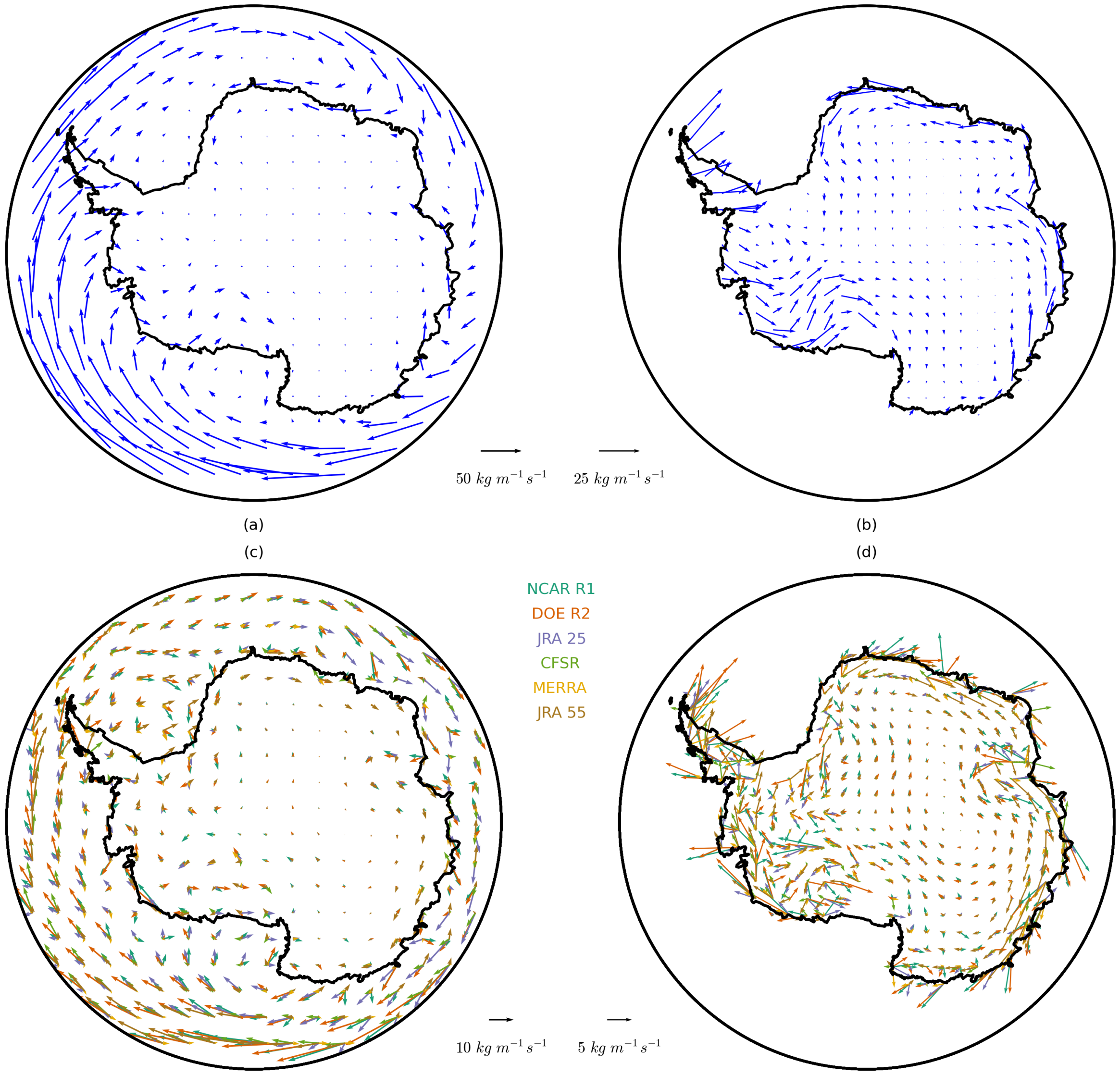

Figure 3.1: Mean vertically integrated moisture flux south of 60°S in ERA-Interim (a) and, with twice the arrow scale, a zoom on just the ice sheet (b). Panel (c) shows the differences in vertically integrated moisture flux between the other 6 reanalyses and ERA-Interim, idem for panel (d) with twice the scale on just the ice sheet.

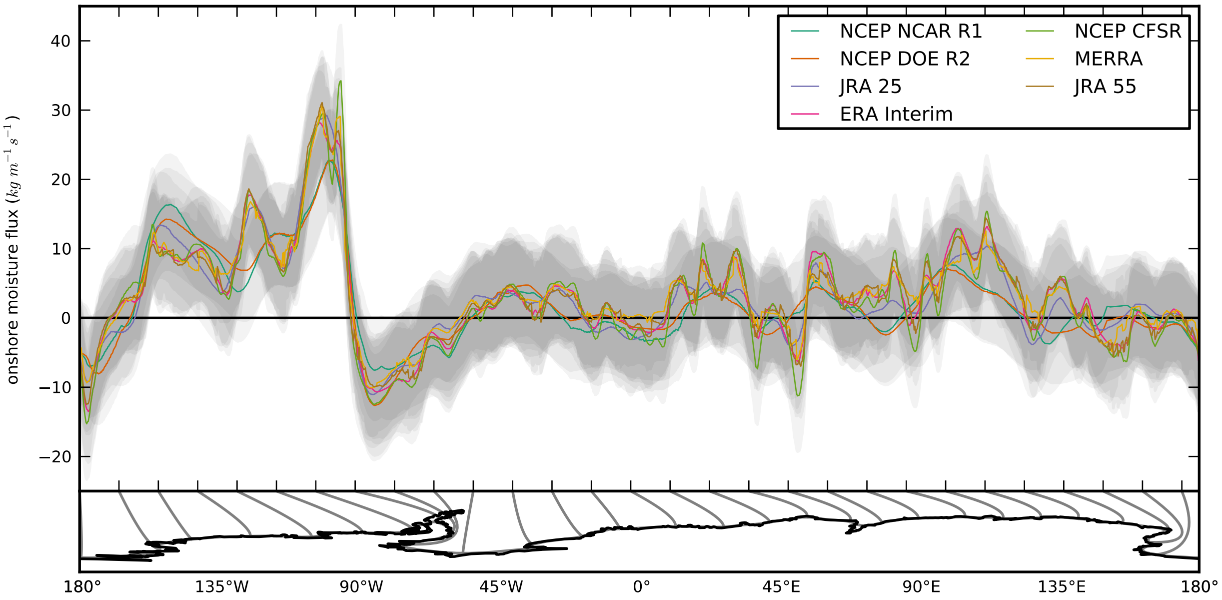

Figure 3.2: Distribution of the mean meridional vertically integrated moisture flux on the boundary of the Antarctic ice sheet in different reanalyses. The grey shaded bands indicate the ranges corresponding to plus or minus one interannual standard deviation from the mean.

(Figure 3.1, c). Over the subpolar Pacific Ocean, ERA Interim estimates weaker fluxes. Over the subpolar Atlantic and Indian Oceans, the disagreement is limited to the older reanalyses, NCEP NCAR R1, NCEP DOE R2 and JRA 25. Inland, these three datasets continue to stand out (Figure 3.1, d), particularly on the coast with sometimes 180° differences in direction with ERA Interim. The widespread inconsistency over West Antarctica concerns all reanalyses.

The coastal profile in the upper panel of Figure 3.2 was built by interpolating the mean moisture flux field on the smoothed boundary of the Antarctic ice sheet (lower panel). The maximum onshore fluxes are located on the westward (windward) side of the Antarctic Peninsula but are partly cancelled out by the outgoing fluxes on the eastward (leeward) side. West Antarctica sees weaker but consistently positive fluxes ($\sim$ 10 kg $m^{-1}s^{-1}$). Overall, the moisture transports are positive over East Antarctica with occasional negative values in valleys where the katabatic winds are channelled, e.g. on the Amery ice shelf (70°E). NCEP DOE R1, NCEP DOE R2 and to a lesser extent JRA 25 are oblivious to these local effects. On the other hand, NCEP CFSR, whose spectral resolution is the highest (T382), shows stronger offshore fluxes at these locations than ERA Interim, MERRA and JRA 55.

The inter-dataset spread of the southward moisture flux is variable depending on the coastal radiosonde sites (Figure 3.3) : small for homogeneous coastal conditions, but large near valleys acting like funnels for the wind. Syowa Station (69°S, 39°E) and Davis Station (68°S, 77°E) are both located near glacier outlets (Shirase and Lambert Glaciers, respectively) nested in such valleys. CFSR is paradoxical : it is either the closest to the radiosonde observations, or the furthest (at Halley Station, 75°S, 26°W and McMurdo Station, 77°S, 166°E). Compared with the Arctic, the reanalyses are still highly correlated with the observations although the coefficients are more spread out : from 0.75 to practically 1. CFSR is still the closest to the radiosondes, followed closely by ERA Interim. Our most recent dataset, JRA 55, often performs the worst.

Just like in the Arctic, the observed precipitable water content is higher than in the reanalyses (Figure 3.3, b). Given the low amounts, the range between the most dry and the most humid dataset amounts to approximately one fourth of the mean value. The dispersion of southward wind speeds at 850 hPa is even greater. The coarser the grid, the more the reanalysis is biased towards offshore northward winds. We suggest that the stations are not representative of their surroundings, because they were generally built in places sheltered from the winds. Only the high resolution datasets can represent both the katabatic outflow and the relative haven of the station. Unlike the Arctic, the direction of the wind at 850 hPa corresponds to the direction of the moisture fluxes : the mean flow flux may be comparable in magnitude to the transient eddies.

The vertically integrated moisture flux is the product of two competing phenomena according to the vertical profiles in Figure 3.4. Near the surface, moisture is exported to the north but higher up, it is imported south. CFSR and JRA 55 reproduce the observed height where the fluxes change sign, at 950 hPa. The two first NCEP reanalyses see it at 750 hPa, JRA 25 at 850 hPa. As a consequence, they overestimate the near-surface northward fluxes and underestimate the upper-air southward fluxes. Specific humidity is not quite as consistent between reanalyses and observations than in the Arctic. The datasets diverge at the surface. As observed, there is a humidity inversion in MERRA and JRA55, but it is too deep and too strong. Conversely, the three NCEP reanalyses (R1, R2, CFSR) are all too moist. Figure 3.4 panel (c) shows the characteristic profile of katabatic winds. The height of the katabatic layer is systematically too high in reanalyses : the lower the model resolution, the higher it is. The mean winds are always blowing north : they cannot account for the southward moisture fluxes observed in panel (a), which are presumably due to transient eddies. The vertical correlation patterns are the same as in the Arctic but the coefficients are approximately 0.1 lower. NCEP NCAR R1, NCEP DOE R2, MERRA and the two JRA

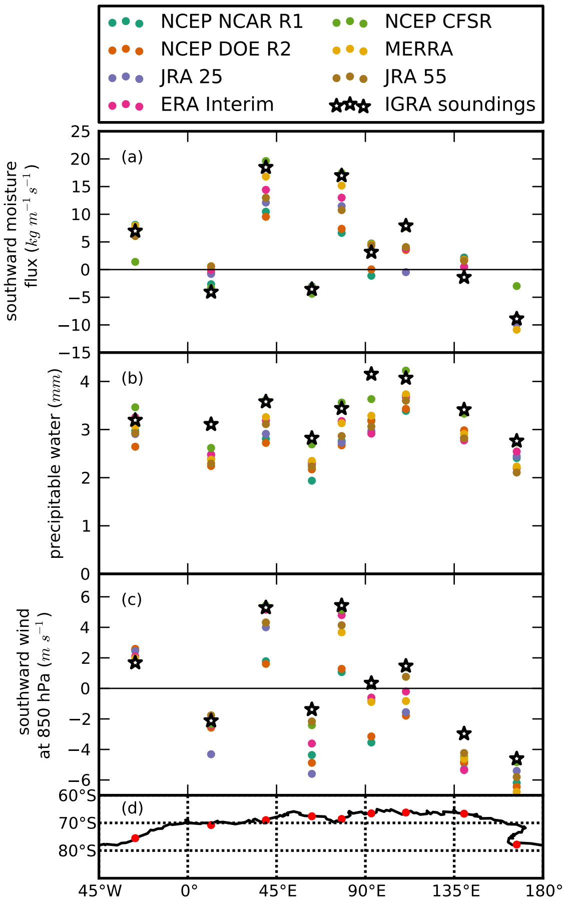

Figure 3.3: Estimates of the vertically integrated meridional moisture flux derived from reanalyses and radiosoundings at the location of the coastal radiosonde stations (a), idem for precipitable water (b) and for the meridional wind at 850 hPa (c). Panel (d) gives the location of the radiosonde stations

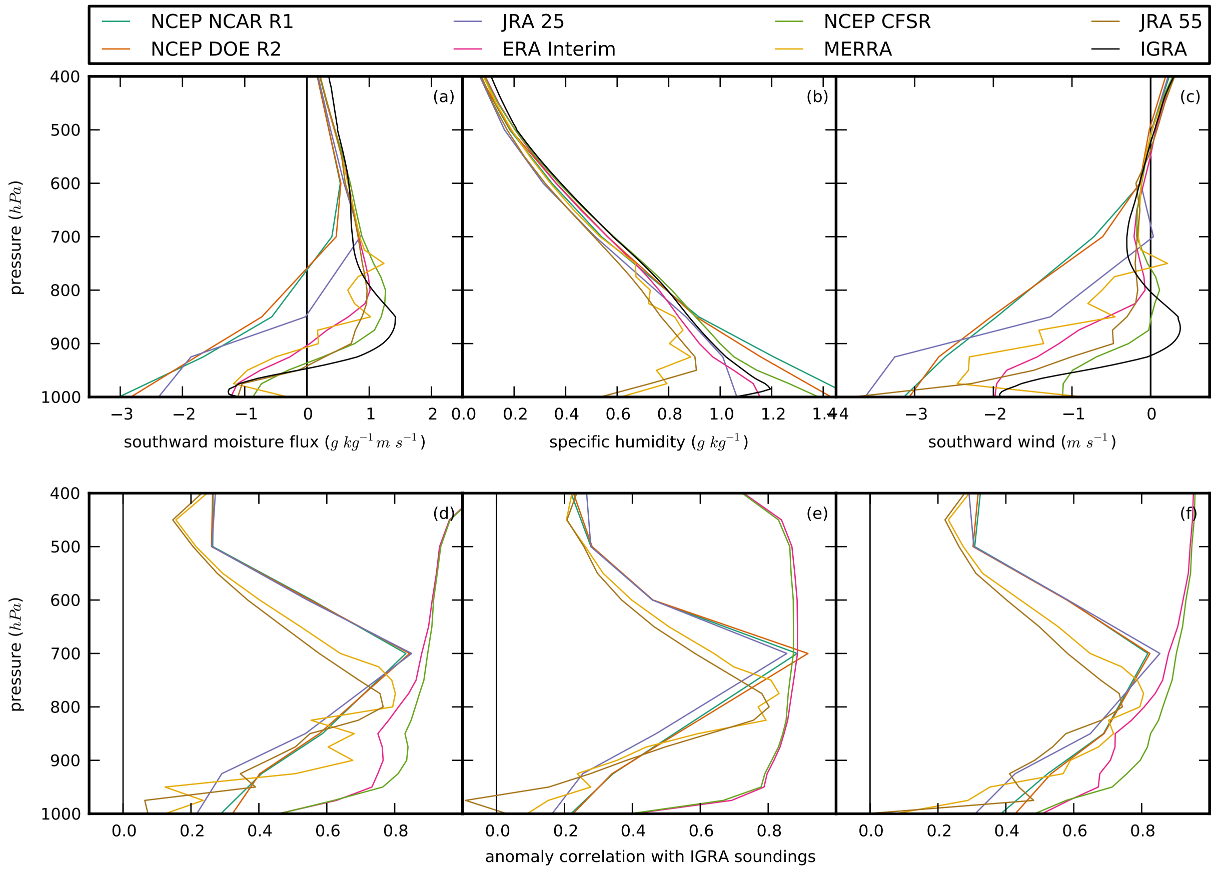

Figure 3.4: Time-averaged (1979-2013) vertical profiles of the seven reanalyses co-located with the coastal radiosonde sites and averaged over all these sites for the meridional moisture flux (a), specific humidity (b) and meridional wind. The lower panels show the correlations between the said variables in reanalyses and in the radiosoundings.

reach a maximum of correlation at a lower altitude than in the Arctic, by 100 hPa.

Conventional snow gauges cannot discriminate between precipitation and blowing snow, a frequent phenomenon on the coast, nor can they measure the tenuous snowfall in the interior of the continent (*Bromwich et al.*, 2011). The accumulation datasets of *Arthern et al.* (2006) and *Favier et al.* (2013) rely mainly on stake measurements, on the identification of reference horizons in ice cores, and, in the case of *Arthern et al.* (2006), on satellite microwave observations to interpolate between in situ measurements. From August 2006 to April 2011, CloudSat offered direct measurements of Antarctic precipitation. The spaceborne radar measured the reflectivity of clouds and precipitating particles and was able to detect the occurrence and rate of snowfall (*Palerme et al.*, 2014). We reproduce the CloudSat and ERA Interim snowfall estimates (Figure 3.5, a and b). The footprint of CloudSat is relatively narrow and its orbit never goes further south than 82°S. As a result, there is no data for higher latitudes. We followed the same conventions to plot ERA Interim's convergence of atmospheric water product (all three phases) in panel (c).

Tsukernik and Lynch (2013) suggested to use moisture convergence over Antarctica as a proxy for accumulation. Moisture fluxes are observed more reliably outside the domain whereas net precipitation is computed by the model using different and potentially inappropriate parameterisations. The convergence product has one drawback : even in spectral space and on model levels, its computation generates numerical artefacts. In East Antarctica, some spatial patterns are suspiciously aligned along meridians (this would not affect continent-wide averages). Unlike snowfall, the convergence can sometimes be negative : net sublimation occurs in the vicinity of the McMurdo Dry Valleys (77°S, 162°E), on the Lambert Glacier and on the plateau, even if the former may be artefacts. The strong convergence over the Antarctic Peninsula is shifted towards the West compared with the satellite snowfall. ERA Interim's snowfall is everywhere below 1500 mm per year whereas the convergence may be greater than 2000 mm per year. The difference is due to liquid precipitation and the analysis increment.

3.2 Long-term moisture budgets

With fewer observations to constrain the analysed fields, we cannot expect to find a similar agreement between datasets in the Antarctic as in the Arctic. On the other hand, the analysis increment should be reduced due to the smaller amount of new information to accomodate. This is indeed what the figures in Table 3.1 suggest. Unlike the Arctic, precipitation is generally higher than evaporation plus advection, but only by 25% in the worst case (JRA 25 over the Antarctic Plateau). This can be be seen in Figure 3.6 by comparing the left and right bar of each reanalysis. The evaporation in NCEP NCAR R1 is unrealistically large (*Hines et al.*, 1999) and still excessive in NCEP DOE R2 (*Bromwich et al.*, 2011). In the latest reanalyses, it is barely positive, with net sublimation in JRA 55.

The 60°S latitude circle covers only ocean ; the Antarctic Plateau covers only land. The 70°S parallel briefly crosses the Antarctic Peninsula and intersects large swaths of East Antarctica so it could count as "piecewise homogeneous" terrain. On the boundaries of the ice sheet however, the moisture fluxes experience substantial changes of magnitude and direction over short distances. This translates in the ratio of the inter-dataset standard deviation to the inter-dataset mean : 4 % at 60°S, 3% at 70°S, 11% for the ice sheet and 7%

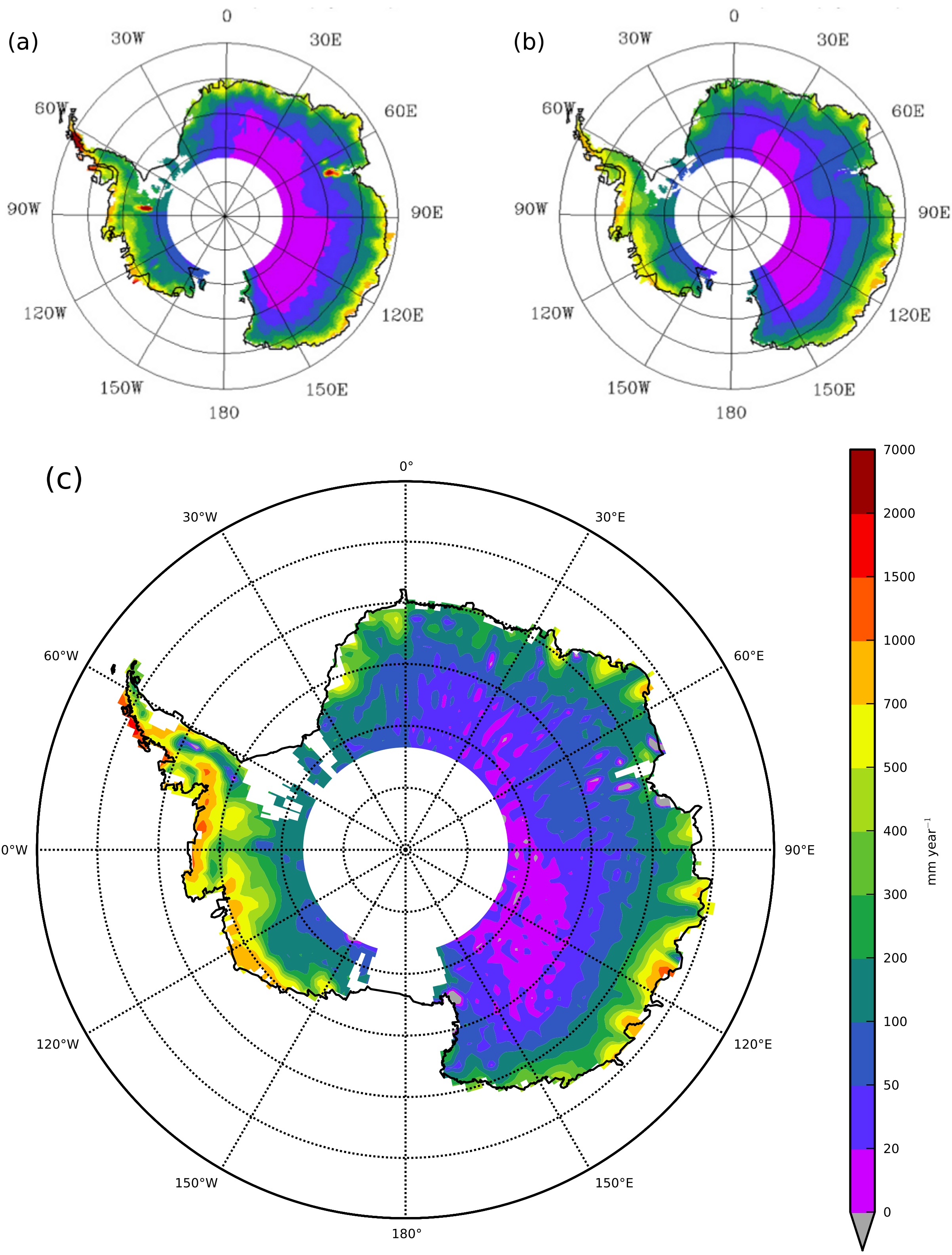

Figure 3.5: Mean snowfall rate from August 2006 to April 2011 according to CloudSat (a) and ERA Interim (b). These two panels are reproduced from *Palerme et al.* (2014). Mean convergence of atmospheric water –vapour and condensate – in ERA Interim, for the same time window and colour scale (c).

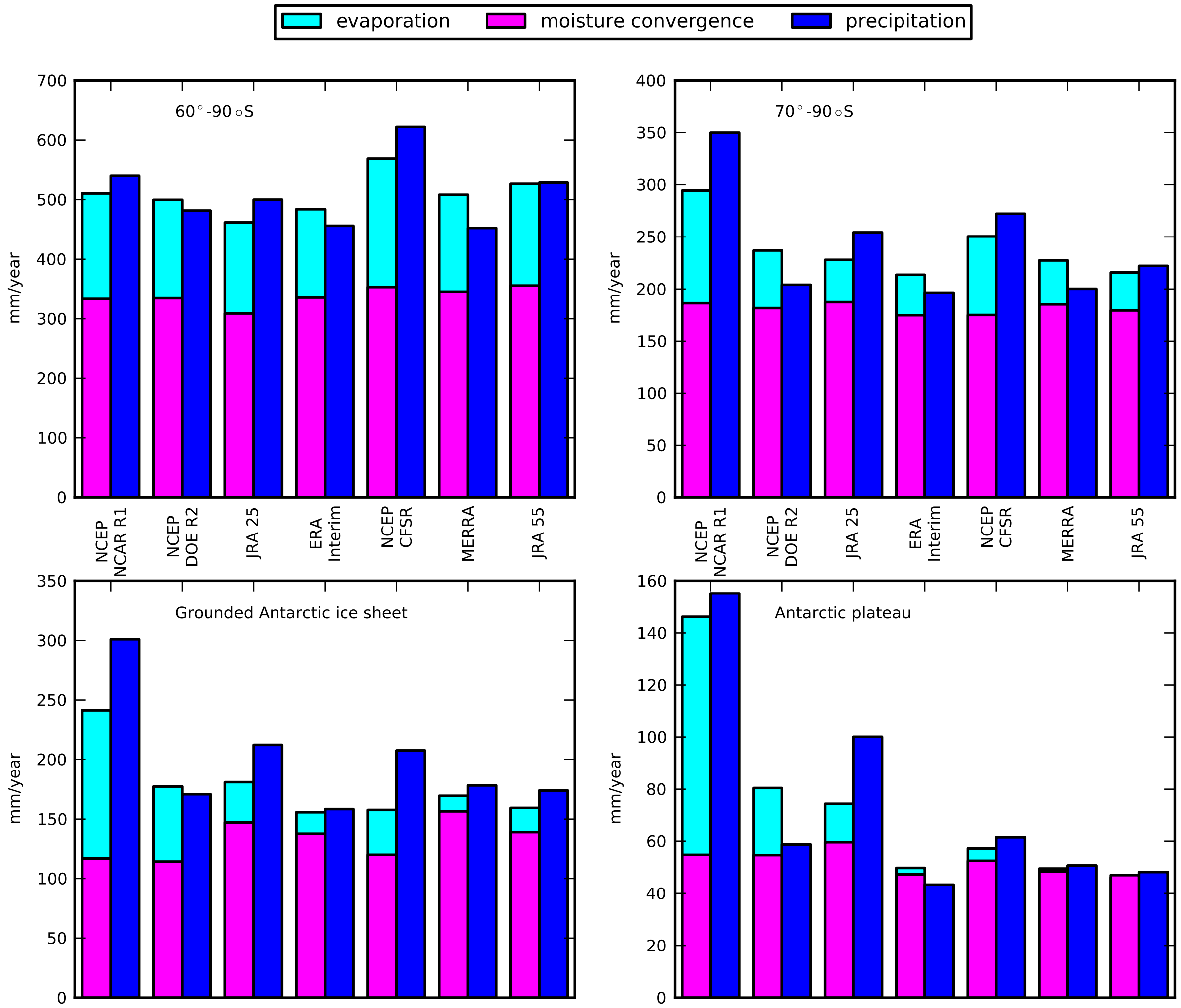

Figure 3.6: Histogram of the long-term averaged (1979-2013) moisture budget terms (mm year^{-1}) for the polar caps south of 60°S, 70°S and the Antarctic ice sheet and plateau.

for the plateau despite its radical climate.

CloudSat does not reach latitudes south of 82°S, which justified a separate table, adapted from *Palerme et al.* (2014). The different variables are close to one another over the whole ice sheet. The difference between net precipitation and atmospheric water convergence is of the same order of magnitude as the liquid precipitation ($\sim$ 10 mm year^{-1}).

3.3 Role of the mean flow and transient eddies

From Figure 3.7 (a), the mean flow fluxes correspond to the circumpolar westerlies. Their magnitude weakens at longitude 0° and 90°E, possibly in relation to the two low pressure centers that modulate the circumpolar trough. As reported earlier, the polar vortex is

Region	Source	Period	P	E	P-E	T	P-E-T
60°-90°S	*Bengtsson et al.* (2011)	1989-2009	495	151	344	332	13
	NCEP NCAR R1	1979-2013	541 (30)	177 (5)	363 (30)	333 (26)	30 (8)
	NCEP DOE R2	1979-2013	482 (35)	165 (6)	316 (32)	335 (27)	-18 (9)
	JRA 25	1979-2013	500 (17)	153 (5)	347 (14)	309 (15)	38 (15)
	ERA Interim	1979-2013	456 (11)	148 (6)	308 (11)	336 (11)	-28 (5)
	NCEP CFSR	1979-2013	622 (16)	216 (20)	406 (22)	353 (13)	53 (15)
	MERRA	1979-2013	453 (41)	163 (8)	290 (45)	346 (18)	-56 (33)
	JRA 55	1979-2013	528 (15)	171 (4)	358 (14)	356 (12)	2 (4)
70°-90°S	*Genthon and Krinner* (1998)	1979-1993				162	
	Cullather and Bosilovich (2011)	1979-2005	198 (14)	43 (2)	155 (13)	188 (11)	-33
	NCEP NCAR R1	1979-2013	350 (19)	108 (4)	242 (16)	186 (16)	56 (4)
	NCEP DOE R2	1979-2013	204 (19)	55 (6)	149 (16)	182 (14)	-33 (6)
	JRA 25	1979-2013	254 (10)	41 (2)	214 (9)	187 (8)	26 (5)
	ERA Interim	1979-2013	196 (8)	39 (2)	158 (7)	175 (7)	-17 (2)
	NCEP CFSR	1979-2013	272 (12)	75 (10)	197 (11)	175 (9)	22 (6)
	MERRA	1979-2013	200 (13)	42 (2)	158 (13)	185 (10)	-27 (8)
	JRA 55	1979-2013	222 (10)	36 (2)	186 (9)	179 (9)	6 (2)
Antarctic Ice Sheet	*Monaghan et al.* (2006)	1985-2001	200		180 (8)		
	Arthern et al. (2006)	Long term				143 (4)	
	Van de Berg et al. (2006)	1980-2004				171 (3)	
	Cullather and Bosilovich (2011)	1979-2005	165 (10)	11 (1)	154 (11)	171 (11)	17
	NCEP NCAR R1	1979-2013	301 (15)	125 (6)	176 (12)	117 (10)	59 (5)
	NCEP DOE R2	1979-2013	171 (15)	63 (7)	108 (10)	114 (10)	-7 (6)
	JRA 25	1979-2013	212 (12)	34 (2)	178 (11)	147 (8)	31 (6)
	ERA Interim	1979-2013	158 (7)	18 (1)	140 (8)	137 (7)	3 (2)
	NCEP CFSR	1979-2013	207 (11)	38 (2)	170 (11)	120 (9)	50 (5)
	MERRA	1979-2013	178 (11)	13 (1)	165 (11)	156 (10)	9 (5)
	JRA 55	1979-2013	174 (11)	21 (2)	153 (10)	139 (9)	14 (1)
Antarctic Plateau	NCEP NCAR R1	1979-2013	155 (9)	91 (4)	64 (7)	55 (9)	9 (5)
	NCEP DOE R2	1979-2013	59 (8)	26 (4)	33 (6)	55 (10)	-22 (7)
	JRA 25	1979-2013	100 (7)	15 (1)	85 (7)	60 (6)	26 (6)
	ERA Interim	1979-2013	43 (4)	3 (0)	41 (4)	54 (4)	-13 (1)
	NCEP CFSR	1979-2013	61 (6)	5 (1)	57 (6)	52 (4)	4 (2)
	MERRA	1979-2013	51 (5)	1 (0)	50 (5)	55 (4)	-6 (1)
	JRA 55	1979-2013	48 (6)	-1 (0)	49 (6)	47 (5)	2 (1)

Table 3.1: Long-term averaged (1979-2013) moisture budget terms (mm year^{-1}) for the polar caps south of 60°S, 70°S, and the Antarctic ice sheet and plateau ; T refers to the total poleward moisture transport, P to precipitation and E to evaporation. Values in brackets are the interannual standard deviations. This table is adapted from *Cullather and Bosilovich* (2011).

variable	source	ice sheet	altitude >2250 m	altitude <2250 m
snow accumulation	*Arthern et al.* (2006)	163	81	243
snowfall	*Palerme et al.* (2014)	171	36	303
snowfall	ERA Interim	163	49	273
precipitation	ERA Interim	178	50	305
net precipitation	ERA Interim	154	46	260
water convergence	ERA Interim	166	60	271

Table 3.2: Climatologies of snow accumulation, snowfall, precipitation and water convergence over domains excluding the cap south of 82°S (mm year^{-1}). Apart from *Arthern et al.* (2006), the climatologies start in August 2006 and end in April 2011.

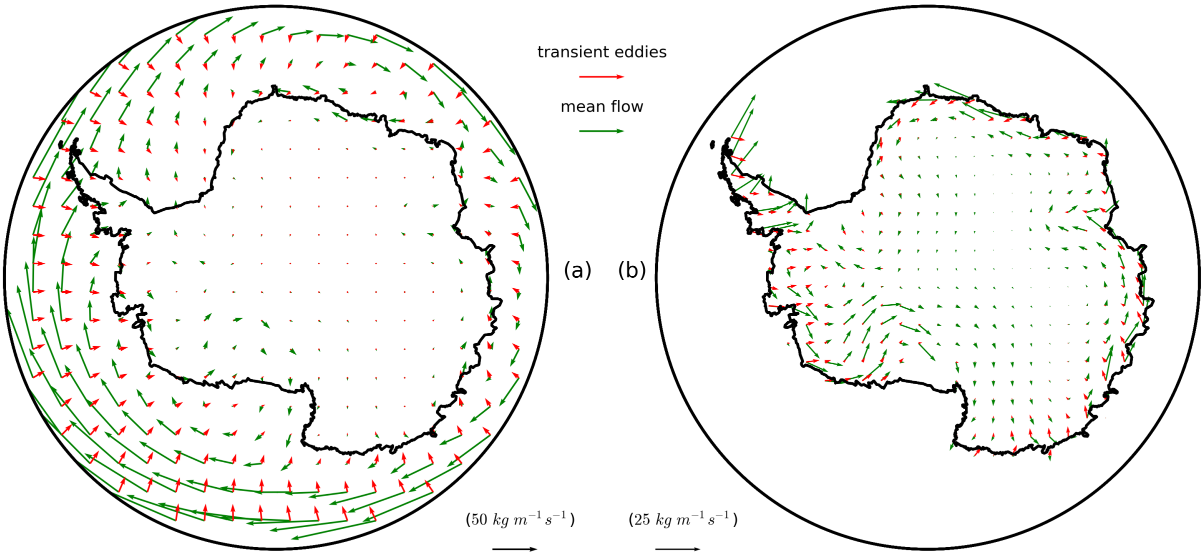

Figure 3.7: Reynolds decomposition (Equation 1.11) of the moisture fluxes in ERA-Interim : south of 60°S (a) and with twice the arrow scale, just on the Antarctic ice sheet (b).

centered on the Ross ice shelf and interrupted by the East Antarctic ice sheet. The transient eddy fluxes make a right angle with the mean circumpolar winds and are approximately five times weaker in magnitude (~ 10 kg $\mathrm{m}^{-1}\mathrm{s}^{-1}$ compared with ~ 50 kg $\mathrm{m}^{-1}\mathrm{s}^{-1}$).

Both the mean flow due to the polar vortex and the transient eddy fluxes penetrate deep inside West Antarctica. In East Antarctica, the mean flow flux is orientated west, slightly away from the coast. We interpret it as the influence of the circumpolar trough and the deflection of katabatic winds by the Coriolis force. The transient eddy fluxes blow inland with a similar eastward component. In Adélie Land (140°E), the mean flow and transient eddies work in nearly opposite directions.

Most of the onshore flux is due to the transient eddy part (transparent bars in 3.8). In the first sector (eastern part of the Ross ice shelf and West Antarctica), roughly two thirds are caused by transient eddies, the lowest proportion of all sectors. The westerlies over the Peninsula are not particularly divergent and in the remaining domains, the mean flow tends to advect moisture away from the ice sheet. In Wilkes Land (second to last sector), the modern reanalyses show weak onshore mean flow fluxes, of varying magnitude. The inconsistency between reanalyses is caused by the mean flow rather than transient eddies.

We decompose the mean flow term into stationary eddies, vertical cells and a residual,

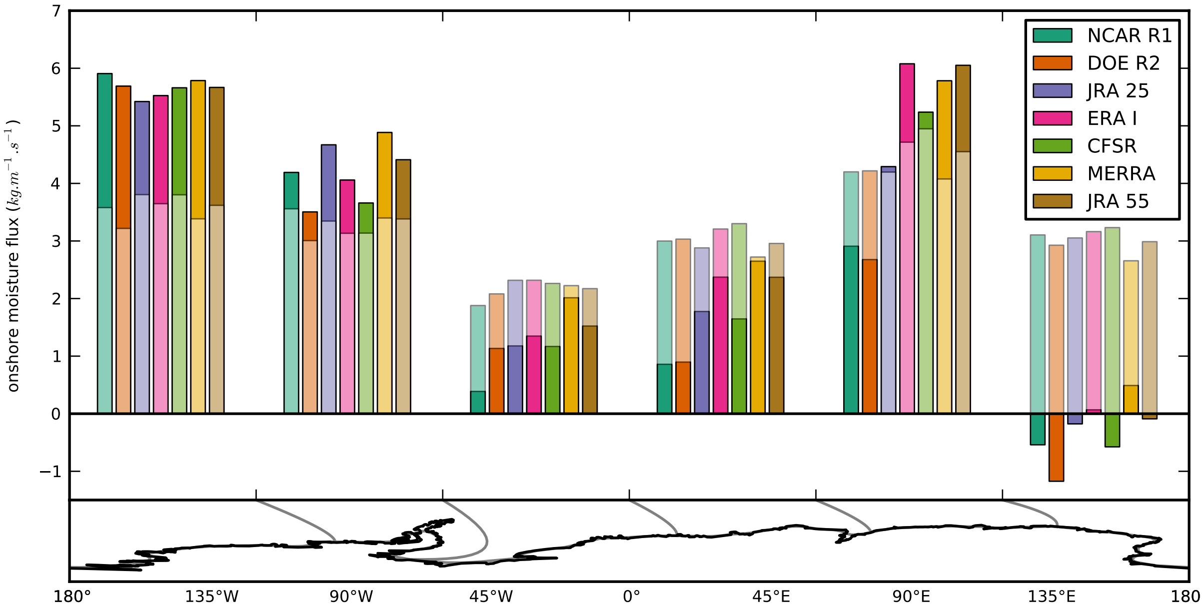

Figure 3.8: Distribution of the vertically integrated total moisture transport along the boundary of the Antarctic ice sheet and its transient eddy component (from Equation 1.11, semi-transparent bars ; all bars start at zero) in the seven reanalyses (1979-2013). Each set of bars correspond to the average over 45-degree longitudinal bands, defined in the map in the lower panel.

according to Equation 1.12. The result on latitude circles is displayed in Figure 3.9 (a) and is similar to the profile found in *Tsukernik and Lynch* (2013). Given their preferred meridional orientation, transient eddies are responsible for most of the southward moisture flux : around 90% at 70°S (Figure 3.9, b). The stationary eddies are considerably weaker, despite the moisture contrasts along the latitude circles intersecting the coast (mostly between 65 and 80°S). The polar cell is of comparable magnitude : it advects moisture away from the pole south of 65°S.

Figure 3.9, (c) shows data interpolated along the smoothed boundary of the ice sheet. In this particular case, the Reynolds decomposition was performed after the interpolation. The zonal mean $[\cdot]$ is replaced with the average along the boundary. Unsurprisingly, the transient eddies blow moisture inland at all altitudes, with a maximum around 750 hPa. We interpret the stationary eddy and the vertical cell profiles as the effect of katabatic winds. Some locations on the coast at the mouth of valleys drain more dry, inland air than the rest, which implies anomalous mean humidities $\bar{q}^*$ and offshore winds $\bar{v}^*$, in other words, stationary eddies. The katabatic winds occur near the surface so they show up as vertical anomalies too : both $[\bar{q}]^\circ$ and $[\bar{v}]^\circ$, i.e. the polar cell. As we saw over the radiosonde sites, the katabatic layer is deeper in the old reanalyses. The lower branch of the vertical cell is weaker

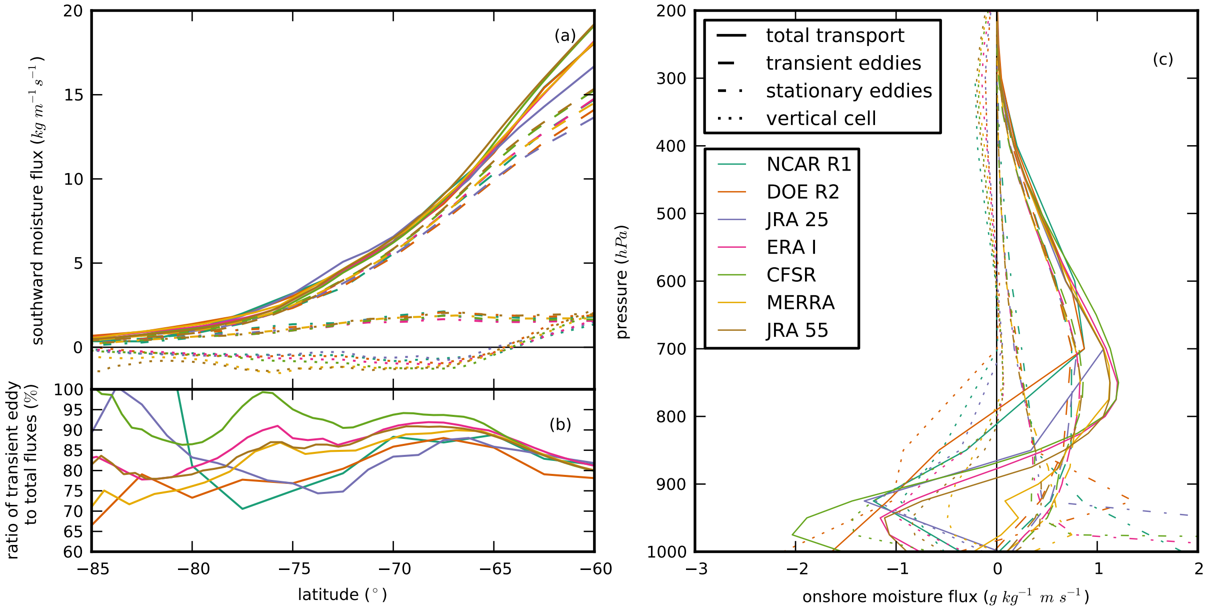

Figure 3.9: Meridional distribution in absolute (a) and relative values (b) of the different terms of the Reynolds decomposition (Equation 1.12) of the southward moisture flux and their vertical profiles along the coast of the Antarctic ice sheet (c).

in MERRA but we believe this is an artefact. The underground pressure levels are already masked in the MERRA archives, more conservatively than by our own procedure : part of the katabatic layer is masked. The vertical cell imports very dry air from the mid-latitudes higher than 500 hPa, actually higher still than our last level, 200 hPa. We accounted for the subsequent subsidence in our mass budget calculations.

Table 3.3 summarises the contribution of each flux component to the moisture convergence over the Antarctic ice sheet. The figures must be taken with a grain of salt : the domain boundaries have been smoothed and we performed the interpolation before computing averages and anomalies.

3.4 Seasonal variability

The seasonal cycle of moisture convergence and net precipitation is not as pronounced as in the Arctic because the precipitable water content does not vary as much (*Oshima and Yamazaki*, 2006). Instead, the winter maximum is due to the stronger cyclone activity despite the low humidity. This pattern is reproduced by all the reanalyses (Figure 3.10). The convergence is highest in March ($\sim$ 15 mm month^{-1} in the modern datasets) and then settles on a plateau throughout autumn and winter. Spring sees a short-lived drop in

Reanalysis	total $\{[\bar{q}\bar{v}]\}$	transient eddies $\{[\overline{q'v'}]\}$	stationary eddies $\{[\bar{q}^*\bar{v}^*]\}$	vertical cell $\{[\bar{q}]^\circ[\bar{v}]^\circ\}$	residual $\{[\bar{q}]\}\{[\overline{v_{nd}}]\}$
NCEP NCAR R1	141 (14)	199 (17)	72 (10)	-107 (13)	-22.6 (0.0)
NCEP DOE R2	131 (16)	190 (17)	60 (9)	-106 (12)	-13.4 (0.0)
JRA 25	176 (13)	201 (11)	64 (10)	-84 (7)	-4.6 (0.0)
ERA Interim	200 (11)	207 (11)	65 (7)	-73 (5)	0.5 (0.0)
NCEP CFSR	173 (15)	213 (12)	67 (7)	-105 (7)	-1.6 (0.0)
MERRA	218 (14)	184 (10)	62 (8)	-86 (8)	-0.3 (0.0)
JRA 55	215 (14)	199 (14)	69 (7)	-114 (9)	-4.2 (0.0)

Table 3.3: Long-term averaged (1979-2013) components of the moisture convergence on the Antarctic ice sheet (mm year^{-1}) according to Equation 1.12. $\{[\overline{v_{nd}}]\}$ is the residual of Equation 1.16. Values in brackets are the interannual standard deviations.

convergence, caused mainly by increased evaporation and decreased mean flow fluxes. There is no appreciable precipitable water tendency, at least not of similar magnitude as the other terms of the moisture budget.

The radiosondes sites only sample a small part of the domain boundary. The cycle of moisture advection averaged over the stations has little in common with the cycle for the whole ice sheet (Figure 3.11). Instead of a plateau, the late autumn and winter seasons are interrupted by weaker months, in May and September. The precipitable water content follows the expected cycle : a sharp maximum in January (3 mm in observations) and dry values (below 1.5 mm) for the whole winter. The interior of the continent is even drier : this is why there was no visible annual variation in water content in Figure 3.10.

The spatial distribution of moisture fluxes shows no consistent behaviour among sectors between summer and winter (Figure 3.12). Over West Antarctica, the dramatic winter increase was mainly due to the mean flow, whereas it decreased over the Peninsula. East Antarctica remains quite unchanged except in Wilkes Land, which sees an approximate 50% increase of both the mean flow and transient eddy components.

3.5 Interannual variability

The interannual variability of precipitation in Antarctica has been treated extensively in *Bromwich et al.* (2011) and *Nicolas and Bromwich* (2011). The former article has a telling title “Precipitation Changes in High Southern Latitudes from Global Reanalyses: A Cautionary Tale” : the trends were largely spurious according to the authors. Even the modern reanalyses were affected by artefacts : MERRA (and CFSR to a lesser extent) by the in-

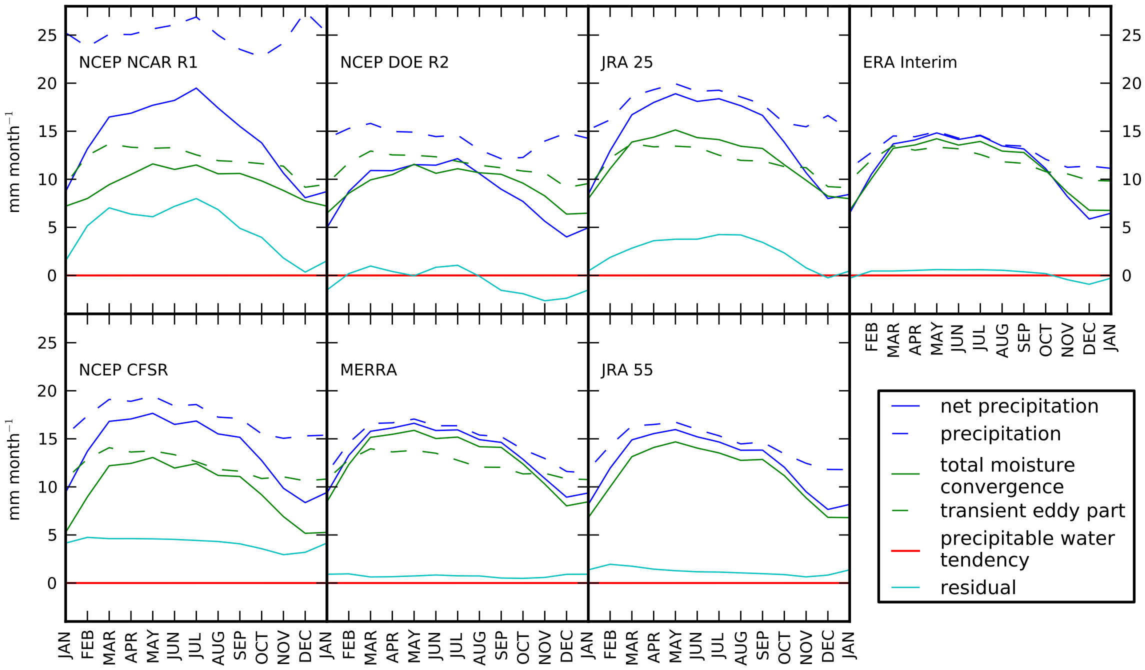

Figure 3.10: Seasonal cycle of the moisture budget for the Antarctic ice sheet. The residual term is equal to net precipitation minus convergence minus the rate of change of precipitable water.

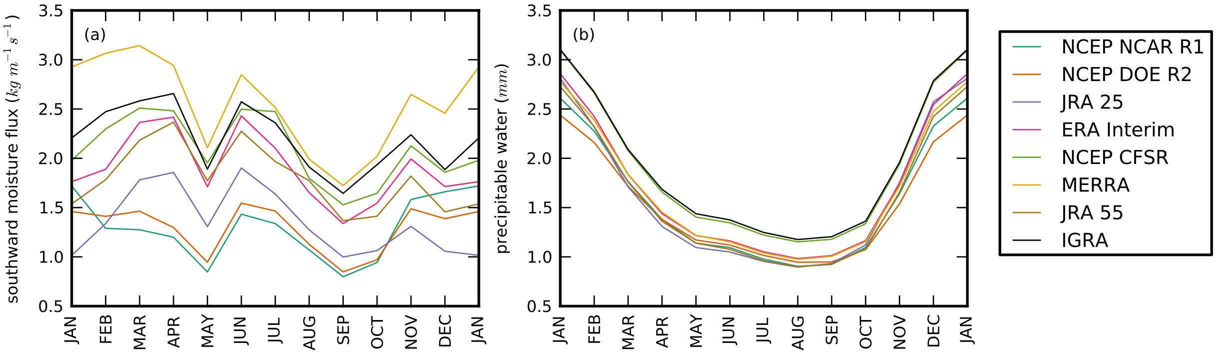

Figure 3.11: Annual cycle of the meridional moisture flux (a) and of precipitable water (b) in reanalyses and IGRA, averaged over all the radiosonde sites.

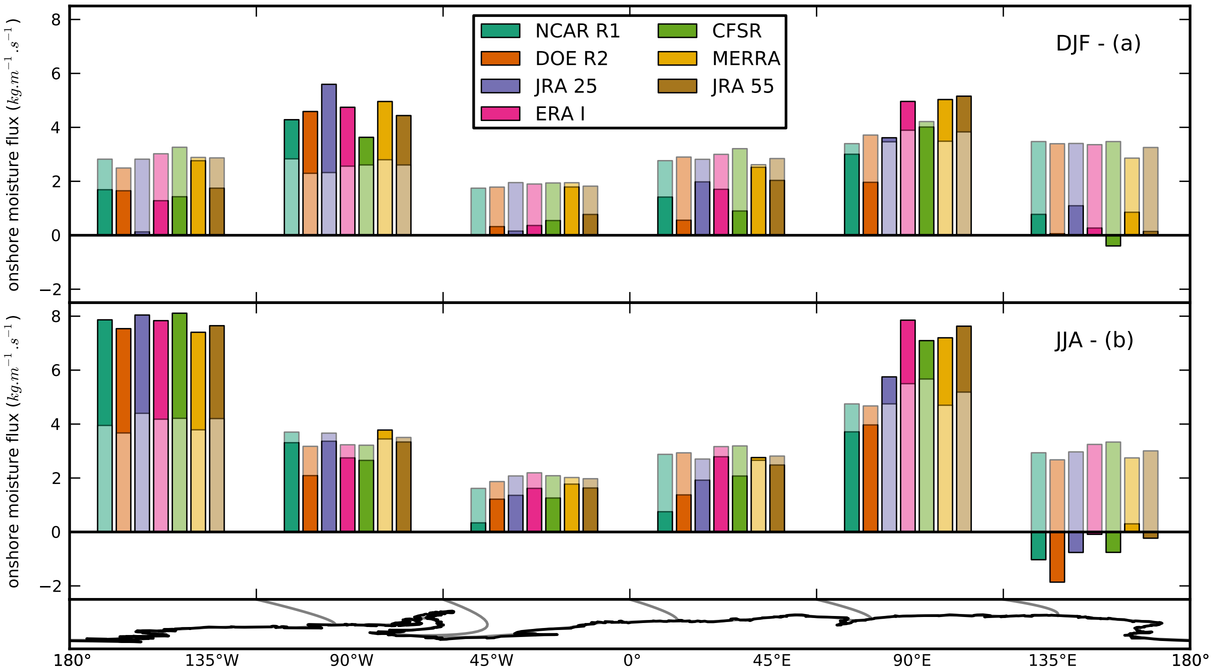

Figure 3.12: Same as Figure 3.8 but for summer (DJF, panel a) and winter (JJA, panel b).

troduction of AMSU in the late 1990s, ERA Interim by the increased assimilation of SSM/I radiances between 1992 and 2005 when the mission was ended.

We nonetheless display the time series for all the terms of the moisture budget (Figure 3.13) with our usual emphasis on moisture transport (first column). *Bromwich et al.* (2011) and *Nicolas and Bromwich* (2011) had excluded NCEP NCAR R1 (understandably), ERA Interim only extended to 1989 and JRA 55 was not yet released. However, we cannot escape the conclusion of the authors. Our time series share the same ambiguity : the observed patterns of interannual variability cannot be interpreted as real world phenomena with any confidence. The inter-dataset spread is greater than the interannual variability even for the moisture convergence variable.

As far as we know, radiosondes were only used to build moisture flux climatologies as in *Connolley and King* (1993) or *Cullather et al.* (1998). With longer records, we hope to exploit trends as well. The threshold we applied to the Arctic stations – at least 85% of valid days – is too demanding for Antarctica. There are fewer radiosonde launches and those few observations are more likely to be filtered by our quality checks. Figure 3.14 summarises the data availability at the nine IGRA stations on the coast active from 1979 to 2013. Before the 1990s, it looks as though several stations did not run a radiosonde program at all. In fact they did, but only in summer, or the launches were irregular and error-ridden. We cannot

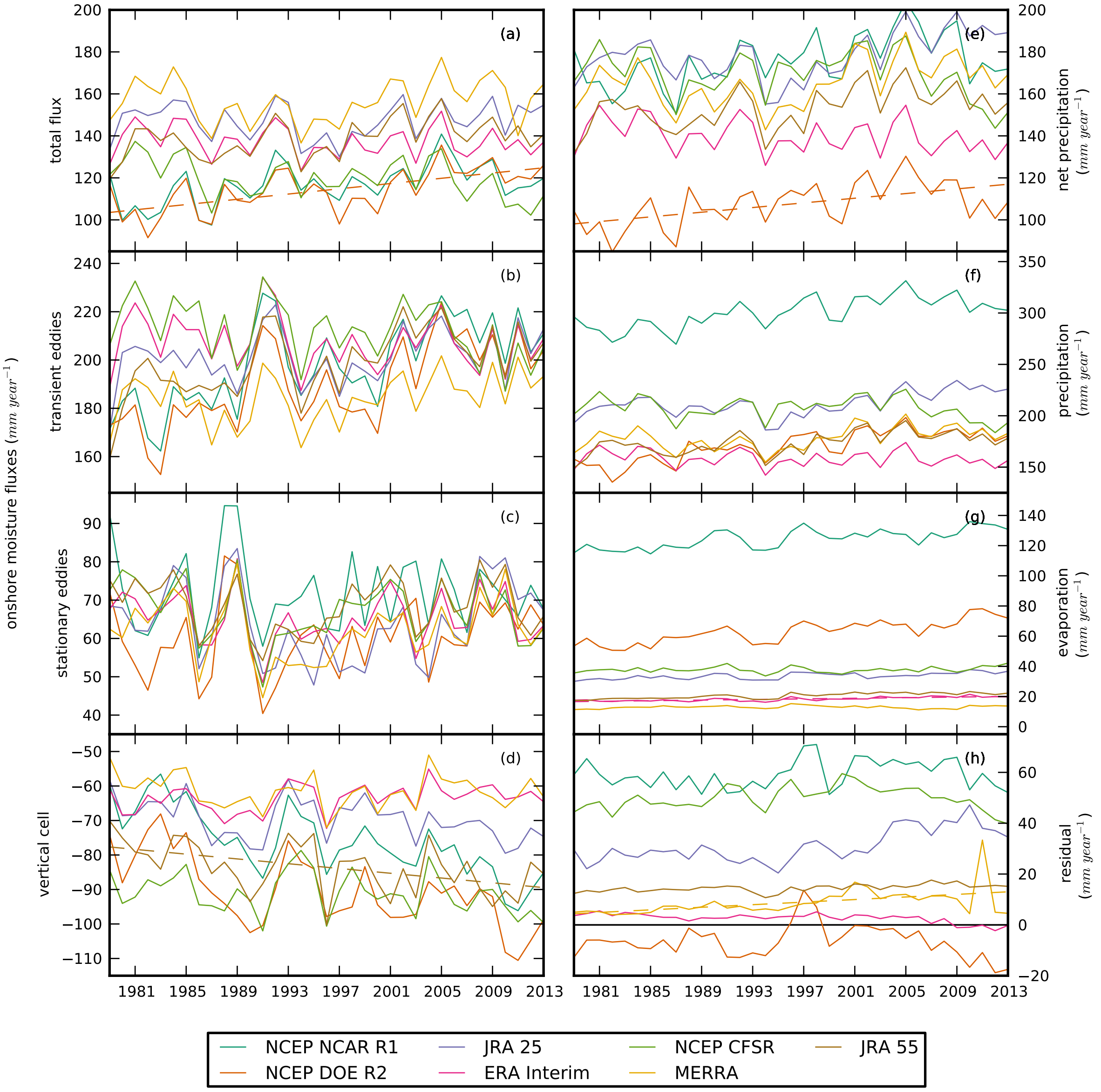

Figure 3.13: Time series of moisture convergence to the Antarctic ice sheet via the aerological method (a). On the smoothed boundary, the fluxes were decomposed into the transient eddy part (b), the stationary eddy part (c) and the vertical cell (c) according to Equation 1.12. Time series of the terms of the moisture budget for the said region : net precipitation or P-E via the physics output method (e), precipitation (f), evaporation (g) and the residual, i.e. the difference between the physics output and the aerological methods (h). The regression line of the variable is drawn (in dashes) if its trend is statistically significant at the 95% level (Student t-test).

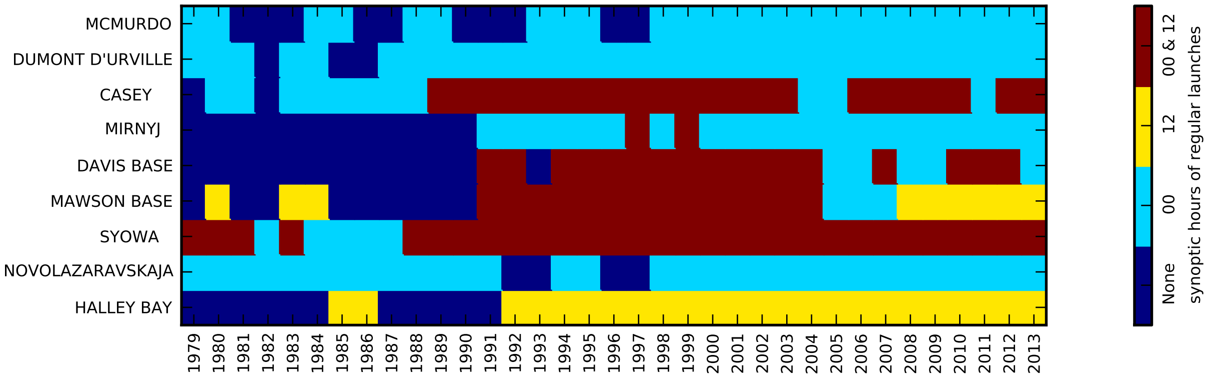

Figure 3.14: Average time of the radiosonde launch at the nine IGRA coastal stations. A station is considered to have regular observations at a given hour (midnight or midday) if it has more than 50% of valid soundings for this time of the day. ‘None’ refers to an absence of regular soundings.

build a time series by simply averaging the stations operational at a given time : in the 1990s, we can expect an artificial jump when new stations are taken into account. We rather compute anomalies per synoptic time, month and station and we average the anomalies, by analogy with worldwide surface temperature datasets e.g. *Jones* (1994).

Once we correct for the spatial heterogeneity of the data, we find statistically significant increases of the southward moisture transport (Figure 3.15, a). Except for Mirnyj and McMurdo, all stations report increases, with significance in the case of Halley, Syowa and Casey. Such trends were anticipated from climate model projections (*Gregory and Huybrechts*, 2006; *Krinner et al.*, 2007) but not observed (*Monaghan et al.*, 2006; *Bromwich et al.*, 2011). We must nevertheless issue three caveats. First, the spatial and temporal representativity of our result is questionable. Second, the radiosonde time series can be affected by changes in instruments and practices. Third, the trend is not the product of additional moisture, the expected mechanism. Indeed, the precipitable water content has not changed over the same period (Figure 3.15, b). The transient eddy component has increased but not significantly. The remainder of the trend is therefore due to a weakening of the mean flow, which was not predicted by climate models as far as we know.

To conclude, trends in the Antarctic are as surprising as in the Arctic. In both regions, the moisture fluxes were expected to increase because of additional humidity. The humidity in the Arctic did rise, but not the fluxes because of unfavourable winds. The Antarctic stayed as dry but the moisture convergence increased due to weaker equatorward mean winds and stronger poleward transient eddy fluxes.

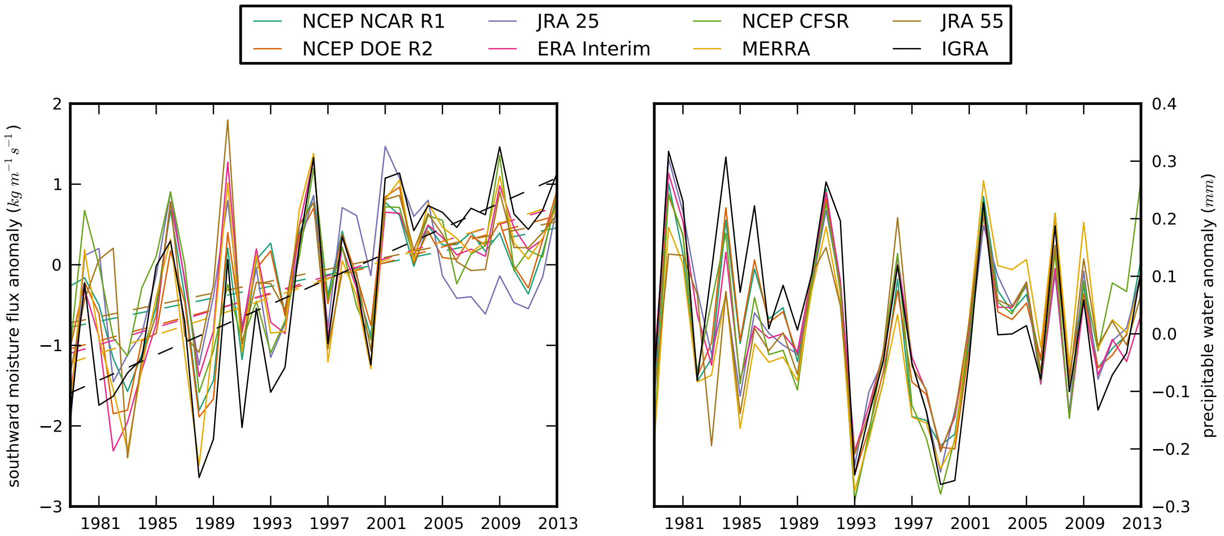

Figure 3.15: Anomalies of the southward moisture flux averaged over the IGRA coastal stations (a) ; idem with precipitable water. A regression line is drawn (in dashes) if the trend is statistically significant at the 95% level (Student t-test).

Chapter 4

The role of cyclones in moisture advection

4.1 Temporal scale decompositions

The two previous chapters have shown the predominant contribution of transient eddies to the moisture transport to the high latitudes : 90-92% at 70°N, 84-145% to the (smoothed) Antarctic ice sheet. Now we would like to delve deeper into the meaning of this statistic. How dependent is it on the choice of a temporal threshold ? How does it compare to spectral methods ?

Our original purpose was to identify the mechanisms responsible for moisture advection : we wanted to know which time scales contributed the most to the transports. Let $[0, A]$ be the period of study, in our case 35 years and $\overline{qv}$ the mean moisture flux at a given location and altitude. $a = A/N$ is a shorter time scale e.g. a month, and N the number of months in period A. What is the contribution of time scales shorter than a to $\overline{qv}$?

By analogy with fluid mechanics, the Reynolds decomposition lends itself to the study of turbulence on synoptic scales. For a given month $n \in \llbracket 0, N \rrbracket$, we divide any variable, say q, into its monthly mean and monthly anomaly :

$$q = \langle q \rangle_n + q' \text{ where } \langle q \rangle_n = \frac{1}{a} \int_{na}^{(n+1)a} q \, \mathrm{d}t \text{ and } q' = q - \langle q \rangle_n \tag{4.1}$$

Since q and v are correlated, the mean of their product is not the product of their means but $\langle qv \rangle_n = \langle q \rangle_n \langle v \rangle_n + \langle q'v' \rangle_n$. The remaining term is the “eddy” flux :

$$\langle q'v' \rangle_n = \frac{1}{a} \int_{na}^{(n+1)a} (q - \langle q \rangle_n)(v - \langle v \rangle_n) \, \mathrm{d}t \tag{4.2}$$

We now average the monthly decompositions over the whole period :

$$\langle \langle qv \rangle_n \rangle = \frac{1}{N} \sum_{n=0}^{N-1} \langle qv \rangle_n \tag{4.3}$$

This yields the complete Reynolds decomposition : $\langle \langle qv \rangle_n \rangle = \langle \langle q \rangle_n \langle v \rangle_n \rangle + \langle \langle q'v' \rangle_n \rangle$ which separates the contribution by time scales longer than a month from those shorter than a month.

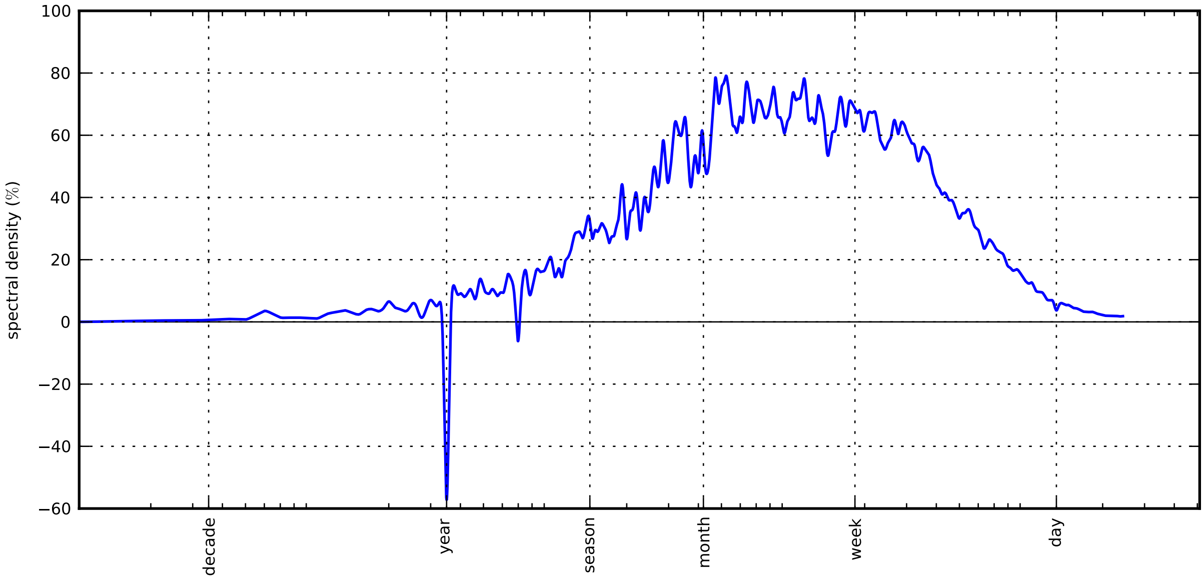

Figure 4.1: Periodogram of the mean moisture flux at 70°N for the period 1979-2013 from ERA Interim. The linear scale spectrum has been divided by $\frac{\mathrm{d}\log_{10} j}{\mathrm{d}j}$ to account for the logarthmic scale.

We can also expand q and v in their respective Fourier series, as in

$$q = \sum_{j\in\mathbb{Z}} q_j e_j \quad \text{with} \quad e_j = e^{2\pi i j t/A} \tag{4.4}$$

i is the imaginary unit and $\mathbb{Z}$ the set of integers, positive and negative. The product of q and v breaks down into :

$$qv = \sum_{j,k\in\mathbb{Z}^2} q_j\, v_k\, e_{j+k} \tag{4.5}$$

Since $\overline{e_j} = \delta_{j0}$, it follows that :

$$\overline{qv} = \sum_{j\in\mathbb{N}} f_j \quad \text{with} \quad f_j = \begin{cases} q_0 v_0 & \text{if } j = 0. \\ q_j v_{-j} + q_{-j} v_j & \text{otherwise.} \end{cases} \tag{4.6}$$

$\mathbb{N}$ is the set of postive integers. The terms with indices lower or equal to N correspond to periods of a month or more, those with indices higher than N correspond to periods less than a month, miroring the Reynolds decomposition. We average Equation 4.6 over the 70°N parallel using the time averaged weights from Equation 1.10. Figure 4.1 shows each time scale's share of the total moisture flux at 70°N. The periodogram peaks between one month and one week, which is consistent with the return time of cyclones. Interestingly, the annual cycles of humidity and meridional wind are anticorrelated.

We would like to relate the “mean flow” term of the Reynolds decompostion, $\langle\langle q\rangle_n \langle v\rangle_n\rangle$, to the Fourier series. After a number of calculations, detailed in the appendix, we came up with the following approximation.

$$\langle\langle q\rangle_n \langle v\rangle_n\rangle \approx \sum_{j\,\in\,\mathbb{Z}} q_j v_{-j}\ \mathrm{sinc}^2(\pi j/N) \tag{4.7}$$

The cardinal sine function is reminiscent of the effect of convoluting a signal with a rectangular window i.e. a moving average.

$$\begin{aligned} Q(t) &= \frac{1}{a}\int_{t-a/2}^{t+a/2} q(\tau)\ \mathrm{d}\tau \\ &= q_0 + \sum_{j\,\in\,\mathbb{Z}^*} q_j\ [e_j]_{t-a/2}^{t+a/2} \\ &= \sum_{j\,\in\,\mathbb{Z}} q_j\ \mathrm{sinc}(\pi j/N)\ e_j(t) \end{aligned} \tag{4.8}$$

We multiply Q by V :

$$Q(t)\ V(t) = \sum_{k,j\,\in\,\mathbb{Z}} q_j\, v_k\ \mathrm{sinc}(\pi j/N)\ \mathrm{sinc}(\pi k/N)\ e_{j+k}(t) \tag{4.9}$$

Averaging over $[0, A]$ yields the same result as $\langle\langle q\rangle_n \langle v\rangle_n\rangle$.

We perform several Reynold decompositions of the meridional moisture flux at 70°N with temporal cutoffs ranging from 35 years to 6 hours and compute the mean flow contribution to the total fluxes (Figure 4.2). The output of the Fourier decomposition and cardinal sine formula (Equation 4.7) are plotted alongside. This time, the spectrum in Figure 4.1 is displayed as a cumulative distribution function rather than a density. Each coefficient’s contribution to the total is summed, up to a certain temporal threshold given by the horizontal axis. The negative contribution of the annual cycle shows up as a small drop in the green curve ; it is absent from the two others. From Equation 4.7, it was unlikely that Fourier and Reynolds decompositions would yield similar results. The overall aspect is similar but the Fourier distribution is shifted towards the longer frequencies. As expected, the output from moving averages (computed using Fourier coefficients) cannot be distinguished from the Reynolds decomposition. Using these two methods, we find the familiar 92% figure for a time scale of a month. The Fourier decomposition gives a mere 76%. Unfortunately, there is no reason to trust one method more than the other. Though they disagree on the details, they do paint a similar picture : scales shorter than a month dominate the moisture advection to the Arctic. These formal decomposition methods have done good service but their physical meaning is not clear. To move further, we need methods more discriminative of the actual meteorological mechanism at play.

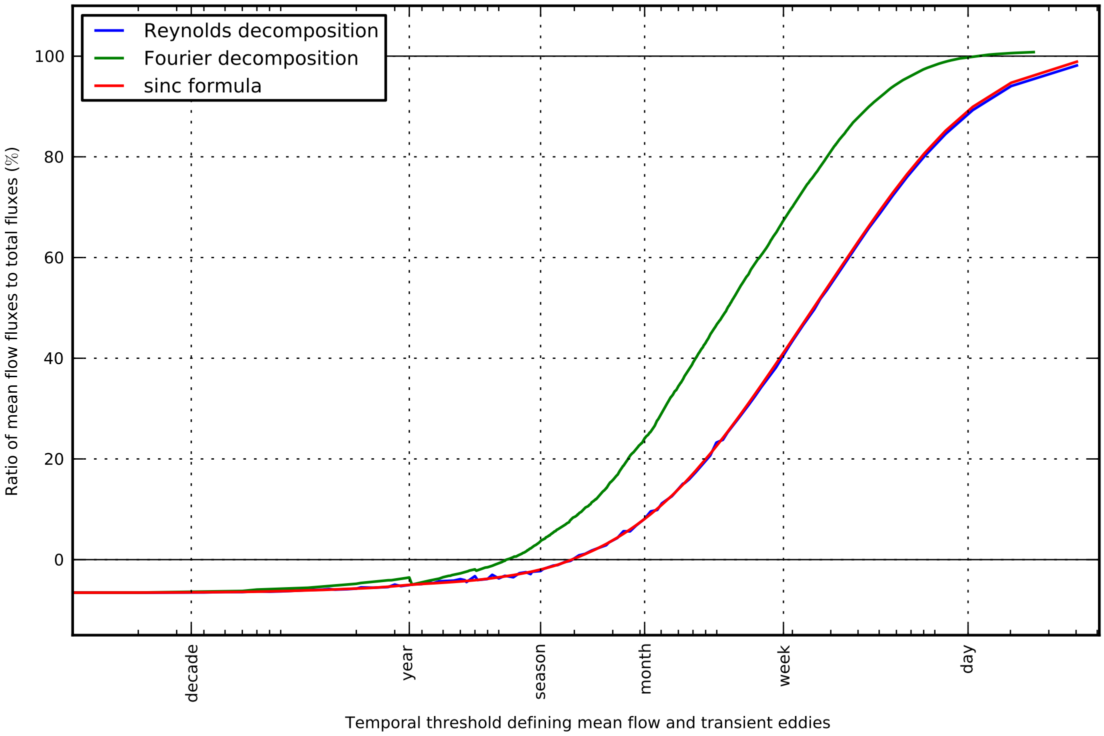

Figure 4.2: Relative contribution of the mean flow to the moisture transports through 70°N depending on the time scale defining mean flow and transient eddies and the method chosen : Reynolds, Fourier or the cardinal sine formula ; based on ERA Interim fluxes for the 1979-2013 period.

4.2 Contribution of individual cyclones

The term “transient eddies” is suggestive of cyclones. Several authors, ourselves included, have implied the connection. For example, *Karoly* (2015) talks of “synoptic-scale cyclones (also known as transient eddies).” Indeed, extratropical cyclones make good suspects : they occur on the right time scales and they generate meridional winds that put the middle and the high latitudes into contact, leading to transports of moisture and heat. *Sorteberg and Walsh* (2008) demonstrated that cyclone activity and moisture transport were significantly correlated in the Arctic.

Extratropical cyclone were formerly known as barometric depressions i.e. minima of the sea level pressure (SLP) fields. We defined transient eddy fluxes as $\overline{q'v'}$; likewise, we define high frequency variations of the SLP as $\overline{p_0'p_0'}$. Before the advent of tracking methods, this is how storm tracks were located (e.g. *Rogers* (1997)). Using six-hourly fields instead of monthly averages, one can follow individual cyclones : designated features can be traced on gridded fields from one time step to the next (*Hodges*, 1994). The identification criteria varies from method to method. The cyclone trajectories of the Institute of Oceanolgy, Russian Academy of Science, which we use, rely on SLP minima (*Gulev et al.*, 2001; *Rudeva and Gulev*, 2007; *Tilinina et al.*, 2013) but *Sorteberg and Walsh* (2008) tracked maxima of the 850 hPa vorticity. An example of a so-called spaghetti plot is shown in Figure 4.3 (a). The SLP fields used by the algorithm are from ERA Interim. Figure 4.3 (b) reveals the two main storm tracks : in the North Atlantic and North Pacific, as well as other regions of cyclonic activity : the Baffin Bay and Northern Eurasia. Some of these regions overlap with the areas of intense transient eddy fluxes in Figure 2.6.

Over the whole archive, we isolate the cyclones crossing the 70°N parallel. Figure 4.4 shows storm-centered composites of several fields in the vicinity of these cyclones at the time of the crossing. The moisture flux vector field (arrows) is arranged in an eddy pattern centered on the cyclone center, superimposed on the mean westerly circulation. The magnitude of the zonal flux decreases with the latitude, along with the integrated water content (coloured contours). The northward flux to the east of the cyclone feeds on the warm and moist mid-latitude air whereas to the west of the cyclone, the southward flux advects cold and dry Arctic air. The zonal patern of integrated water vapour is subsequently deformed by the eddy revealing the cold and warm sectors of the cyclone and a closed contour of especially moist air near the cyclone center. The meridional moisture fluxes are maximal at

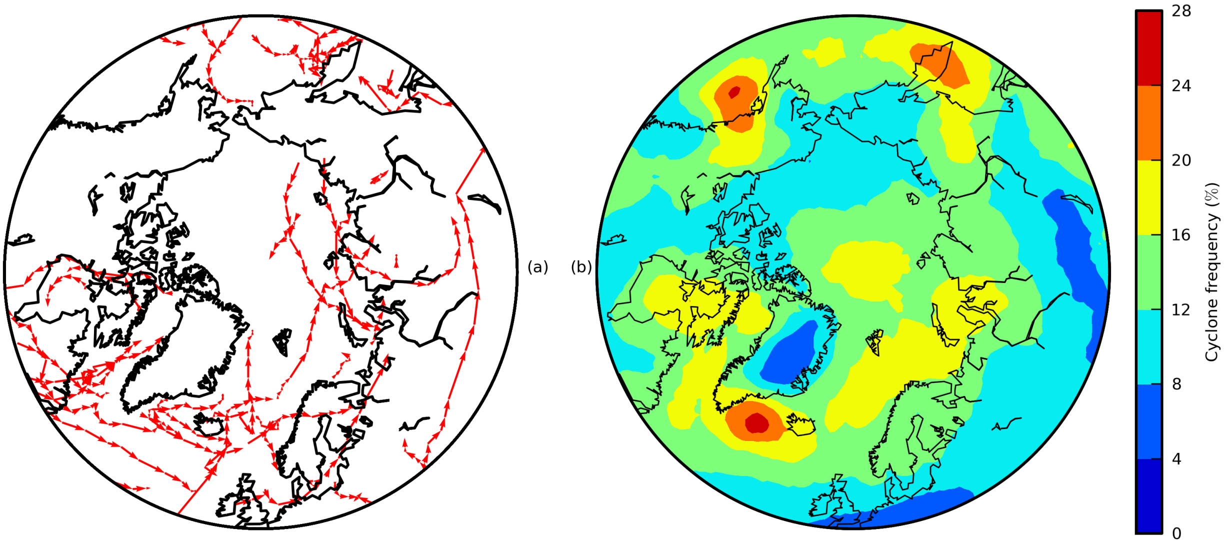

Figure 4.3: The trajectories of the first 50 cyclones of 1979 according to the IORAS algorithm running on ERA Interim SLP fields (a). With the same method and data from 1979 to 2013 : map of cyclone frequencies i.e. percentage of the time at least one cyclone was within 500 km of ny point.

the latitude of the cyclone center, 70°N. The moisture flux converges to the northeast of the cyclone center, the head (*Wallace and Hobbs*, 2006). In the cold sector, the advection of dry air over a relatively warmer surface leads to a flux divergence i.e. net evaporation.

Plus or minus noise, the composited patterns are visible on individual cyclones, as in the case study presented on Figure 4.5. The longitude profile of meridional moisture flux at 70°N shows the characteristic southward advection in the cold sector, and northward advection in the warm sector. What share of these fluxes can we attribute to the cyclone ? We built a heuristic algorithm to answer the question objectively.

1. smooth the original longitudinal flux profile (red curve in Figure 4.5) with a band-pass filter (blue curve)
2. assert that the slope of the smoothed profile at the cylone center is positive
3. go west along smoothed the profile
    - 3.1. assert that the first westward minimum is negative
    - 3.2. if the smoothed profile becomes positive or reaches a minimum
        - define the western boundary of the cyclone (purple dot)

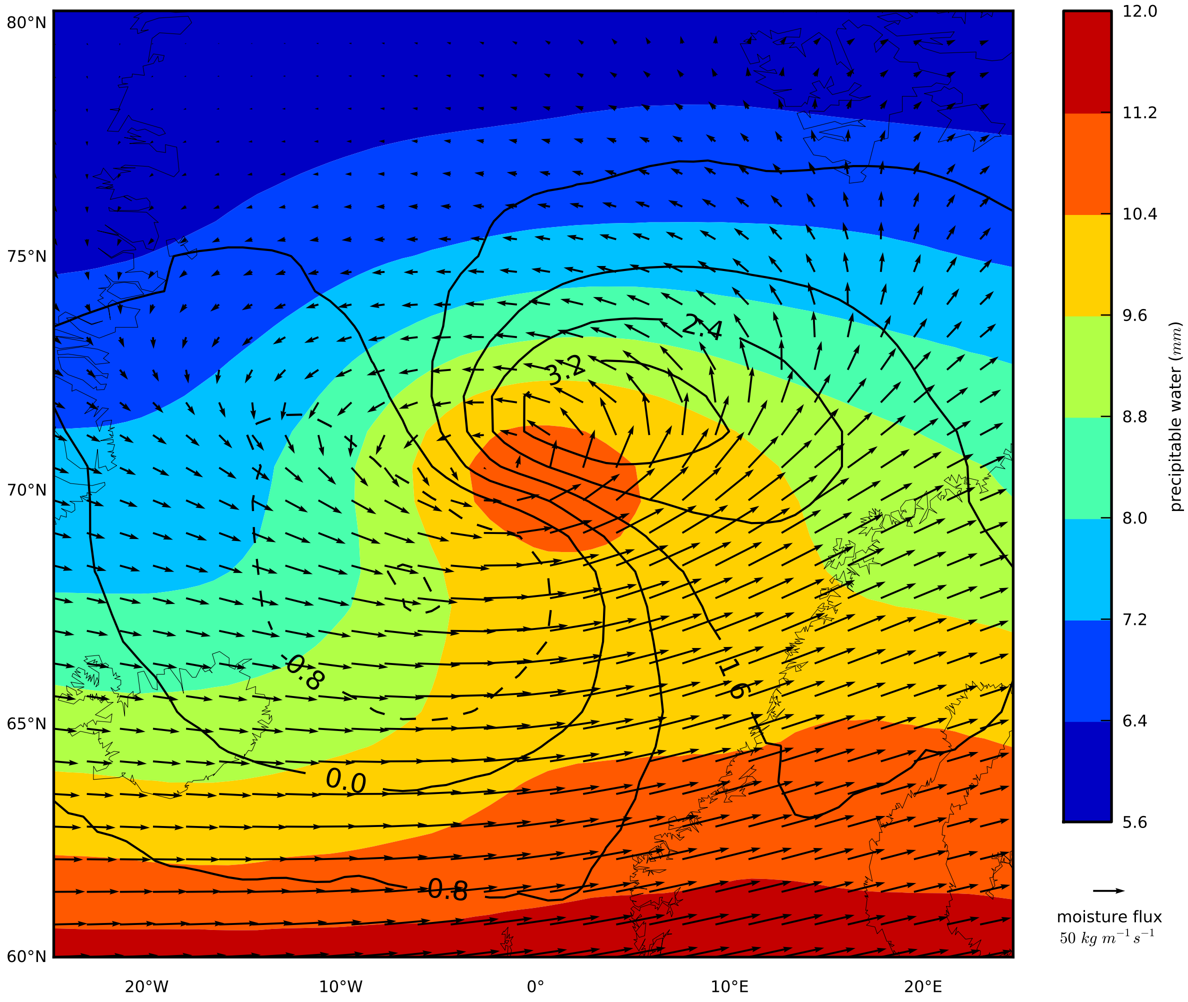

Figure 4.4: Storm centered composites of precipitable water (coloured contours), moisture fluxes (arows) and moisture convergence (black contours : solid if positive, dashed if negative) using IORAS tracks and ERA Interim fields (1979-2013). The composited cyclones were crossing the 70°N parallel at all longitudes ; the coastlines for longitude 0° were drawn to give a sense of scale.

4. return to the cyclone center
5. go east along the smoothed profile
    5.1. assert that the first eastward maximum is positive
    5.2. if the smoothed profile becomes negative or reaches a maximum
        - define the eastern boundary of the cyclone (yellow dot)
6. integrate the original moisture profile from the western to the eastern boundary

During the 35 year period, a total of 24 225 cyclones crossed the 70°N parallel according to the IORAS dataset. An individual cyclone may be counted several times. Of these cyclones, 9.6% failed step (2) and another 7.5% failed steps (3.1) or (4.1). Surprisingly, the remaining cyclones have contributed to both negative (39%) and positive (61%) net fluxes with a mean of $+28 \cdot 10^6$ kg s^{-1} (Figure 4.6, a). The positive tail is quite heavy : the top decile contributed to 75% of the mean. The figure drops to 35% if we only consider cyclones making a positive net contribution. The importance of extreme atmospheric transport events has already been underlined by *Messori and Czaja* (2013) for heat and *Woods et al.* (2013) for moisture.

The mode of the distribution is zero : the most common case is cyclones having no effect at all. Was the tracking scheme particularly sensitive to weak cyclones or were these cyclones actually vigorous, but with compensating cold and warm sectors ? This time, we take the absolute value of the meridional moisture flux before we perform the integration between the western and eastern boundaries of the cyclone (Figure 4.6, b). The first hypothesis was correct : most cyclones have a weak effect on the meridional moisture fluxes. The cyclones with no effect whatsoever are nonetheless rare. It would be interesting to apply the algorithm to random “pseudo-cyclones” to see if the tracking scheme is prone to false positive errors. Conversely, we could restrict ourselves to deep cyclones only and see if they are indeed responsible for the extreme transport events.

4.3 Contribution of all cyclones

The 24 225 cyclones we examined in the previous section are only a small subset of the cyclones that contribute to the moisture transport at 70°N. Intuitively, the further the cyclone center is from 70°N, the smaller his influence on the transport at 70°N. Its signature on the moisture flux field will likely be indistinguishable from noise, especially to our algorithm.

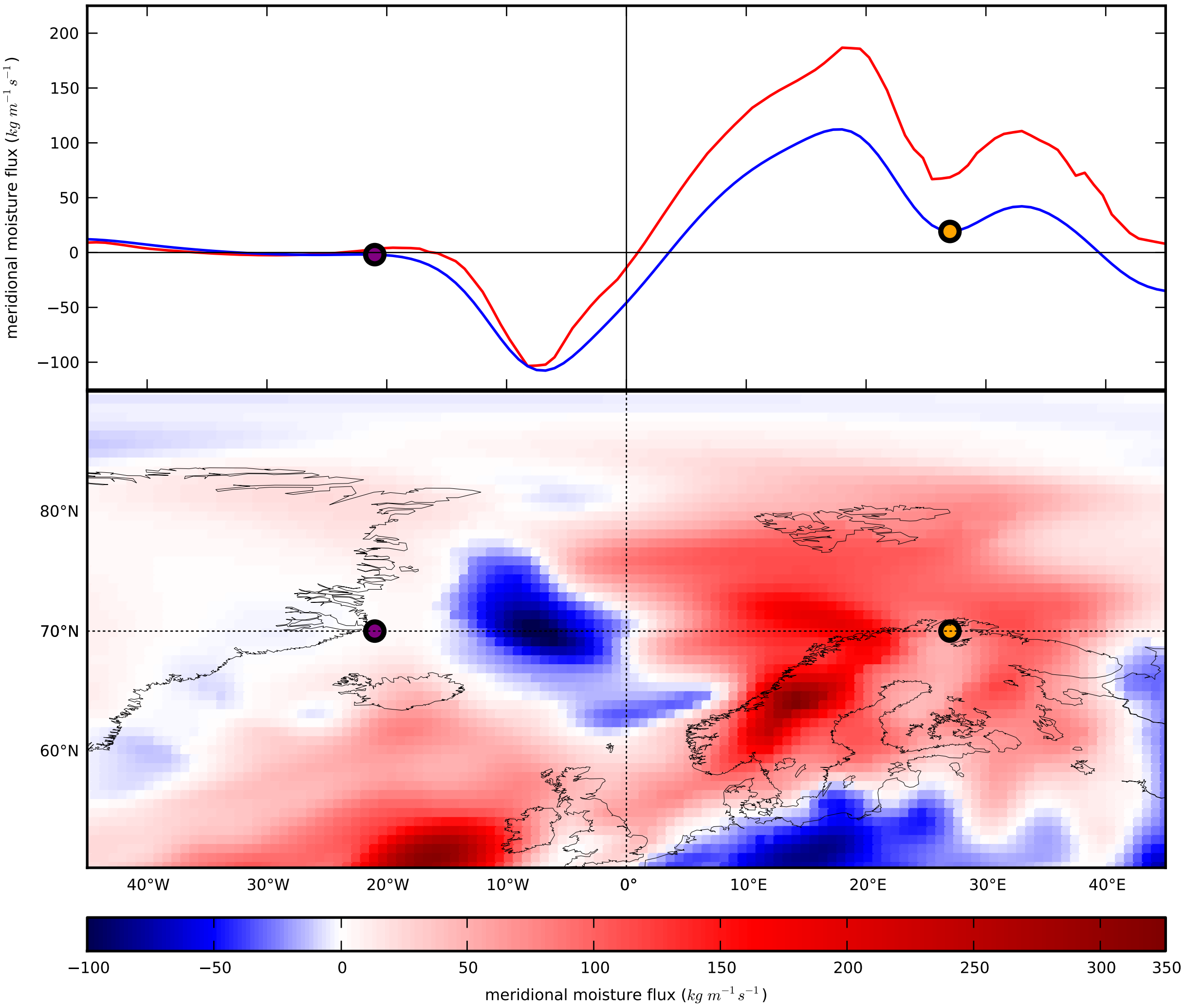

Figure 4.5: Example of our flux attribution algorithm on a cyclone crossing the 70°N parallel (2008/02/21). The top panel shows the meridional moisture flux at 70° (red curve) and the band-passed version on which the algorithm operates (blue curve). Below is a map displaying the fluxes in the neighbourhood of the cyclone. The purple and orange points signal the western and eastern boundaries of the cyclone.

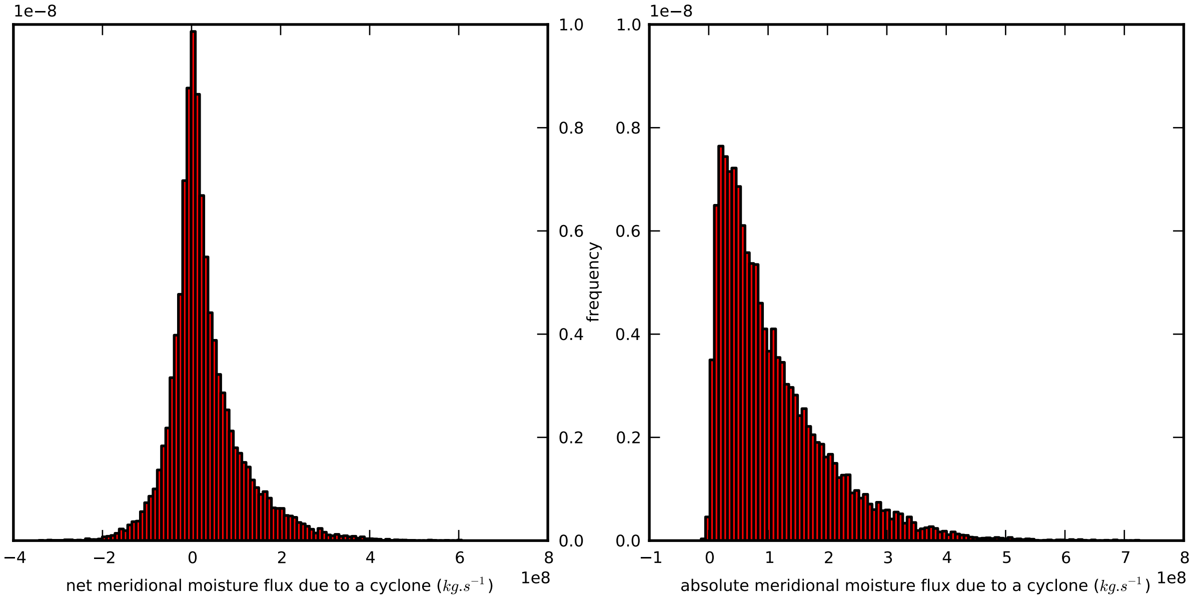

Figure 4.6: Distributions of fluxes due to cyclones crossing the 70°N parallel during the 1979-2013 period from ERA Interim data.

When cyclones are located at 70°N – the best case scenario – it rejects 17% of cyclones. Paradoxically, the flux profile composites of the rejected cyclones are not far removed from Figure 4.5 (a). The compositing removed the noise that prevented the attribution algorithm from functioning : the composites can be fed into the algorithm without fear of rejection. On the downside, we can no longer attribute a flux to a single cyclone.

The compositing procedure is illustrated by Figure 4.7. For each time step in the 1979-2013 period,

(a) load the corresponding meridional moisture flux field from the reanalysis and locate the cyclones present at that time (green dots)

(b) isolate the fluxes at 70°N, discard the rest
locate which cyclone is the closest to any point at 70° N

(c) assign the fluxes to each cyclone's latitude
only if the cyclone is the closest

(d) rotate the different profiles so as to place the cyclones on the prime meridian

The output of each time step is then averaged over the whole period.

Figure 4.8 (a) shows the output of the algorithm without the instructions in italics. Let us interpret the meaning of the blue-white-red colour at a given latitude ϕ and longitude

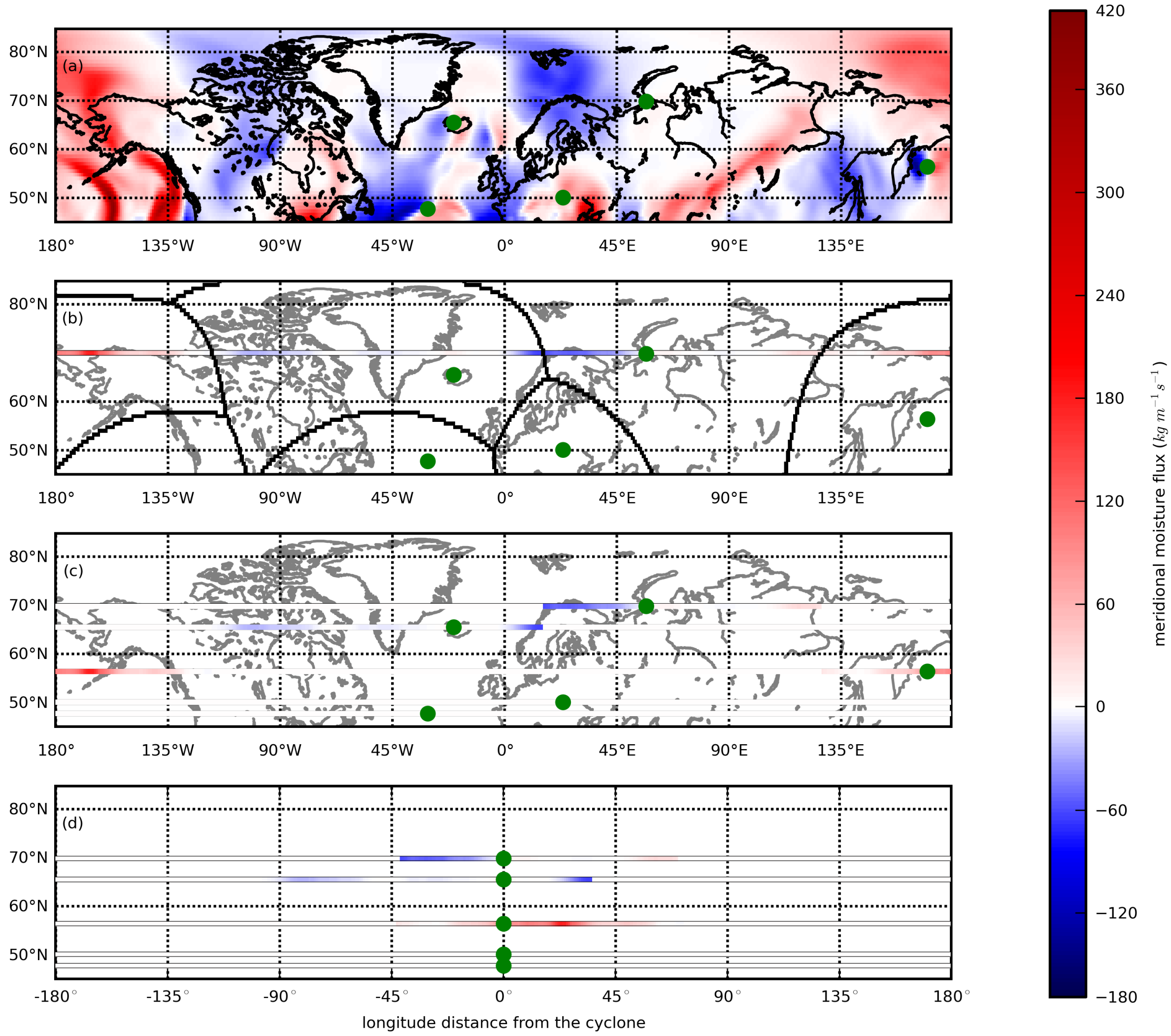

Figure 4.7: The four steps of the cyclone compositing algorithm, applied to the 1^{st} of January 1979. The green points locate the cyclones. The bold lines in panel (b) define each cyclone's closest neighbours.

λ. When a cyclone is present at latitude ϕ, a point at 70°N and λ degrees of longitude to the east of the cyclone experiences on average the meridional moisture flux symbolized by that colour. For example, a cyclone located between 50°N and 80°N is likely to affect the fluxes at 70°N. Points at 70°N less than 45° of longitude to the east of the cyclone would be located in its warm sector. They would therefore experience northward fluxes under those conditions. Points at 70°N located less than 45° of longitude to the west of the cyclone would find themselves in its cold sector where on average moisture fluxes would be negative. This is the explanation for the blue and red patterns on either side of the prime meridian : they represent the influence of the cold and warm sectors of cyclones. Points at 70°N that are more than 45° degrees of longitude to the east or to the west of the cyclone are unaffected by its presence. This is also true when the cyclone is located below 50°N : the fluxes at 70°N are independent of his presence.

We are now tempted to apply the attribution algorithm defined in the previous section on the composited profiles (green contour on Figure 4.8). Qualitatively, the objective boundaries make sense though they look spread-out. Quantitatively, the fluxes inside the boundary amount to 15.7 kg m^{-1} s^{-1}. The total fluxes, both inside and outside, amount to an improbable 90.2 kg m^{-1} s^{-1} when we would expect no more than the average moisture fluxes through 70°N, 6.9 kg m^{-1} s^{-1}.

Cyclones are an ubiquitous phenomenon : we must partition the 70°N profile or we will be attributing the same flux to several cyclones. The instructions in italics share the profile among the closest cyclones to avoid double-counts. The pink background colour has been replaced with white (zero fluxes) in Figure 4.8, (b). The green contour is more narrow ; it encloses 6.1 kg $\mathrm{m}^{-1}\mathrm{s}^{-1}$. The regions outside the boundary weigh 0.8 kg m^{-1} s^{-1} and the whole is 6.9 kg $\mathrm{m}^{-1}\mathrm{s}^{-1}$. From these calculations, cyclones are responsible for 89% of the advection through 70°N, which is not far from the share of transient eddies according to the Reynolds decomposition (92%).

Actually, we have come up with a tool rather than a final result. We merely showed that most of the moisture flux occurred in the neighbourhood of a cyclones. Now, as we said, cyclones are a very frequent phenomenon. The 89% of moisture fluxes we attributed to cyclones were due to 78% of longitudes and time steps. Put this way, the proximity to a cyclone is not a good predictor of above average fluxes.

In designing the algorithm, we guessed that cyclones far from 70°N would have no effect on the moisture fluxes at 70°N so we stratified the cyclones by latitude. We know

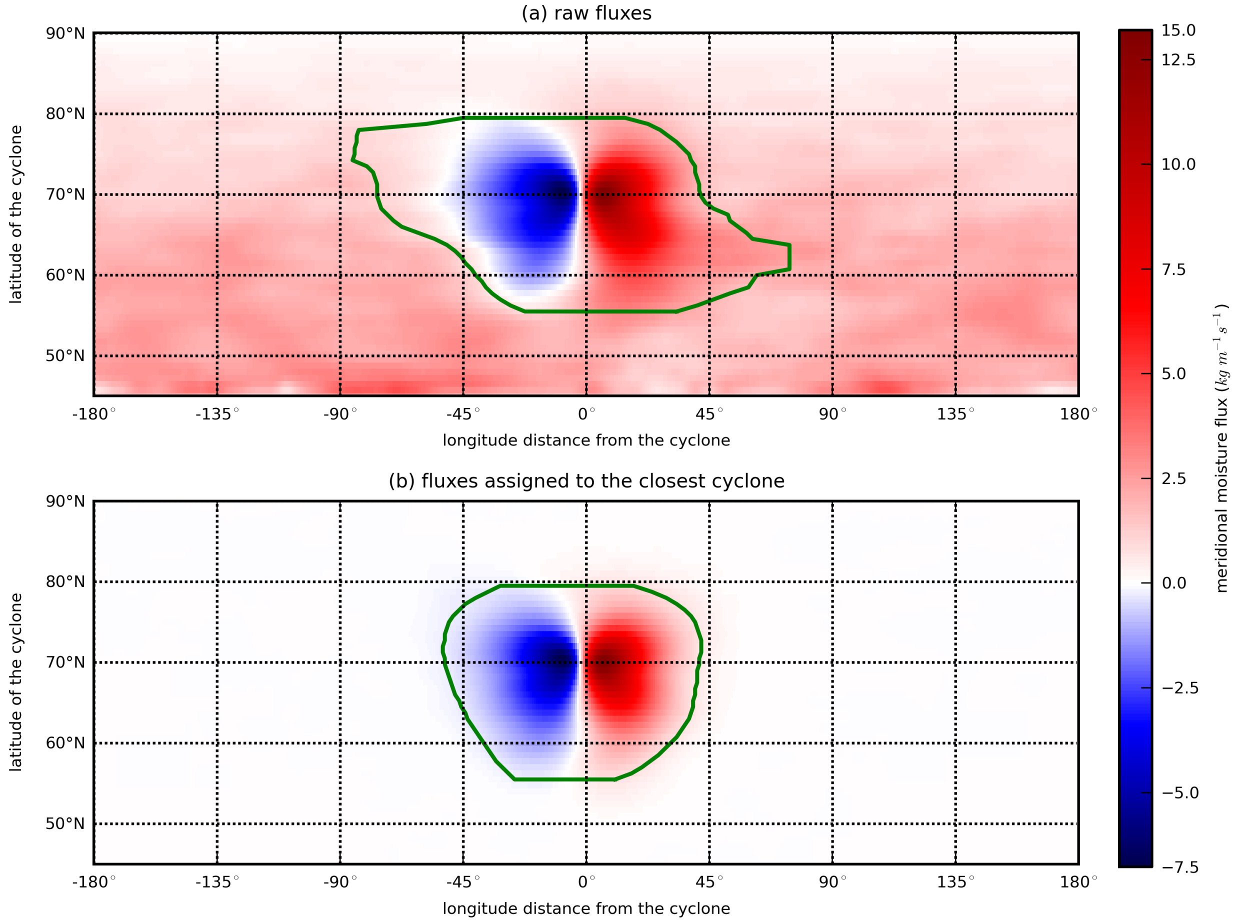

Figure 4.8: Output of the flux attribution algorithm on the profile composites without partitioning the fluxes between cyclones (a) and with a division of the fluxes between the closest cyclones (b).

from the previous section that even among the cyclones crossing 70°N, most have little effect on the moisture flux. We would like to extend the stratification to an index of the cyclone's strength. For instance, *Sorteberg and Walsh* (2008) did not just correlate the number of cyclones with the moisture fluxes : they correlated the accumulated cyclone central vorticities at 850 hPa with the moisture fluxes. We decide to sort the cyclones by their central SLP and to divide them into deciles, which we divide into even smaller bins depending on the latitude of the cyclone. For each SLP-latitude bin, we build composites of the storm-centered 70°N meridional moisture flux profile, excluding locations on the parallel that are closer to some other cyclone. We then apply the attribution algorithm to the composites of each SLP-latitude bin. Finally, we sum the contributions from the bins of matching SLP and plot the share of each decile (Figure 4.9). Unsurprisingly, the deeper the cyclone, the stronger the fluxes (red line) and the more longitudes it affects (blue line). The first decile is responsible for 30% of the mean fluxes. By the fourth decile, the fraction of fluxes due to cyclones is the same as the fraction of 70°N they affect. Cyclones belonging to the remaining deciles bring about below average fluxes. A minority of deep cyclones is therefore associated with the majority of the moisture transport to the Arctic.

The importance of extreme events has already been highlighted by *Woods et al.* (2013). A limited number of events (14 per year) is responsible for 28% of the moisture fluxes to the Arctic during winter according to the authors. These events coincided with large scale blocking conditions. *Liu and Barnes* (2015b) attributes the extreme transport events more specifically to Rossby wave breaking. In East Antarctica, *Gorodetskaya et al.* (2014) linked episodes of exceptionally heavy snowfall to atmospheric rivers. These phenomena are likely to occur simultaneously with cyclones and will be counted as such by our algorithms. The next methodological challenge will be to discriminate between the two effects.

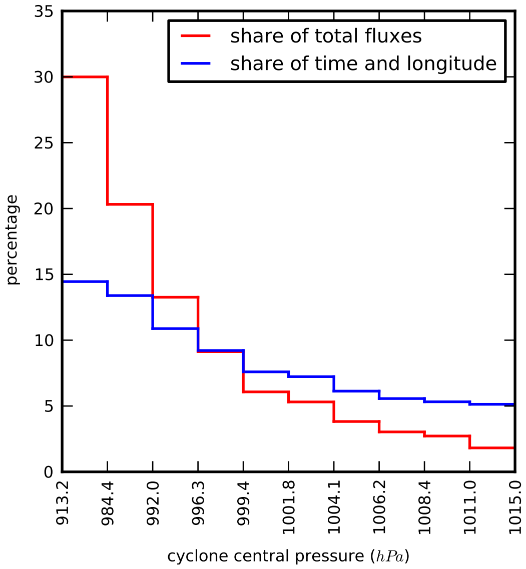

Figure 4.9: Share of moisture fluxes due to cyclones depending on their strength, using the central SLP to sort them into deciles.

To do so, we should exploit both the harmonic analysis of Section 4.1 and the cyclone trajectories of Sections 4.2 and 4.3. Using wavelets, the fluxes can be expressed as the sum of basic functions representing the different scales at work. Unlike Fourier harmonics, these functions have a compact support and are thus localised in time and space : they can be assigned to specific cyclones. With wavelets, we would able to share the credit between the large scale flow and the embedded cyclones.

Conclusions

We analysed the atmospheric water budget of both polar regions in seven reanalyses for the 1979-2013 period from the perspective of moisture transport. Moisture fluxes are computed from analysed winds and humidities unlike precipitation and evaporation, which are forecasted. They are less affected by the model spin-up or by changes in the observation system. If constrained by enough observations, reanalyses will estimate moisture transport consistently. Generally speaking, they can be computed reliably using data archived on pressure levels and without mass-correction. Small domains aside, moisture fluxes can be conflated with atmospheric water fluxes.

In the Arctic, the evaluation of the atmospheric moisture transport in the reanalyses against the radiosonde data demonstrated a qualitative agreement in terms of longitudinal, vertical and temporal patterns but also a quantitative difference, i.e., a 6-13% overestimation of the moisture fluxes by the reanalyses compared to in situ data. Net precipitation and moisture convergence are not in balance. In fact, the inter-dataset standard deviation of the net precipitation is nearly ten times that of the moisture convergence (45 mm year^{-1} compared to 5.1 mm year^{-1}). The meridional moisture transport to the Arctic is largely dominated by transient eddies, which explain 88-94% of the total transport at 70°N. The reason for this result is the averaging of the mean flow fluxes : the regions of northward mean flow – the North Atlantic, Baffin Bay and the North Pacific – are offset by regions of southward mean flow – over Canada and Western Russia. In contrast, the transient eddy transport is always northward, with peaks along the storm tracks. In spite of the magnitude of the annual cycle, with transports almost doubling from winter to summer, differences between datasets remain minor throughout the year. On interannual scales, most datasets depict a locally driven intensification of the water cycle : precipitation increases because of changes in local evaporation, not due to moisture imports. The growing atmospheric humidity in the lower troposphere does not result in an increase of the northward moisture transport because the correlation of humidity and meridional wind at these levels has weakened.

In Antarctica, the estimates of moisture convergence – 117 to 156 mm per year – are almost as spread out as net precipitation – 108 to 178 mm per year. The lack of observations is all the more conspicuous given the spatial heterogeneity of the mean flow winds : the katabatic winds are concentrated in distinct outlets on the coast and in the lower model levels. The transient eddies occur at higher altitudes and are represented more consistently in the reanalyses. They more than compensate the disposal of moisture by the mean flow. Instead of the reanalyses, prone to artefacts, we looked to radiosonde observations for indications of the interannual variability. In spite of an unchanged precipitable water content, the southward moisture transport has increased significantly, due to a weakening of the mean flow and stronger transient eddy fluxes. When analysing trends, the Reynolds decomposition reminds that the total fluxes do not depend on the average humidity only but also on the mean winds and, more importantly, on both variables' second order moments.

In order make its physical interpretation clearer, we began by reframing the Reynolds decomposition in the broader context of harmonic analysis. In the case of moisture transport through 70°N, the two methods are slightly different quantitatively but both agree that the lion's share occurs on time scales shorter than a month. We questioned the identification of transient eddies with extratropical cyclones by computing an independent estimate of cyclones' contribution to moisture transport. The percentage is remarkably close to the Reynolds' estimate : 89% and 92% respectively. However, cyclones are commonplace and most of them cause very little advection. On the other hand, the deepest ten percent are responsible for 30% of the moisture fluxes through 70°N.

Although transient eddies dominate moisture advection to the polar regions, several studies have shown how dependent they are on larger temporal and spatial scale patterns. *Sorteberg and Walsh* (2008) demonstrated that cyclones entering the Arctic are largely responsible for the poleward moisture advection but they also noted that the number of cyclones passing over the Greenland Sea depends on large scale circulation patterns, as reported earlier by *Tsukernik et al.* (2007). *Woods et al.* (2013) also argued along these lines, positing that blocking high pressure systems steer cyclones towards the pole and lead to intense moisture intrusions. In this respect, further analysis should be conducted to clarify the interplay between transient eddies and the large-scale flow, relying on a detailed analysis of cyclone activity (*Tilinina et al.*, 2013, 2014) which may be combined with a wavelet decomposition of the fluxes.

Similar studies with refined diagnostics can be extended to regional and long-term reanalyses. A natural choice would be the recent Arctic System Reanalysis (*Bromwich et al.*, 2015), which was produced with a high-resolution version of the non-hydrostatic Polar Weather Research and Forecast model and assimilated more data regionally than the global reanalyses. To understand the Arctic hydrological cycle on multidecadal time scales, it is also important to examine reanalyses not limited to the satellite era, such as NOAA ESRL 20^{th} Century

Reanalysis (*Compo et al.*, 2011), ERA 20C (*Hersbach et al.*, 2015a) and ERA CLIM (*Hersbach et al.*, 2015b). The analysis of moisture transports in these products would enable an understanding of the mechanisms steering the Arctic hydrological cycle during the time of the so-called early twentieth century Arctic warming (*Bengtsson et al.*, 2004b; *Brönnimann*, 2009; *Yamanouchi*, 2011).

Our assessement for both polar regions should serve as a standard to evaluate the historical runs of the CMIP5 ensemble of climate models and to clarify the extent to which they reproduce the features of the polar hydrological cycle and their changes in a warming climate. Existing assessments of climate model projections of the Arctic hydrological cycle (*Kattsov and Walsh*, 2000; *Kattsov et al.*, 2007; *Rawlins et al.*, 2010) and of the Antarctic surface mass balance (*Gregory and Huybrechts*, 2006; *Krinner et al.*, 2007) mainly cover evaporation, precipitation and runoff. These assessments will benefit from estimates of moisture advection, which shed additional light on the mechanisms of change and the model capacity to represent these mechanisms.

Bibliography

Allan, R. P., C. Liu, M. Zahn, D. A. Lavers, E. Koukouvagias, and A. Bodas-Salcedo (2013), Physically consistent responses of the global atmospheric hydrological cycle in models and observations, in *The Earth's Hydrological Cycle*, pp. 533–552, Springer.

Arthern, R. J., D. P. Winebrenner, and D. G. Vaughan (2006), Antarctic snow accumulation mapped using polarization of 4.3-cm wavelength microwave emission, *Journal of Geophysical Research: Atmospheres*, *111*(D6).

Bengtsson, L., S. Hagemann, and K. I. Hodges (2004a), Can climate trends be calculated from reanalysis data?, *Journal of Geophysical Research: Atmospheres (1984–2012)*, *109*(D11).

Bengtsson, L., V. A. Semenov, and O. M. Johannessen (2004b), The early twentieth-century warming in the Arctic-A possible mechanism, *Journal of Climate*, *17*(20), 4045–4057.

Bengtsson, L., K. I. Hodges, S. Koumoutsaris, M. Zahn, and N. Keenlyside (2011), The changing atmospheric water cycle in Polar Regions in a warmer climate, *Tellus A*, *63*(5), 907–920.

Bintanja, R., and F. Selten (2014), Future increases in Arctic precipitation linked to local evaporation and sea-ice retreat, *Nature*, *509*(7501), 479–482.

Boisvert, L. N., T. Markus, and T. Vihma (2013), Moisture flux changes and trends for the entire Arctic in 2003–2011 derived from EOS Aqua data, *Journal of Geophysical Research: Oceans*, *118*(10), 5829–5843.

Bosilovich, M., et al. (2006), NASA's modern era retrospective-analysis for research and applications (MERRA), *US CLIVAR Variations*, *4*(2), 5–8.

Bouchard, A., F. Rabier, V. Guidard, and F. Karbou (2010), Enhancements of satellite data assimilation over Antarctica, *Monthly Weather Review*, *138*(6), 2149–2173.

Bromwich, D., R. Cullather, and M. Serreze (2000), Reanalyses depictions of the Arctic atmospheric moisture budget, in *The Freshwater Budget of the Arctic Ocean*, pp. 163–196, Springer.

Bromwich, D. H., J. P. Nicolas, and A. J. Monaghan (2011), An Assessment of Precipitation Changes over Antarctica and the Southern Ocean since 1989 in Contemporary Global Reanalyses*, *Journal of Climate*, *24*(16), 4189–4209.

Bromwich, D. H., J. P. Nicolas, A. J. Monaghan, M. A. Lazzara, L. M. Keller, G. A. Weidner, and A. B. Wilson (2013), Central West Antarctica among the most rapidly warming regions on Earth, *Nature Geoscience*, *6*(2), 139–145.

Bromwich, D. H., A. B. Wilson, L.-S. Bai, G. W. K. Moore, and P. Bauer (2015), A comparison of the regional Arctic System Reanalysis and the global ERA-Interim Reanalysis for the Arctic, *Quarterly Journal of the Royal Meteorological Society*.

Brönnimann, S. (2009), Early twentieth-century warming, *Nature Geoscience*, *2*(11), 735–736.

Burgess, E. W., R. R. Forster, J. E. Box, E. Mosley-Thompson, D. H. Bromwich, R. C. Bales, and L. C. Smith (2010), A spatially calibrated model of annual accumulation rate on the Greenland Ice Sheet (1958–2007), *Journal of Geophysical Research: Earth Surface (2003–2012)*, *115*(F2).

Cavalieri, D., and C. Parkinson (2008), Antarctic sea ice variability and trends, 1979–2006, *Journal of Geophysical Research: Oceans*, *113*(C7).

Collins, M., et al. (2013), *Long-term Climate Change: Projections, Commitments and Irreversibility*, book section 12, p. 1029–1136, Cambridge University Press, Cambridge, United Kingdom and New York, NY, USA.

Compo, G. P., et al. (2011), The twentieth century reanalysis project, *Quarterly Journal of the Royal Meteorological Society*, *137*(654), 1–28.

Connolley, W., and J. King (1993), Atmospheric water-vapour transport to Antarctica inferred from radiosonde data, *Quarterly Journal of the Royal Meteorological Society*, *119*(510), 325–342.

Cullather, R. I., and M. G. Bosilovich (2011), The moisture budget of the polar atmosphere in MERRA, *Journal of Climate*, *24*(11), 2861–2879.

Cullather, R. I., D. H. Bromwich, and M. L. Van Woert (1998), Spatial and Temporal Variability of Antarctic Precipitation from Atmospheric Methods*, *Journal of Climate*, *11*(3), 334–367.

Cullather, R. I., D. H. Bromwich, and M. C. Serreze (2000), The Atmospheric Hydrologic Cycle over the Arctic Basin from Reanalyses. Part I: Comparison with Observations and Previous Studies, *Journal of Climate*, *13*(5), 923–937.

Curry, J., J. Schramm, M. Serreze, and E. Ebert (1995), Water vapor feedback over the Arctic Ocean, *Journal of Geophysical Research: Atmospheres*, *100*(D7), 14,223–14,229.

Curry, J. A., J. L. Schramm, W. B. Rossow, and D. Randall (1996), Overview of Arctic cloud and radiation characteristics, *Journal of Climate*, *9*(8), 1731–1764.

Dee, D., et al. (2011), The ERA-Interim reanalysis: Configuration and performance of the data assimilation system, *Quarterly Journal of the Royal Meteorological Society*, *137*(656), 553–597.

Durre, I., R. S. Vose, and D. B. Wuertz (2006), Overview of the integrated global radiosonde archive, *Journal of Climate*, *19*(1), 53–68.

Ebita, A., et al. (2011), The Japanese 55-year Reanalysis "JRA-55": an interim report, *Sola*, *7*, 149–152.

Ettema, J., M. R. van den Broeke, E. van Meijgaard, W. J. van de Berg, J. L. Bamber, J. E. Box, and R. C. Bales (2009), Higher surface mass balance of the Greenland ice sheet revealed by high-resolution climate modeling, *Geophysical Research Letters*, *36*(12).

Favier, V., C. Agosta, S. Parouty, G. Durand, G. Delaygue, H. Gallée, A.-S. Drouet, A. Trouvilliez, and G. Krinner (2013), An updated and quality controlled surface mass balance dataset for Antarctica, *Cryosphere*, *7*(2), p–583.

Francis, J. A. (2002), Validation of reanalysis upper-level winds in the Arctic with independent rawinsonde data, *Geophysical research letters*, *29*(9), 29–1.

Genthon, C., and G. Krinner (1998), Convergence and disposal of energy and moisture on the Antarctic polar cap from ECMWF reanalyses and forecasts, *Journal of climate*, *11*(7), 1703–1716.

Gorodetskaya, I. V., M. Tsukernik, K. Claes, M. F. Ralph, W. D. Neff, and N. P. Van Lipzig (2014), The role of atmospheric rivers in anomalous snow accumulation in East Antarctica, *Geophysical Research Letters*, *41*(17), 6199–6206.

Grant, A., S. Brönnimann, and L. Haimberger (2008), Recent Arctic warming vertical structure contested, *Nature*, *455*(7210), E2–E3.

Gregory, J., and P. Huybrechts (2006), Ice-sheet contributions to future sea-level change, *Philosophical Transactions of the Royal Society of London A: Mathematical, Physical and Engineering Sciences*, *364*(1844), 1709–1732.

Groves, D. G., and J. A. Francis (2002), Moisture budget of the Arctic atmosphere from TOVS satellite data, *Journal of Geophysical Research: Atmospheres (1984–2012)*, *107*(D19), ACL–11.

Gulev, S., O. Zolina, and S. Grigoriev (2001), Extratropical cyclone variability in the Northern Hemisphere winter from the NCEP/NCAR reanalysis data, *Climate Dynamics*, *17*(10), 795–809.

Hartmann, D., et al. (2013), *Observations: Atmosphere and Surface*, book section 2, p. 159–254, Cambridge University Press, Cambridge, United Kingdom and New York, NY, USA.

Held, I. M., and B. J. Soden (2006), Robust responses of the hydrological cycle to global warming, *Journal of Climate*, *19*(21), 5686–5699.

Hersbach, H., C. Peubey, A. Simmons, P. Berrisford, P. Poli, and D. Dee (2015a), ERA-20CM: a twentieth-century atmospheric model ensemble, *Quarterly Journal of the Royal Meteorological Society.*

Hersbach, H., C. Peubey, A. Simmons, P. Berrisford, P. Poli, and D. Dee (2015b), ERA-20CM: a twentieth-century atmospheric model ensemble, *Quarterly Journal of the Royal Meteorological Society.*

Hines, K. M., R. W. Grumbine, D. H. Bromwich, and R. I. Cullather (1999), Surface Energy Balance of the NCEP MRF and NCEP-NCAR Reanalysis in Antarctic Latitudes during FROST*, *Weather and forecasting*, *14*(6), 851–866.

Hodges, K. (1994), A general-method for tracking analysis and its application to meteorological data, *Monthly Weather Review*, *122*(11), 2573–2586.

Hwang, Y.-T., D. M. Frierson, and J. E. Kay (2011), Coupling between Arctic feedbacks and changes in poleward energy transport, *Geophysical Research Letters*, *38*(17).

Jakobson, E., and T. Vihma (2010), Atmospheric moisture budget in the Arctic based on the ERA-40 reanalysis, *International Journal of Climatology*, *30*(14), 2175–2194.

Jones, P. D. (1994), Hemispheric surface air temperature variations: a reanalysis and an update to 1993, *Journal of Climate*, *7*(11), 1794–1802.

Kållberg, P. (2011), *Forecast drift in ERA-Interim*, European Centre for Medium Range Weather Forecasts.

Kalnay, E., et al. (1996), The NCEP/NCAR 40-year reanalysis project, *Bulletin of the American Meteorological Society*, *77*(3), 437–471.

Kanamitsu, M., W. Ebisuzaki, J. Woollen, S.-K. Yang, J. Hnilo, M. Fiorino, and G. Potter (2002), Ncep-doe amip-ii reanalysis (r-2), *Bulletin of the American Meteorological Society*, *83*(11), 1631–1643.

Karoly, D. (2015), *Meteorology of the southern hemisphere*, Springer.

Kattsov, V. M., and J. E. Walsh (2000), Twentieth-century trends of Arctic precipitation from observational data and a climate model simulation, *Journal of Climate*, *13*(8), 1362–1370.

Kattsov, V. M., J. E. Walsh, W. L. Chapman, V. A. Govorkova, T. V. Pavlova, and X. Zhang (2007), Simulation and projection of Arctic freshwater budget components by the IPCC AR4 global climate models, *Journal of Hydrometeorology*, *8*(3), 571–589.

King, J. C., and J. Turner (2007), *Antarctic meteorology and climatology*, Cambridge University Press.

Kobayashi, S., et al. (2015), The JRA-55 reanalysis: General specifications and basic characteristics, *Journal of the Meteorological Society of Japan. Ser. II.*, *93*(1), 5–48.

Kopec, B. G., X. Feng, F. A. Michel, and E. S. Posmentier (2016), Influence of sea ice on Arctic precipitation, *Proceedings of the National Academy of Sciences*, *113*(1), 46–51.

Krinner, G., O. Magand, I. Simmonds, C. Genthon, and J.-L. Dufresne (2007), Simulated Antarctic precipitation and surface mass balance at the end of the twentieth and twenty-first centuries, *Climate Dynamics*, *28*(2-3), 215–230.

Liu, C., and E. A. Barnes (2015a), Extreme moisture transport into the Arctic linked to Rossby wave breaking, *Journal of Geophysical Research: Atmospheres*, *120*(9), 3774–3788.

Liu, C., and E. A. Barnes (2015b), Extreme moisture transport into the Arctic linked to Rossby wave breaking, *Journal of Geophysical Research: Atmospheres*, *120*(9), 3774–3788.

Messori, G., and A. Czaja (2013), On the sporadic nature of meridional heat transport by transient eddies, *Quarterly Journal of the Royal Meteorological Society*, *139*(673), 999–1008.

Miloshevich, L. M., H. Vömel, D. N. Whiteman, B. M. Lesht, F. J. Schmidlin, and F. Russo (2006), Absolute accuracy of water vapor measurements from six operational radiosonde types launched during awex-g and implications for airs validation, *Journal of Geophysical Research: Atmospheres*, *111*(D9), n/a–n/a, doi:10.1029/2005JD006083, d09S10.

Monaghan, A. J., et al. (2006), Insignificant change in Antarctic snowfall since the International Geophysical Year, *Science*, *313*(5788), 827–831.

Newman, M., G. N. Kiladis, K. M. Weickmann, F. M. Ralph, and P. D. Sardeshmukh (2012), Relative contributions of synoptic and low-frequency eddies to time-mean atmospheric moisture transport, including the role of atmospheric rivers, *Journal of Climate*, *25*(21), 7341–7361.

Nicolas, J. P., and D. H. Bromwich (2011), Precipitation changes in high southern latitudes from global reanalyses: A cautionary tale, *Surveys in geophysics*, *32*(4-5), 475–494.

Onogi, K., et al. (2007), The JRA-25 reanalysis, *J. Meteorol. Soc. Jpn.*, *85*(3), 369–432.

Oshima, K., and K. Yamazaki (2006), Difference in seasonal variation of net precipitation between the Arctic and Antarctic regions, *Geophysical research letters*, *33*(18).

Palerme, C., J. Kay, C. Genthon, T. L'Ecuyer, N. Wood, and C. Claud (2014), How much snow falls on the Antarctic ice sheet?, *The Cryosphere*, *8*(4), 1577–1587.

Peixóto, J., and A. H. Oort (1992), Physics of climate, *American institute of physics, New York.*

Polyakov, I. V., et al. (2002), Observationally based assessment of polar amplification of global warming, *Geophysical research letters*, *29*(18), 25–1.

Rancic, M., J. Derber, D. Parrish, R. Treadon, and D. Kleist (2008), The development of the first-order time extrapolation to the observation (FOTO) method and its application in the NCEP global data assimilation system, in *12th Conference on IOAS-AOLS*.

Rawlins, M. A., et al. (2010), Analysis of the Arctic system for freshwater cycle intensification: Observations and expectations, *Journal of Climate*, *23*(21), 5715–5737.

Renan, E. (1881), *L'Ecclésiaste : un temps pour tout*, 11-62 pp., Arlea.

Rienecker, M. M., et al. (2011), MERRA: NASA's modern-era retrospective analysis for research and applications, *Journal of Climate*, *24*(14), 3624–3648.

Rogers, J. C. (1997), North Atlantic storm track variability and its association to the North Atlantic Oscillation and climate variability of northern Europe, *Journal of Climate*, *10*(7), 1635–1647.

Rudeva, I., and S. K. Gulev (2007), Climatology of cyclone size characteristics and their changes during the cyclone life cycle, *Monthly Weather Review*, *135*(7), 2568–2587.

Saha, S., et al. (2010), The NCEP climate forecast system reanalysis, *Bulletin of the American Meteorological Society*, *91*(8), 1015–1057.

Screen, J. A., and I. Simmonds (2010), The central role of diminishing sea ice in recent Arctic temperature amplification, *Nature*, *464*(7293), 1334–1337.

Seager, R., and N. Henderson (2013), Diagnostic Computation of Moisture Budgets in the ERA-Interim Reanalysis with Reference to Analysis of CMIP-Archived Atmospheric Model Data, *Journal of Climate*, *26*(20), 7876–7901.

Serreze, M., A. Barrett, J. Stroeve, D. Kindig, and M. Holland (2009), The emergence of surface-based Arctic amplification, *The Cryosphere*, *3*(1), 11–19.

Serreze, M. C., R. G. Barry, and J. E. Walsh (1995), Atmospheric water vapor characteristics at 70°N, *Journal of Climate*, *8*(4), 719–731.

Serreze, M. C., et al. (2006), The large-scale freshwater cycle of the Arctic, *Journal of Geophysical Research: Oceans (1978–2012)*, *111*(C11).

Solomon, A. (2006), Impact of latent heat release on polar climate, *Geophysical research letters*, *33*(7).

Sorteberg, A., and J. E. Walsh (2008), Seasonal cyclone variability at 70°N and its impact on moisture transport into the Arctic, *Tellus A*, *60*(3), 570–586.

Steig, E. J., D. P. Schneider, S. D. Rutherford, M. E. Mann, J. C. Comiso, and D. T. Shindell (2009), Warming of the Antarctic ice-sheet surface since the 1957 International Geophysical Year, *Nature*, *457*(7228), 459–462.

Stepaniak, D. (2008), ERA-Interim Vertical Coordinate Conventions and Numerical Attributes, `http://rda.ucar.edu/datasets/ds627.0/docs/Eta_coordinate/index.html`, accessed: 2016-02-04.

Stramler, K., A. D. Del Genio, and W. B. Rossow (2011), Synoptically driven Arctic winter states, *Journal of Climate*, *24*(6), 1747–1762.

Stroeve, J. C., M. C. Serreze, M. M. Holland, J. E. Kay, J. Malanik, and A. P. Barrett (2012), The Arctic's rapidly shrinking sea ice cover: a research synthesis, *Climatic Change*, *110*(3-4), 1005–1027.

Tilinina, N., S. K. Gulev, I. Rudeva, and P. Koltermann (2013), Comparing cyclone life cycle characteristics and their interannual variability in different reanalyses, *Journal of Climate*, *26*(17), 6419–6438.

Tilinina, N., S. K. Gulev, and D. H. Bromwich (2014), New view of Arctic cyclone activity from the Arctic system reanalysis, *Geophysical Research Letters*, *41*(5), 1766–1772.

Trenberth, K. E., J. T. Fasullo, and J. Mackaro (2011), Atmospheric moisture transports from ocean to land and global energy flows in reanalyses, *Journal of Climate*, *24*(18), 4907–4924.

Tsukernik, M., and A. H. Lynch (2013), Atmospheric meridional moisture flux over the Southern Ocean: A story of the Amundsen Sea, *Journal of Climate*, *26*(20), 8055–8064.

Tsukernik, M., D. N. Kindig, and M. C. Serreze (2007), Characteristics of winter cyclone activity in the northern North Atlantic: Insights from observations and regional modeling, *Journal of Geophysical Research: Atmospheres (1984–2012)*, *112*(D3).

Van de Berg, W., M. Van den Broeke, C. Reijmer, and E. Van Meijgaard (2006), Reassessment of the Antarctic surface mass balance using calibrated output of a regional atmospheric climate model, *Journal of Geophysical Research: Atmospheres*, *111*(D11).

Wallace, J. M., and P. V. Hobbs (2006), *Atmospheric science: an introductory survey*, vol. 92, Academic press.

Woods, C., R. Caballero, and G. Svensson (2013), Large-scale circulation associated with moisture intrusions into the Arctic during winter, *Geophysical Research Letters*, *40*(17), 4717–4721.

Yamanouchi, T. (2011), Early 20th century warming in the Arctic: A review, *Polar science*, *5*(1), 53–71.

Zhang, J. (2007), Increasing Antarctic sea ice under warming atmospheric and oceanic conditions, *Journal of Climate*, *20*(11), 2515–2529.

List of Figures

Relating Reynolds and Fourier decompositions

We would like to relate the "mean flow" term of the Reynolds decompostion, $\langle\langle q\rangle_n\langle v\rangle_n\rangle$, to the $\sum_{|j|\leq N} q_j v_{-j}$ term of the Fourier series. N is the ratio between the length of the time series, A, and the shorter time scale, a.

First we split the variables in long term mean and fluctuation e.g. $q = \bar{q} + (q - \bar{q})$.

For a given month, the product of the means can be written as :

$$\langle q\rangle_n\langle v\rangle_n = \bar{q}\bar{v} + \bar{q}\langle v - \bar{v}\rangle_n + \langle q - \bar{q}\rangle_n \bar{v} + \langle q - \bar{q}\rangle_n\langle v - \bar{v}\rangle_n$$

When we average the monthly means of a variable X over all months, Chasles' relation ensures that : $\langle\langle X\rangle_n\rangle = \overline{X}$. Accordingly :

$$\langle\langle q\rangle_n\langle v\rangle_n\rangle = \bar{q}\bar{v} + \bar{q}\ \overline{v - \bar{v}} + \overline{q - \bar{q}}\ \bar{v} + \langle\langle q - \bar{q}\rangle_n\langle v - \bar{v}\rangle_n\rangle$$

$\overline{q - \bar{q}}$ and $\overline{v - \bar{v}}$ go to zero so the second and third right hand side terms vanish.

We will now tackle the last term bit by bit, using the Fourier decomposition

$$q = \sum_{j\in\mathbb{Z}} q_j e_j \text{ with } e_j = e^{2\pi i j t/A}$$

to take advantage of the nice properties of the exponential function :

$$\begin{aligned}
\langle q - \bar{q}\rangle_n &= \frac{1}{a}\int_{na}^{(n+1)a} \sum_{j\in\mathbb{Z}^*} q_j e_j \ \mathrm{d}t \\
&= \frac{1}{a}\sum_{j\in\mathbb{Z}^*} q_j \left[\frac{A}{2\pi i j} e_j\right]_{na}^{(n+1)a} \\
&= \sum_{j\in\mathbb{Z}^*} \frac{N q_j}{2\pi i j}\left(e_j(a) - 1\right)\left(e_j(a)\right)^n
\end{aligned}$$

Combining both factors, we obtain :

$$\langle q - \bar{q}\rangle_n\langle v - \bar{v}\rangle_n = \sum_{j,k\in\mathbb{Z}^*} \frac{N q_j}{2\pi i j}\frac{N v_k}{2\pi i k}\left(e_j(a) - 1\right)\left(e_k(a) - 1\right)\left(e_{j+k}(a)\right)^n$$

Finally we average over all months in $[0, A]$. We change the order of summation :

$$\langle\langle q - \bar{q}\rangle_n\langle v - \bar{v}\rangle_n\rangle = \frac{1}{N}\sum_{j,k\in\mathbb{Z}^*} \frac{N q_j}{2\pi i j}\frac{N v_k}{2\pi i k}\left(e_j(a) - 1\right)\left(e_k(a) - 1\right)\sum_{n=0}^{N-1}\left(e_{j+k}(a)\right)^n$$

- If $(j+k)/N \notin \mathbb{Z}$, the $e_{j+k}(a)^n$ or $(e^{2\pi i(j+k)/N})^n$ for $n \in [\![1, N]\!]$ constitute a geometric series whose sum is :
$$\sum_{n=0}^{N-1} (e_{j+k}(a))^n = \frac{e_{j+k}(a)^N - 1}{e_{j+k}(a) - 1}$$
As it happens, $e_{j+k}(a)^N = e^{2\pi i(j+k)}$ which is one, $j+k$ being an integer, therefore the sum is zero.

- If there exists an integer p such that $j+k = Np$, then $e_{j+k}(a) = e^{2\pi i p}$, which is one. Therefore :
$$\sum_{n=0}^{N-1} (e_{j+k}(a))^n = N$$

It follows that :

$$\langle\langle q - \bar{q}\rangle_n \langle v - \bar{v}\rangle_n\rangle = \sum_{j\in\mathbb{Z}^*}\sum_{p\in\mathbb{Z}} \frac{Nq_j}{2\pi i j}\frac{Nv_{Np-j}}{2\pi i(Np-j)}\left(e_j(a) - 1\right)\left(e_{-j}(a) - 1\right)$$

We now reorganise the exponentials and the denominators into sinc functions and include the product of the means, $\bar{q}\bar{v} = q_0 v_0$:

$$\langle\langle q\rangle_n \langle v\rangle_n\rangle = \sum_{j\in\mathbb{Z}}\sum_{p\in\mathbb{Z}} (-1)\, q_j\, v_{-j}\ \mathrm{sinc}\!\left(\pi\frac{j}{N}\right)\ \mathrm{sinc}\left(\pi\frac{Np-j}{N}\right)$$

For well-behaved functions, the Fourier coefficents q_j and v_j tends towards 0 with increasing indices. Unless $p = 0$, either q_j or v_{Np-j} will likely be negligible.
Consequently, we propose the following approximation for the mean flow term :

$$\langle\langle q\rangle_n \langle v\rangle_n\rangle \approx \sum_{j\in\mathbb{Z}} q_j\, v_{-j}\ \mathrm{sinc}^2(\pi j/N)$$